ISBN 978-82-326-2070-8 (printed version)
ISBN 978-82-326-2071-5 (electronic version)
ISSN 1503-8181

Mahmoud Moqadam

Doctoral Thesis

Doctoral theses at NTNU, 2016:363

**NTNU**
Norwegian University of
Science and Technology
Faculty of Natural
Sciences and Technology
Department of Chemistry

NTNU
Norwegian University of
Science and Technology

NTNU

Doctoral theses at NTNU, 2016:363

Mahmoud Moqadam

# Mechanistic Study of Chemical Reactions Using Path Sampling

NTNU
Norwegian University of
Science and Technology

Mahmoud Moqadam

# Mechanistic Study of Chemical Reactions Using Path Sampling

Thesis for the degree of Philosophiae Doctor

Trondheim, December 2016

Norwegian University of Science and Technology
Faculty of Natural
Sciences and Technology
Department of Chemistry

NTNU
Norwegian University of
Science and Technology

**NTNU**
Norwegian University of Science and Technology

Thesis for the degree of Philosophiae Doctor

Faculty of Natural
Sciences and Technology
Department of Chemistry

ISBN 978-82-326-2070-8 (printed version)
ISBN 978-82-326-2071-5 (electronic version)
ISSN 1503-8181

Doctoral theses at NTNU, 2016:363

Printed by Skipnes Kommunikasjon as

# Preface

This thesis is submitted in partial fulfilment of the requirements for the degree of Philosophiae Doctor (Ph.D.) at the Norwegian University of Science and Technology (NTNU) and consists of four papers. The work was carried out in the chemistry department of NTNU, supervised by associate professor Titus S. van Erp and co-supervised by professor Per-Olof Åstrand. The project has been funded by the research Council of Norway and the Faculty of Natural Science and Technology of NTNU as part of the project *From Molecules to Process Applications*.

I have completed my Bachelor and Master of Science in petrochemical and chemical engineering with specialization in Reaction Engineering at Amirkabir University of Technology (Tehran Polytechnic) in October 2012. I have been accepted as a Ph.D. candidate in the chemistry department in March 2013.

## Acknowledgement

I am deeply indebted to my adviser Titus S. van Erp for his fundamental role in my doctoral work. Titus provided me with every bit of guidance, assistance, and expertise that I needed during my research. Titus gave me the freedom to follow and develop my intuition and plans while at the same time providing me with valuable feedback, advice, and encouragement. In addition to our academic collaboration, I greatly value the close personal rapport that Titus and I have forged over the years. I quite simply cannot imagine a better adviser.

I would like to thank my co-supervisor professor Per-Olof Åstrand for helping me understand concepts in theoretical chemistry and molecular modelling. I am very thankful to the post-doctoral researchers in the group, Dr. Enrico Riccardi and Dr. Anders Lervik, for having an active role in my project and also giving me very helpful tips about programming and problem-solving ideas. Their guidance and ideas helped me a great deal to achieve my goals in this work. I would like to thank Dr. Thuat T. Trinh and Mehdi Mahmoodinia for introducing me to concepts in molecular simulations and various software programs used in the computational chemistry. I also thanks Dr. Raffaela Cabriolu for proofreading and editing this thesis.

I also am very grateful to all the great people here in IKJ for the nice working atmosphere and specially our QuantiTIS group members for very interesting scientific and fun discussions during our weekly meeting.

Finally, I am deeply thankful to my loving family and my amazing friends for their love, support, and sacrifices. Without them, this thesis would never have been written. You are the best!

# Summary

Molecular simulations are the ideal tool to obtain detailed information at the molecular scale which is often invisible to experiments. However, we are still far from a situation in which industries and pharmaceutical laboratories effectively design new materials and medicines based on molecular modeling. Present simulation techniques such as standard molecular dynamics can not reach time- and length-scales required to study complex chemical and biological processes, or they are based on inaccurate and oversimplified models which make them unreliable. Several methods have been proposed over the last decades in order to overcome these problems. Many of those methods are able to provide thermodynamic properties much faster than plain molecular dynamics does, but they force the system in an unnatural way and, therefore, information about the unbiased dynamics is lost. The Transition Path Sampling (TPS) pioneered another approach showing how one can harvest paths (short molecular trajectories) via a statistically sound Monte Carlo approach. Based on this principle TPS also provided an algorithm for the determination of rate constants. Several aspects of this original algorithm were improved by the Transition Interface Sampling (TIS) method. Another variation of TIS, Replica Exchange TIS (RETIS), improved the algorithmic efficiency even further. TIS and RETIS divide the phase space in subregions using interfaces and gather a collection of true dynamical unbiased trajectories connecting the reactant and product states without a priori assumption of the reaction coordinate. From these ensembles of pathways, reaction mechanisms can be extracted and rate constants can be computed.

In this work, for the first time, we use a combination of the RETIS simulations with Ab initio molecular dynamics to study two realistic and challenging reactions. These reactions are autoionization of water and silicate oligomerization reactions. Although these reactions have previously been studied experimentally and/or theoretically, the exact mechanisms of reactions and rate constants are still under discussion. The autodissociation of a water molecule in pure water or an aqueous solution is a fundamental event in acid-base chemistry and is an extremely rare event on the femtosecond time scale of molecular motions. Silicate oligomerization is also a fundamental reaction that is at the basis of sol-gel chemistry and the formation of nanoporous silicate materials. RETIS provides a quantitative and deep qualitative analysis of these fundamental processes. In addition to the RETIS simulations, we have tested a ReaxFF forcefield for the silicate dimerization reactions and have examined this process with Ab initio molecular dynamics simulations using the more conventional thermodynamic integration methods. With these molecular dynamics simulations, we can study both dynamics properties and time dependent kinetic phenomena. Finally, we introduce an approach to analyze collective variables regarding their predictive power for a reaction. The method is based on already available path sampling data produced by, for instance, transition interface sampling or forward flux sampling.

## List of Publications

The publication made during the PhD is listed below:

1. M. Moqadam, E. Riccardi, T. T. Trinh, P. -O. Åstrand and T. S. van Erp, "A Test on Reactive Force Fields for the Study of Silica Dimerization Reactions", J. Chem. Phys. 143, 184113 (2015).

2. M. Moqadam, E. Riccardi, T. T. Trinh, A. Lervik, T. S. van Erp, "Rare Event Ab Initio Simulations Reveal Subtle Key Steps in Aqueous Silicate Dimerization", Manuscript.

3. T. S. van Erp, M. Moqadam, E. Riccardi, A. Lervik, "Analyzing Complex Reaction Mechanisms Using Path Sampling", J. Chem. Theory Comput. 12, 5398, (2016).

4. M. Moqadam, A. Lervik, E. Riccardi, T. S. van Erp, "Concerted and Stepwise Autoionization of Water", Manuscript.

### Not included in the thesis

5. R. Jalilzadeh, M. Moqadam, "A Comprehensive Kinetic Model of Fischer-Tropsch Synthesis Over Supported Cobalt Catalyst", submitted to Chemical and Process Engineering, September 2016.

### Contributions to the papers

Paper 1 / Chapter 3: M. Moqadam performed the simulations and wrote the initial draft. T. S. van Erp guided the overall supervision of the project. E. Riccardi, T. T. Trinh and P.-O Åstrand assisted with their specific expertise on the quantum mechanical calculations. All authors also contributed by participating in scientific discussions, reading, and writing of the manuscript.

Paper 2 / Chapter 4: M. Moqadam performed the simulations and wrote the initial draft. T. S. van Erp guided the overall supervision of the project and provided the first version of the RETIS computer program. E. Riccardi delivered the second version of the code which was used for the simulations. T. T. Trinh and A. Lervik assisted with their specific expertise on molecular modeling. All authors also contributed by participating in scientific discussions, reading, and writing of the manuscript.

Paper 3 / Chapter 5: T. S. van Erp developed the theoretical analysis method and wrote the initial draft. E. Riccardi, A. Lervik, M. Moqadam performed simulation on the one-dimensional model, the ion ionization model, and the Ab Initio gas-phase water dissociation respectively. All authors were involved in the programming of the analysis tools, participating in scientific discussions and the reading and writing of the manuscript.

Paper 4 / Chapter 6: M. Moqadam performed the simulations. A. Lervik and M. Moqadam analyzed the results and wrote the initial draft. T. S. van Erp guided the overall supervision of the project and provided the first version of the RETIS computer program. E. Riccardi delivered the second version of the code which was used for the simulations. All authors also contributed by participating in scientific discussions, reading, and writing of the manuscript.

# Contents

# Chapter 1

# Introduction

## 1.1 Background

Computational simulations can be used to find a reasonable starting point for a laboratory synthesis process and to provide a strong direction for the experimental investigations. Computational studies can also be carried out in order to achieve a better understanding of the reaction mechanism and to explore the possible reaction pathways that are not readily studied by the experimental means. In this work we use high-level computation methods to explore reaction mechanisms and rate constants of the silicate oligomerization reaction and the autoionization of water, which are two important reactions in many areas of chemical and biological processes.

### 1.1.1 Silicate Oligomerization

A main motivation to study silicate oligomerization is a wish to better understand how zeolites are formed. These materials have a tremendous importance for industrial applications. Hence, computational studies on the oligomerization process will shed light on the initial stages of zeolite synthesis and ultimately would allow a better control in designing novel and already known zeolitic materials in a more energy efficient or environmental-friendly way.

Zeolites are hydrated aluminosilicate minerals with a microporous structure commonly used as commercial adsorbents and catalysts in wide variety of the chemical and biochemical industries. The materials were discovered in the year 1756 by Swedish mineralogist Axel Fredrik Cronstedt and named based on the Greeks names, "zein and lithos", which simply mean "boiling water" [1]. These porous materials are formed in the nature as minerals or can also be made synthetically in the laboratories. Currently, from 229 different zeolite structures, about 83 percent of them are synthetically made. In 1950s, a new zeolite synthesis method led to the discovery of several different zeolites which were used for the purification process in the chemical industry, but nowadays they have several applications in the water purification, softening processes and petrochemical, agricultural and oil and gas industries [2].

The open 3D crystalline framework of zeolites are made from interlinked tetrahedral of alumina ($AlO_4$) and silica ($SiO_4$). The tetrahedral form, built by 4-coordinated atoms, is one of the most important properties of zeolites which traps water or other small-sized molecules inside the structure. The aluminosilicate framework structure usually contains the regular arrays of cages, cavities and channels and its negatively charged nature attracts the positive cations, such as metal ions, to drift into and out of the structure. This aspect makes zeolites useful for several industrial applications such as ion exchange, reversible dehydration and sorption.

All zeolites are aluminosilicate materials, however, the topology of the crystalline structure and the Si/Al ratio can differ tremendously among the different types of zeolites.

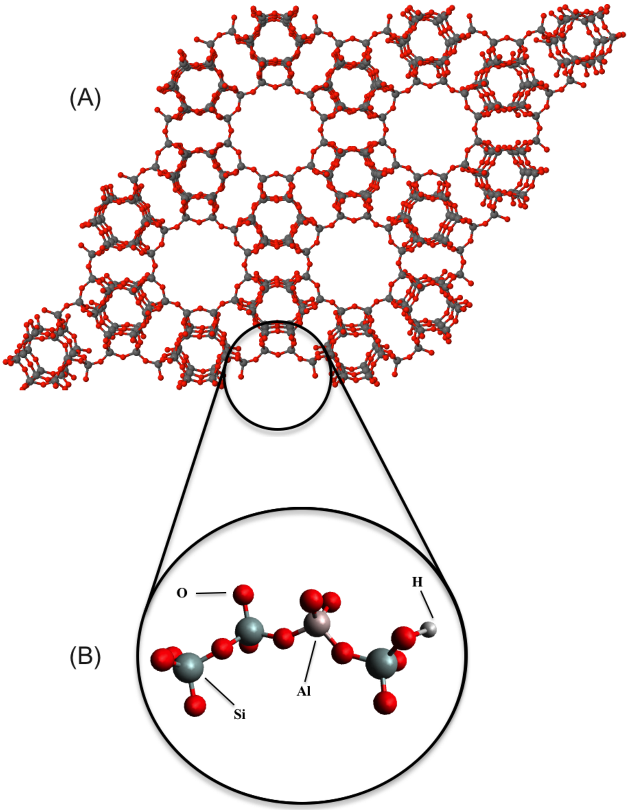

**Figure 1.1:** (A) Part of the crystal structure with 5- and 10-membered rings representing the vertical straight channels (B) Detail of the atomic structure, illustrating the interlinked tetrahedral form.

These parameters highly influence the possible application of the material. Low-silica or aluminium rich zeolites are highly selective for polar molecules such as water, while the high-silica zeolites preferably adsorb the less or non-polar molecules. Figure 1.1 represents the micropore system of a high-silica zeolite, pentasil-zeolite (ZSM-5), commonly used as a heterogeneous catalyst for the fluidized catalytic cracking (FCC) of petroleum.

Zeolites are resistant to high temperatures. They don't dissolve in water or other inorganic solvents. They also have a relatively high melting point that is above 1000 °C. These unique properties make zeolites ideal for industrial applications. Therefore, a continuous research effort aims to develop more of these types of porous material with highly specific chemical and physical aspects [3–5]. This development is, however, slow since a fundamental understanding how these structures form is lacking.

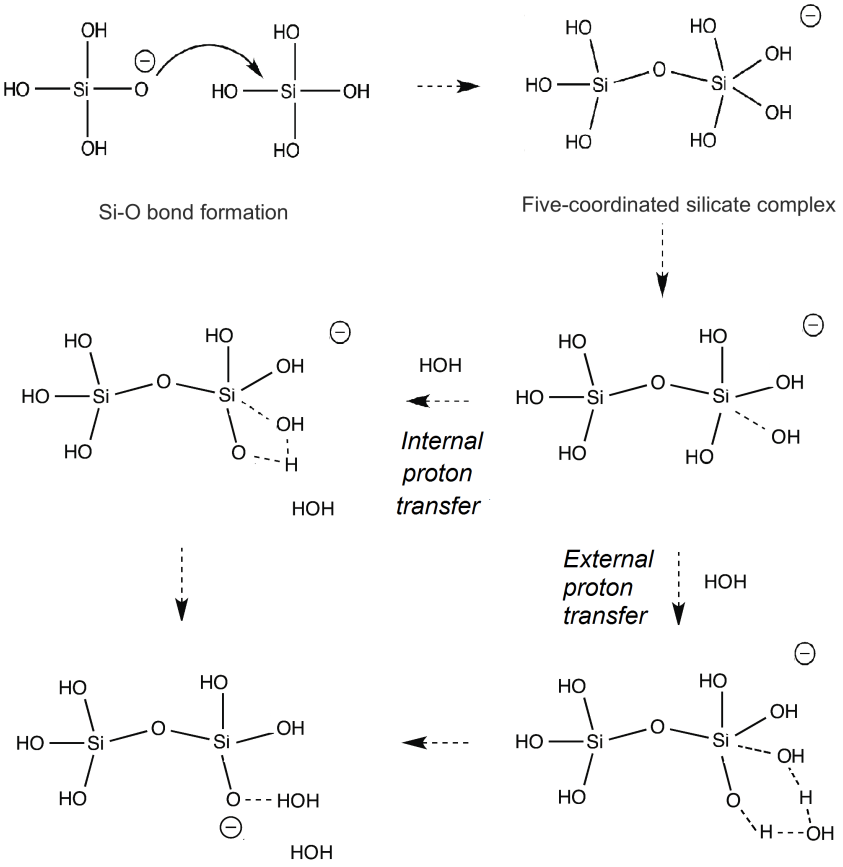

**Figure 1.2:** The silicate oligomerization reaction.

The process of hydrothermal zeolite synthesis has been broadly reviewed in several science and technology books [1–3, 6]. Aluminosilicate zeolites are typically synthesized under the hydrothermal conditions from an aluminate solution and a silicate solution mixture in an alkaline media and at temperatures between about 80 and 200 °C [7].

The oligomerization process is a key elementary reaction in zeolite synthesis. Therefore, understanding how the silicate and the aluminum oligomers grow is of the fundamental scientific and technological importance. In this thesis, we study the first step in the silicate oligomerization mechanism which is the formation of the SiO−Si linkage between the reactants to form a five-coordinated silicate complex which is an essential intermediate in the condensation reaction (figure 1.2). The intermediate can then either dissociate again or its formation is followed up by a water removal step which leads to a stable negatively charged product, the silicate dimer. In a consecutive step, the dimer can grow further by addition of other monomers to form trimers and larger oligomeric species including both linear polymers and ring-structures.

### 1.1.2 Autoionization of Water

Understanding the behavior of the aqueous solution is of fundamental importance in many areas of the chemistry and biology. Water plays a crucial role as an universal solvent for a wide range of the chemical processes. Water has the amphiprotic nature as its molecules can act as either an acid or a base depending on the nature of other reactant. Acids and bases can be defined in different ways. In 1884, the Swedish chemist Svante Arrhenius proposed a basic definition for the acid-base reaction. According to this definition, an acid is a chemical substance which dissociates in the aqueous solution to form hydrogen ions ($H^+$), and a base is a chemical substance which dissociates in the aqueous solution to form hydroxide ions ($OH^-$). Later, two more practical and general theories were proposed: Brønsted-Lowry theory and Lewis theory [8]. The Brønsted-Lowry theory defines the acids and bases as the proton donors and acceptors. The Lewis theory of acids and bases envisages acids as the acceptors and bases as the donors of the electron-pair [8, 9]. However, there is no strict rule for choosing any of these definitions because in a general perspective all three definitions are essentially equivalent.

**Table 1.1:** Definitions of Acids and Bases.

| | Acids | Bases |
|---|---|---|
| Arrhenius | $H^+$ donor | $OH^-$ donor |
| Brønsted-Lowery | $H^+$ donor | $H^+$ acceptor |
| Lewis | electron-pair acceptor | electron-pair donor |

One of the most important chemical properties of water is its ability to act as either a Brønsted acid or a Brønsted base. In pure water or aqueous solution, one water molecule can deprotonate to become a hydroxide ion ($OH^-$) and a hydrogen nucleus ($H^+$). The latter protonates another water molecule to create a hydronium ion ($H_3O^+$). This process is called the autoionization of water (see figure 1.3) and it determines the pH of water. Autoionization is greatly involved with the acid-base chemical equilibria. The process is

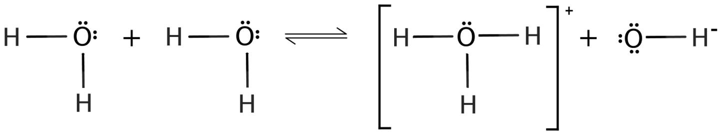

**Figure 1.3:** The autoionization of water.

extremely rare and about two out of every $10^9$ molecules is ionized at any given instant. Therefore, a extremely small number of hydroxide ions and hydronium ions are present at any particular time [10, 11].

The equilibrium constant $K_c$ for this reaction is given by,

$$K_c = \frac{\left[\mathrm{H_3O^+}\right]\left[\mathrm{OH^-}\right]}{[\mathrm{H_2O}]^2} \tag{1.1}$$

The concentrations [. . .] are given here in standard concentrations (mol/l). The concentration of water, $[H_2O]$, remains essentially constant in pure water and aqueous solutions. Thus, this expression can be simplified by excluding the concentration of water. The new equilibrium constant expression can be written as

$$K_w = K_c\,[\mathrm{H_2O}]^2 = \left[\mathrm{H_3O^+}\right]\left[\mathrm{OH^-}\right] \tag{1.2}$$

The concentration of hydroxide and hydronium ions presents in pure water at room temperature (25 °C) are equal: $[H_3O^+] = [OH^-] = 1.003 \times 10^{-7}$. Hence,

$$K_w = \left[\mathrm{H_3O^+}\right]\left[\mathrm{OH^-}\right] \approx 1.0 \times 10^{-14} \tag{1.3}$$

In the equation 1.3 the concentrations of hydronium and hydroxide ions are the acid and base constants, respectively [12]. Thus, pH and pOH, can easily obtained by

$$\begin{aligned} \mathrm{pH} &= -\log_{10}\left[\mathrm{H_3O^+}\right] = 7 \\ \mathrm{pOH} &= -\log_{10}\left[\mathrm{OH^-}\right] = 7 \end{aligned} \tag{1.4}$$

The sum of these two gives the equilibrium constant equation, $\mathrm{pK}_w$ at (25 °C),

$$\mathrm{pK_w} = \mathrm{pH} + \mathrm{pOH} = 14 \tag{1.5}$$

Although the amount of hydronium and hydroxide ions is extremely low in pure water, still it leads to a very weak electrical conductivity of water [11]. In this work we use the theory of quantum mechanics to investigate the mechanism and the rate of autoionization of water.

## 1.2 Aim and Objective

The aim of this thesis is to perform unbiased mechanistic investigations on reactive chemical reactions using a path sampling technique. The main objectives in this work are to use a unique path sampling technique to tackle the time scale problem and to describe true dynamical evolution of realistic and challenging processes. The processes are:

- Silicate dimerization reactions: Molecular thermodynamics, mechanisms and rate constants of the early stages of the silicate condensation process are investigated. This is done by first studying the dissociation and association reactions of silicate complex in the gas phase. The dissociation and water removal reactions of silicate complex are also studied in the aqueous solution in the presence of sodium ion.

- Autoionization of water: With a proper implementation of the path sampling technique in combination with ab initio molecular dynamics simulations, a fully detailed qualitative and quantitative study on the mechanism of autoionization process in liquid water is presented.

To accomplish these goals we have used density functional theory (DFT), reactive force field (ReaxFF), molecular dynamics (MD) and replica exchange transition interface sampling (RETIS) combined with Born-Oppenheimer molecular dynamics (BOMD). Our path sampling technique will improve the knowledge about the different aspect of the chemical reactions involved in these processes.

## 1.3 Outline of the Thesis

A short theoretical background is given in Chapter 2 for the methods being used in the thesis. Based on the results of this work, four manuscripts have been prepared, from which two have been already published (Chapters 3, 5) and two have been submitted (Chapter 4, 6).

In Chapter 3, DFT has been used to study the initial step of silicate dimerization reactions in the gas and aqueous phase. Then, a comparison between DFT and ReaxFF calculations have been presented. The reactive force field was based on two different ReaxFF parameter sets.

In Chapter 4, reaction mechanisms and rate constants of early stages in silicate condensation reaction have been studied. We have performed RETIS combined with CP2K to overcome the time scale challenges as well as to analyse the different possible reaction mechanisms involved in the gas and aqueous phases.

In Chapter 5, a quantitative analysis method for identifying mechanisms and initiation conditions for reactive chemical reactions is introduced. The analysis is performed on the path sampling data that are already produced by path sampling simulations for computing reaction rates.

In Chapter 6, dissociation of water molecules in pure water have been studied to reveal molecular mechanism of autoionization process. The combination of RETIS and CP2K have been used to describe the true dynamical pathways and to measure the rate constant of water dissociation in this process.

In Chapter 7, we have briefly discussed our ongoing projects on autodissociation of water molecules in presence of chloride and sodium ions. This study will complement and expand our work in Chapter 6 by addressing how the presence of ions can accelerate the ionization process of water.

The final Chapter presents a short conclusion for the thesis and topics for future research.

# Bibliography

[1] D. Breck. *Zeolite Molecular Sieves*. Wiley: New York, 1974.

[2] R. M. Barrer. *Hydrothermal Chemistry of Zeolites*. Academic Press: London, 1982.

[3] R. Szostak. *Molecular Sieves - Principles of Synthesis and Identification*. Springer: The Netherlands, 1998.

[4] E. M. Flanigen, R. L. Patton, and S. T. Wilson. Structural, synthetic and physicochemical concepts in aluminophosphate-based molecular sieves. *Stud. Surf. Sci. Catal*, 37:13–27, 1988.

[5] C. T. Kresge, M. E. Leonowicz, W. J. Roth, J. C. Vartuli, and J. S. Beck. Ordered mesoporous molecular sieves synthesized by a liquid-crystal template mechanism. *Nature*, 359:710–712, 1992.

[6] P. A. Jacobs and J. A. Martens. *Synthesis of High-Silica Aluminosilicate Zeolites*. Elsevier Science: New York, 1987.

[7] R. Xu, W. Pang, and Q. Huo. *Modern Inorganic Synthetic Chemistry*. Elsevier Science: Netherlands, 2011.

[8] D. W. Oxtoby, H. P. Gills, and A. Campion. *Principles of Modern Chemistry*. Cengage Learning: Boston, 2011.

[9] P. Atkins and L. Jones. *Chemical Principles: The Quest For Insight*. W. H. Freeman & Co Ltd: New York, 2012.

[10] F. H. Stillinger. *Theory and Molecular Models for Water*. John Wiley & Sons, Inc., 2007.

[11] J. C. Kotz, P. M. Treichel, and J. Townsend. *Chemistry and Chemical Reactivity*. Brooks Cole, 2011.

[12] I. Tinoco, K. Sauer, and J. C. Wang. *Physical Chemistry. Principles and Applications in Biological Sciences*. Prentice-Hall, 1995.

# Chapter 2

# Theoretical Concepts

## 2.1 Density Functional Theory - DFT

Quantum Mechanics is a fundamental theory developed to describe the physics of microscopic world and to provide information about the structure and the energy for a system of atoms and protons. Quantum concepts are not easy to grasp because they are very far from our classical intuition based on our experience of the macroscopic world. In principle, most quantum chemical methods attempt to solve the steady-state Schrödinger equation. The time-independent Schrödinger equation is given by

$$E\psi = \hat{H}\psi \tag{2.1}$$

where $\psi$ is the wave function which defines the state of the system, and the term $E$ denotes the energy of the electrons and nuclei system. The term $\hat{H}$ is defined as the Hamiltonian operator corresponding to the total energy of the system acting on the overall wave function. One dimensional Hamiltonian is given by,

$$\hat{H} = -\frac{\hbar^2}{2m}\frac{\partial^2}{\partial x^2} + V(x) \tag{2.2}$$

where the first term is the operator associated with the kinetic energy and second term is the potential energy of the system. The Hamiltonian operator $\hat{H}$ for a system of particles is generally very complex and computationally difficult to be solved [1, 2]. Therefore, some approximations have been included to solve the equation 2.2 by using the approximate methods like Hartree-Fock (HF) and Density functional theory (DFT) [3]. These theories are designed to lighten the computational complexity.

Hartree-Fock theory is based on a simplified expression in which the complicated many-electron wave function is written as a single Slater determinant [4]. Density functional theory is an alternative prescription of quantum mechanics, which allows one to replace these complicated many-electron wave functions $\psi$, by much simpler electron density $\rho(r)$. This is a remarkable theory that can characterize an atom, a molecule, a radical or several interactive molecules. The history of DFT begins with the works of Thomas and Fermi [5,6] in the 1920s but the modern DFT is based on two fundamental theorems introduced by Hohenberg and Kohn (HK) [7].

The first theorem states that for any many-electron system in an external potential, the external potential is uniquely determined by the ground state density. Based on this theorem, the total energy as a functional of the electron density can be written as:

$$E_0[\rho] = \int \rho(r)\nu_{\text{ext}}\text{dr} + F[\rho] \tag{2.3}$$

$$F[\rho] = T[\rho] + V_{ee}[\rho] \tag{2.4}$$

where $\nu_{\text{ext}}$ is the external potential in which the interacting electrons are moving, $F[\rho]$ is the HK functional. This is a universal functional of the density and is completely independent of the system and the external potential. $V_{ee}[\rho]$ is the electron-electron interaction energy and $T\,[\varphi]$ is the kinetic energy of electrons. The exact shape of the kinetic energy and the electron interaction energy functionals are not known. Therefore, the energy cannot be calculated.

The second theorem states that if $F[\rho]$ would be known, the density $\rho_0(r)$ which minimizes the functional $E_0[\rho]$ must correspond to the true density provided that the system is in the electronic ground state. Although Hohenberg-Kohn theorems are potentially powerful, in practice, they do not provide a way for computing the ground state density of a system. In 1965, Kohn and Sham devised a practical method for finding the electron density and the energy of ground state. They suggested the following form of the functional to approximate the unknown energy functional [8]:

$$E_0[\rho] = T_s\,[\rho] + \int \rho(r)\nu_{ext}dr + E_H[\rho] + E_{xc}[\rho] \tag{2.5}$$

where $T_s\,[\rho]$ is the kinetic energy of a reference system $s$ of $n$ non-interacting electrons given by

$$T_s[\rho] = -\frac{1}{2}\sum_{i}^{N}\langle\psi_i \mid \bigtriangledown^2 \mid \psi_i\rangle \tag{2.6}$$

and $E_H[\rho]$ is the Coulomb (or Hartree) energy,

$$E_H[\rho] = \frac{1}{2}\int\int \frac{\rho(r)\rho(r')}{r-r'}drdr' \tag{2.7}$$

and $E_{xc}[\rho]$ is the exchange-correlation energy which is the only unknown term. This is the fundamental key element of the Kohn-Sham approach to DFT. The exchange correlation functional corrects for the fact that an electron cannot repel itself, like the Hartree energy functional suggests, and that the motion of electrons is not independent. The exact value of the exchange-correlation energy is unknown, however it can be approximated. Therefore, the accuracy of DFT concretely depends on the accuracy of the exchange-correlation functionals. The simplest approximation is the local density approximation (LDA) which is based on the results of the homogeneous electron gas. The local density approximation assumes that the density can be treated locally as a homogeneous electron gas. It presumes that the exchange correlation energy per particle in a system is the same as that of an uniform electron gas of the same density which can be computed by quantum monte carlo [9].

$$E_{xc}^{LDA}\,[\rho] = \int \rho(r)\epsilon_{xc}(\rho(r))dr \tag{2.8}$$

where $\epsilon_{xc}(\rho)$ is the exchange-correlation energy per particle of an uniform electron gas of density $\rho$. The LDA works well in many different applications as in the solid state physics. However, LDA leads to an overestimation in the calculated energies, in particular, where the density experiences the rapid changes such as in molecules. Another class of approximations for the exchange correlation functionals is the Generalized Gradient Approximation (GGA). The GGA such as Becke Lee Yang Parr (BLYP) [10] is still local but also takes the gradient of the electron density into account. GGA functionals can be divided into the exchange and the correlation part and treated individually. For example the BLYP functional is obtained by adding the gradient corrections to the LDA method with the exchange correction of Becke and the correlation function of Lee, Yang and Parr [10]. The BLYP functional has been widely used in the theoretical chemistry and gives very good results for the molecular geometries and ground-state energies. Yet, a good description of the exchange part of the energy is very difficult. BLYP can be improved by the hybrid functionals proposed by Becke. The hybrid functionals (such as B3LYP) are usually constructed as a linear combination of the Hartree-Fock (HF) exchange (which provides more accurate exchange energy) and the correlation (and/or exchange) energy obtained from LDA theory [10, 11]. $E_{xc}^{hyb}[\rho]$ is given by:

$$E_{xc}^{hyb} = E_{xc}^{LDA} + a_0(E_x^{HF} - E_x^{LDA}) + a_x(E_x^{GGA} - E_x^{LDA}) + a_c(E_c^{GGA} - E_c^{LDA}) \quad (2.9)$$

where $a_0 = 0.20$, $a_x = 0.72$ and $a_c = 81$ are the empirically fitted parameters.

Another important factor in the accuracy of DFT is the choice of basis set which is used to approximate the actual wave function. A basis set in computational chemistry often refers to a set of functions (called basis functions) which are combined in linear combinations to build molecular orbitals. These functions are typically the atomic orbitals (but can theoretically be any one-particle functions). Early, Slater-type orbitals (STOs) were the most popular basis functions due to their similarity to atomic orbitals of the hydrogen atom. However, STOs are computationally difficult and are not suitable for fast calculations of necessary two-electron integrals. That is why the Gaussian type orbitals (GTOs) were introduced. One can approximate the shape of the Slater-type orbitals function by summing up a number of Gaussian type orbitals. This leads to a huge computational savings. GTOs allow a much faster calculation of the integrals than the calculations involving STOs. However, unlike Slater type orbitals, the Gaussians orbitals cannot capture the cusp of the wave function nor the exponential decay which implies that one needs more Gaussians for the given accuracy [12].

There are hundreds of different basis sets, and the choice of a basis set significantly impacts the accuracy and speed of computer programs. The smallest of these basis sets are called minimal basis sets, and they are usually formed of the minimum number of basis functions required to represent all electrons. In such a minimum basis set each atomic orbital is represented by a number of Gaussians that are chosen to mimic the behavior of the STO. Since the minimal basis sets typically give rough results, one may improve them using two functions for each of the minimal basis functions (i.e. a double zeta basis set) or three functions for each of the basis functions (i.e. a triple zeta basis set). Zeta symbol ($\zeta$) is often used to present the exponent of an STO basis function. Another factor to improve the minimal basis set is the addition of polarization and diffusion functions. The normal abbreviation for a double zeta basis set is DZ. The double-zeta basis set is very important because it treats each orbital separately and each atomic orbital is expressed as sum of two Slater type orbitals. The double zeta basis set for a 2s orbital is given by,

$$\Phi_{2s}^{STO}(r) = \Phi_{2s}^{STO}(r_1, \zeta_1) + d\Phi_{2s}^{STO}(r_2, \zeta_2) \tag{2.10}$$

where the constant $d$ determines how much each STO will count towards the final orbital. A more accurate one is QZ4P basis set developed by van Lenthe and Baerends [13]. It can be described as a core triple zeta, valence quadruple zeta basis set, with four sets of polarization functions which make it an accurate but expensive option for the calculations. In practice, you need to choose a basis set, among many different options, that gives the best possible tradeoff between accuracy and efficiency for the system [14]. For our research, we used the Amsterdam Density Functional (ADF) package to study our systems in the gas phase using QZ4P STO basis set [15]. We also studied our systems in the aqueous phase using Quickstep [16] which is a part of CP2K program package [17]. Quickstep is based on the Gaussian and plane waves method and its augmented extension. We used DZVP basis set, and plane waves as auxiliary basis to study the dynamics of the systems.

## 2.2 (Ab initio) Molecular Dynamics - MD/AIMD

Molecular dynamics (MD) method traces the physical movements and the dynamical evolution of the interacting particles by numerically solving the classical equations of motion for a many-body system. Newton's second law equations of motion are integrated for all particles simultaneously and the forces between the particles are calculated from the negative gradient of a particular potential function $V(r_1, ..., r_N)$.

$$m_i \frac{\partial^2 r_i}{\partial t^2} = F_i = -\bigtriangledown_i V(r_1, ..., r_N) \tag{2.11}$$

The potential function is given as the sum of individual energy terms:

$$V = V_{\text{covalent}} + V_{\text{noncovalent}} \tag{2.12}$$

Here, the covalent term is given by following summation:

$$V_{\text{covalent}} = V_{\text{bond}} + V_{\text{angle}} + V_{\text{torsion}} \tag{2.13}$$

where the first term on the right is the bond stretching energy, the second is the angle bending energy and the third is the torsional or the dihedral energy. Likewise, the noncovalent contribution is given as

$$V_{\text{noncovalent}} = V_{\text{vdWaals}} + V_{\text{electrostatic}} \tag{2.14}$$

where the first term on the right is the van der Waals interactions, typically modeled using the Lennard-Jones potential, and the second term is the electrostatic term and of which the basic functional form is the Coulomb potential.

All of these interaction energies combined together are known as a force field (FF) [18]. Many force fields have been developed and parameterized for different systems such as AMBER [19], CHARMM [20], OPLS-AA [21], ReaxFF [22], etc. These force field are parametrized by fitting experimental data and theoretical calculations results. Parameters in each force field are supposed to be internally consistent, but these parameters are generally not transferable between different force fields [23]. The transferability implies that the same force field parameters are used to describe a given functional group in different molecules, state points, thermodynamic and structural properties [24]. Differences in shape of force field functions, simplifying assumptions and combining rules are part of the rationale for the often-repeated statement that different force fields are commonly not transferable and compatible [23]. In this work, we have used the ReaxFF, a bond order based force field, which is commonly used to model the chemical reactions.

However, in chemically complex situations, the parameterization of decent empirical potentials is not always possible in practice. The limitations of classical MD are overcome by using ab initio molecular dynamics (AIMD), where the forces are calculated from a fully quantum mechanical description, usually using a plane-wave expansion of the DFT orbitals. Direct trajectory calculations can be grouped into three main categories: Ehrenfest MD [25], Car-Parrinello MD [26] and Born-Oppenheimer MD (BOMD) [27].

In this work, we have used the Born-Oppenheimer approach, which has been included in the CP2K simulation package [28]. In the Born-Oppenheimer approximation, it is assumed that the electronic and nuclear motions can be separated, and the wave function of a molecule is adiabatically divided into its nuclear and electric components.

$$\Psi_{\text{total}} = \Psi_{\text{electronic}} + \Psi_{\text{nuclear}} \tag{2.15}$$

In the Born-Oppenheimer molecular dynamics, the wave function $\Psi$ is restricted to be the ground state adiabatic wave function $\Psi_0$. The nuclei are propagating in time via the classical molecular dynamics while the electronic part is treated through the time-independent Schrödinger equation and is solved self-consistently at each BOMD step, assuming that the nuclei are fixed in a certain configuration at that instant of time. The equations of motion for the nuclei within the Born-Oppenheimer molecular dynamics method is defined by [29]

$$M_I \ddot{R}_I(t) = -\nabla_I \min\left\{\langle \Psi_0 \mid H_e \mid \Psi_0 \rangle\right\} \tag{2.16}$$

where for each BOMD step the minimum of electronic Hamiltonian $\langle\ H_e\rangle$ has to be reached.

The molecular dynamics can target a wide variety of molecules including the small molecules as well as large molecules containing thousands of atoms. In this work, we applied the classical molecular dynamics, ReaxFF MD, and ab initio molecular dynamics, BOMD, and evaluated the qualitative behavior of these methods for a system of silicate-water interactions.

## 2.3 Reactive Force Field - ReaxFF

The modern quantum chemistry methods are quite accurate and fast to predict the geometries, atomic and vibrational energies for small molecules. In general, the quantum chemical methods can be used for all chemical systems. However, these methods are very expensive and the computational cost makes them impractical for studying the systems including large or many molecules. Therefore, it is desirable to have the accurate force fields to evaluate the forces and other dynamical properties. As mentioned previously, a force field is a set of functionals and parameters used to compute the potential energy of a system of atoms. The parameters of these energy functions can be derived from the experimental work and the quantum mechanical calculations. Different force fields are designed for different purposes. ReaxFF is a force field for modeling chemical reactions with the atomistic potentials developed by van Duin and coworkers [22]. ReaxFF is a set of reactive potential functions to simulate the breaking and the formation of bonds in chemical reactions at molecular level. It is an empirical approach which can mimic the quantum mechanical variation of bond order. The parameters have been derived from small scale quantum mechanical calculations. In comparison with ab initio MD, ReaxFF can reach much larger time scales (nanosecond scale) for a much larger numbers of atoms($\gg$1000). Still, its accuracy is claimed to be very close to that of the quantum mechanics [30–32]. ReaxFF was developed to bridge the gap between the quantum chemical and the empirical force fields based computational chemical methods. Different ReaxFF parameter sets have been developed for a wide variety of chemical environments, including hydrocarbons, proteins and many inorganic systems. Figure 2.1 represents the position of ReaxFF in the hierarchy of various computational methods considering the length and time scales for the simulation of a system of particles. The quantum mechanical methods deal with the atomistic scale, continuum methods like finite element analysis (FEA) deal with materials at a macroscopic length and time scale [31]. ReaxFF deals with materials at the nanoscale.

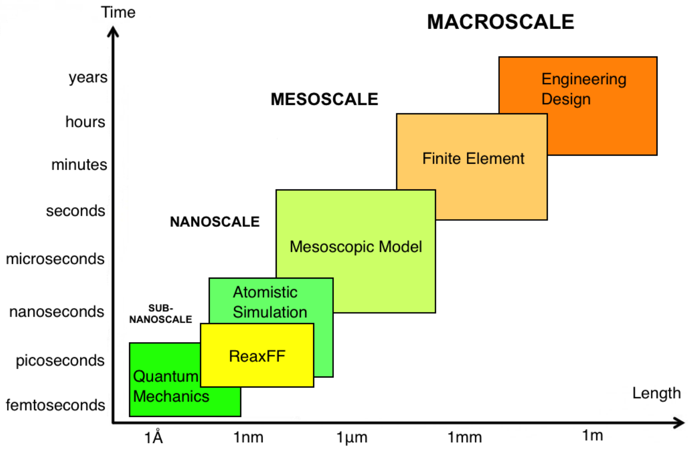

**Figure 2.1:** The hierarchy of various computational methods considering the length and time scales for simulation of a system of particles.

Similar to the empirical nonreactive force fields, the reactive force field partitioned the system energy into the several partial energy contributions, introduced in equation,

$$\begin{aligned} E_{\text{system}} = E_{\text{bond}} + E_{\text{over}} + E_{\text{under}} + E_{\text{lp}} + E_{\text{val}} + E_{\text{pen}} + E_{\text{coa}} + \\ E_{\text{C2}} + E_{\text{tors}} + E_{\text{conj}} + E_{\text{H-bond}} + E_{\text{vdWaals}} + E_{\text{Coulomb}} \end{aligned} \tag{2.17}$$

**Bond Order (BO) and Bond Energy.** ReaxFF uses a general relationship between bond distance and bond order. Bond orders between a pair of atoms can be derived directly from the interatomic distances. Bond orders are continuously updated in each iteration [22]. This fundamental assumption allows the formation and the dissociation of bonds during the simulation to have a smooth transition between nonbonded, single, double and triple bonded systems. The bond energy ($E_{\text{bond}}$) is determined from the bond orders $BO'_{ij}$:

$$\begin{aligned} BO'_{ij} = BO'^{\sigma}_{ij} + BO'^{\pi}_{ij} + BO'^{\pi\pi}_{ij} = \exp\left[P_{bo,1}\left(\frac{r_{ij}}{r_0^{\sigma}}\right)^{P_{bo,2}}\right] + \\ \exp\left[P_{bo,3}\left(\frac{r_{ij}}{r_0^{\pi}}\right)^{P_{bo,4}}\right] + \exp\left[P_{bo,5}\left(\frac{r_{ij}}{r_0^{\pi\pi}}\right)^{P_{bo,6}}\right] \end{aligned} \tag{2.18}$$

in which the three exponential terms describe the sigma-, the pi- and the double pi-bonds, each depending on three fitted parameters ($P_{\text{bo},1}$, $P_{\text{bo},2}$, $r_0^{\sigma}$), ($P_{\text{bo},3}$, $P_{\text{bo},4}$, $r_0^{\pi}$), and ($P_{\text{bo},5}$, $P_{\text{bo},6}$, $r_0^{\pi\pi}$), respectively.

However, the bond orders ($BO'_{ij}$) need to be corrected in order to avoid over coordinations. The bond orders are typically corrected by removing the unrealistic weak bonds and leaving the strong bonds intact.

ReaxFF energy function generally includes the bond energy, over and under coordination energy, lone pair energy, angle strain, penalty energy, angle conjugation, C2 correction, torsion energy, torsion conjugation, hydrogen bond terms. In addition to these terms, ReaxFF includes the van der Waals and coulomb interaction terms, the crucial terms often missing from other forcefields, to describe non-bonded interactions between all atoms, irrespective of connectivity [22].

**van der Waals Interactions.** Van der Waals forces include attractions at long distances due to dispersion and repulsions at short interatomic distances due to Pauli principle. ReaxFF takes the van der Waals interactions into account by using a distance-corrected Morse-potential (equation 2.19) including a shielded interaction (equation 2.20) to avoid the excessive close-range non-bonded interactions:

$$\begin{aligned} E_{vdWaals} = D_{ij} \Bigg\{ & \exp\left[\alpha_{ij}\left(1 - \frac{f(r_{ij})}{r_{vdw}}\right)\right] - \\ & 2\exp\left[\frac{1}{2}\alpha_{ij}\left(1 - \frac{f(r_{ij})}{r_{vdw}}\right)\right] \Bigg\} \end{aligned} \tag{2.19}$$

$$f(r_{ij}) = \left[ r_{ij}^{\lambda_{vdw}} + \left(\frac{1}{\lambda_w}\right)^{\lambda_{vdw}} \right]^{1/\lambda_{vdw}} \tag{2.20}$$

where $\alpha_{ij}$, $\lambda_w$ and $\lambda_{vdw}$ are van der Waals parameters [22, 33].

**Coulomb Interactions.** As with the van der Waals interactions, the Coulomb interactions are calculated between all atom pairs. ReaxFF applies geometry-dependent atomic charge calculations using the charge equilibration method (EEM) [34] that accounts for the polarization effects. A shielded potential is employed to adjust for the orbital overlap between atoms at close distances which is given by

$$E_{Coulomb} = C.\frac{q_i.q_j}{[r_{ij}^3 + (1/\gamma_{ij})^3]^{1/3}} \tag{2.21}$$

where $q_i$ and $q_j$ are atomic charges and $\gamma_{ij}$ is Coulomb parameter [22, 33].

**Force Field Optimization Procedure.** The forcefield is optimized using a quantum mechanics based database. The transferability of force field is supposed to be improved by using a more extensive quantum mechanics database. However, despite a significant improvement regarding the global optimization algorithm, still, reactive force field parameter sets suffer from major unphysical behavior [35]. Therefore, a change in the force field fitting procedures is required to make reactive force field a reliable predictive tool.

In this work, we performed a test on reactive force fields, using two parameterizations of ReaxFF to study the silicate dimerization reactions in the gas and aqueous phase, and compared the ReaxFF with the DFT calculations.

## 2.4 Calculation of Free Energy with Thermodynamic Integration

Free energy is a thermodynamic quantity that is equal to the difference between the internal energy of a system and the product of its temperature and entropy. It determines whether a reaction is spontaneous or not spontaneous. There are different methods to compute free energy differences from molecular simulations such as overlapping distributions, umbrella sampling and thermodynamic integration (TI) [36,37]. The last method has been used in this thesis and, therefore, we will consider thermodynamic integration in more detail.

Thermodynamic integration is a conceptually simple technique to calculate the difference in free energy between two stable states from molecular dynamics simulations. The free energy difference is calculated by defining a continuous and reversible path between two given states with potential energies $U_A$ and $U_B$ and integrating the potential functional as a function of a coupling parameter $\lambda$ along the path.

$$U(\lambda) = U_A + \lambda(U_B - U_A) \tag{2.22}$$

$\lambda$ is defined as a coupling parameter which ranges from 0 (system A) to 1 (system B), such that the potential energy as a function of $\lambda$ varies from the energy of system A and system B. $\lambda$ is not necessarily dimensionless but can also be simply a distance or an angle.

The canonical partition function of the system can be written as a general potential $U(\lambda)$,

$$Q(N, V, T, \lambda) = \frac{1}{\Lambda^{3N} N!} \int dr^N \exp\left[-\beta U(\lambda)\right] \tag{2.23}$$

Considering $F = -k_B T \ln Q$, the derivative of the free energy with respect to $\lambda$ can be written by

$$\begin{aligned} \left(\frac{\partial F(\lambda)}{\partial \lambda}\right)_{N,V,T} &= -\frac{1}{\beta}\frac{\partial}{\partial \lambda} \ln Q(N, V, T, \lambda) \\ = \frac{\int dr^N (\partial U(\lambda)/\partial\lambda) \exp[-\beta U(\lambda)]}{\int dr^N \exp[-\beta U(\lambda)]} &= \left\langle \frac{\partial U}{\partial \lambda} \right\rangle_\lambda \end{aligned} \tag{2.24}$$

By integrating the equation, the free energy difference between states A and B is given by

$$\triangle F(\lambda) = F_B(\lambda) - F_A(\lambda) = \int_{\lambda=0}^{\lambda=1} \left\langle \frac{\partial U(\lambda)}{\partial \lambda} \right\rangle_{\lambda} d\lambda \tag{2.25}$$

In this work, the constrained BOMD simulation is performed keeping the value of the reaction coordinate constant. The free energy profile was obtained with TI method integrating the averaged forces for a system of the silicate-oxygen interactions in water.

## 2.5 Simulating Rare Events

Molecular simulations are an ideal tool to obtain detailed information at the molecular scale which is often invisible to experiments. However, we are still far from a situation in which industries and pharmaceutical laboratories effectively design new materials and medicines based on molecular modeling. Present simulations techniques such as standard molecular dynamics can not reach time- and length-scales required to study complex chemical and biological processes, or they are based on inaccurate and oversimplified models which make them unreliable. Most of chemical reactions are considered as rare events. The straightforward molecular dynamics normally is not able to simulate these reactions at the same conditions where one can estimate the rate of reaction experimentally. In experiments, the rate constants for a system of billions of molecules, are determined by measuring the changes in the concentrations of reactants or products over a long period of time. In contrast, MD simulations are restricted to the small systems of a few hundreds atoms and to a short period of time. Therefore, the probability of observing a single event in these short simulations is imperceptible. Therefore, it is critical to define the simulation techniques that can selectively sample the special regions of the dynamical space of a system in order to detect a single event in such short simulations. In this work, we introduce the Transition interface sampling (TIS) and its improved version, Replica exchange transition interface sampling (RETIS).

## 2.6 Replica Exchange Transition Interface Sampling

One of the biggest drawbacks of molecular simulation is its limited time- and length-scale. This makes the chance that a spontaneous reactive event can be observed in a MD simulation negligible for almost all chemical and biological reactions that occur in nature or laboratory experiments. To overcome this limitation, one needs to set-up a unique systematic computational methodology that is able to tackle the time scale problem. Since the products of chemical reactions are often kinetically rather than thermodynamically determined, a standard equilibrium sampling of the configuration space will not be sufficient to make predictions about which products are formed and at which rate. On the other hand, the timescales of activated processes make standard molecular dynamics unfeasible. Over the last decades, several methods have been proposed in order to tackle the simulation timescale problem. For example, the parallel replica method [38] exploits the power of parallel processing to increase the molecular simulation time. Temperature-accelerated dynamics [39] accelerates rare events by increasing the temperature [40]. Thermodynamic integration [41] and umbrella sampling [36] enhance reactive events by perturbing the actual dynamics [42]. Using reweighting schemes, based on the laws of statistical physics, one can usually get exact results on statistics such as free energy barriers, but important information on the spontaneous dynamical process is usually lost. Moreover, free energies expressed as a low dimensional function of a set of reaction coordinates can be very misleading [40, 42]. The height of free energy barriers depend sensitively on the set of reaction coordinates that is chosen. As a result, Transition state theory (TST) is insufficient to make predictions about reaction rates in complex systems. The reactive flux method [37] is the standard approach to correct the TST expression. It complements the free energy calculation along a single reaction coordinate with the calculation of a dynamical transmission coefficient, by starting short trajectories from the maximum of the free energy barrier [42]. However, in complex systems the correct reaction coordinate can be exceedingly difficult to find. If the reaction coordinate does not capture the molecular mechanism, the biased sampling methods will suffer from substantial hysteresis when following the system over the barrier. Moreover, even if the free energy profile is obtained correctly for this particular (but wrong) reaction coordinate, the corresponding transmission coefficient will be very low, making an accurate evaluation problematic [42].

To overcome these difficulties, Chandler and coworkers developed the Transition path sampling (TPS) method. This technique gathers a collection of true dynamical unbiased trajectories connecting the stable states without any a priori assumption of the reaction coordinate [40]. From the ensemble of pathways, rate constants can be calculated and reaction mechanisms can be extracted [43].

The original TPS rate evaluation is based on the calculation of a time correlation function,

$$C(t) = \frac{\langle h_A(x_0) h_B(x_t) \rangle}{\langle h_A(x_0) \rangle} \tag{2.26}$$

where $h_A(x)$ and $h_B(x)$ are the characteristic functions of the two stable states, the product and the reactant state respectively, and $h_{A(B)}(t) = 1$ if $x \in A(B)$ and 0 otherwise, and $x_0$ and $x_t$ are phase points at the time $t = 0$ and $t$.

In the TPS framework $C(t)$ can be rewritten as an average in the path ensemble,

$$k_{AB}^{TPS}(t) = \frac{\mathrm{d}}{\mathrm{d}t} C(t) = \frac{\langle \dot{h}_B(x_t) \rangle_{AB}}{\langle h_B(x_{t'}) \rangle_{AB}} C(t') \tag{2.27}$$

where the subscript AB denotes an average in the ensemble of paths of length $t$ that start in A and visit B at least once. Time $t$ must be chosen in the region of $C(t)$ where it is increasing linearly with time. Time $t'$ is an arbitrary time in the region where $C(t)$ is significantly different from zero. The function $C(t')$ can be computed in the TPS scheme using the shooting algorithm in combination with umbrella sampling. Since $t' < t$, equation 2.27 reduces the time-window for which the correlation function needs to be computed. Hence, the expensive umbrella sampling can be performed with shorter paths of length $t'$.

TPS creates a large number of paths starting between two stable states A and B by using Monte Carlo (MC) algorithm that employs the so called shooting move. This works as follows. First an initial path is generated starting from the state A and reach to state B. Then, one takes a random point along the existing path and makes a small displacement to the all atomic momenta. The new path is obtained by integrating the equation of motion forward and backward. This new path will then be accepted or rejected in order to have the correct path probability. The procedure is iterated and the ensemble is gradually sampled.

However, quantitative analysis using transition path sampling used to be very expensive until the novel algorithms were developed by van Erp and coworkers. The main new algorithm is transition interface sampling which has turned path sampling into a powerful method to obtain quantitative results.

The TIS method is a powerful alternative to configuration space based approaches to treat rare event processes. The latter become problematic when many degrees of freedom participate in the reaction mechanism which is the case for many biological reactions, chemical reactions in a solvent, and nucleation. For these systems, it is very difficult to devise a good reaction coordinate which does not make the algorithms extremely inefficient [37]. In contrast, TIS is based on the sampling of dynamical MD trajectories using a MC sampling which is much less sensitive to the choice of RC [44]. TIS has significantly improved transition path sampling [43] by allowing variable path lengths and recasting the computation of the rate constants into fluxes through interfaces dividing the reactant and product state. In TIS, all path ensembles contain trajectories that start at the foot of reaction barrier from the reactant side and end there as well or end at the product region. In between start- and end-point the trajectory must have reached a certain threshold value (interface) along the progress coordinate, which differs for each ensemble. The sampling of trajectories is done using a TPS shooting algorithm, adapted for variable path lengths. This is basically a Monte Carlo algorithm in which you randomly pick a point of an old path, make a small random modification, and create a new trajectory by going forward and backward in time until reaching the first interface (at the reactant side) or the last interface (in the product region). The path is then accepted or rejected according to a detailed balance relation to ensure the correct weighting of the trajectories. But if the trajectory does not fulfil the ensemble specific threshold condition, it is always rejected. In that case, the old trajectory is counted again and the procedure is repeated like in standard MC. This approach ensures that we have a much higher chance to generate a valid trajectory at each trial than if we would just start from a random point within the reactant well. In each path-ensemble simulation the main property, that is calculated, is the conditional crossing probability. This is the chance that, in case you reach a certain threshold value along the progress coordinate, you make a little step further. The overall reaction rate is obtained by the product of the different crossing probabilities and a flux value. The nice feature of TIS is that it is exact: it will converge to the same result as an infinitely long straight-forward MD simulation but orders of magnitude faster.

As mentioned before, the TIS method is based on a flux calculation. In order to formulate a proper flux, one needs to redefine the correlation function dividing the all phase space into two overall states $\mathcal{A}$ and $\mathcal{B}$. Overall state $\mathcal{A}$ consists all phase space points inside the stable state A, but also all phase points that visit A, before reaching B when the equations of motion are integrated backward in time. Similarly, overall state $\mathcal{B}$ covers stable region B and all phase points, coming directly from this region in the past, without having been in A. The corresponding time correlation function is given by,

$$C(t) = \frac{\langle h_{\mathcal{A}}(x_0) h_{\mathcal{B}}(x_t) \rangle}{\langle h_{\mathcal{A}}(x_0) \rangle} \tag{2.28}$$

This correlation function is linear and the time derivative at $t = 0$ is given by,

$$\begin{aligned} k_{AB} &= \frac{\langle h_{\mathcal{A}}(x_0) \dot{h}_{\mathcal{B}}(x_0) \rangle}{\langle h_{\mathcal{A}}(x_0) \rangle} \\ &= \lim_{dt \to 0} \frac{1}{\mathrm{d}t} \frac{\langle h^b_{AB}(x_0) \theta(\lambda_B - \lambda(x_0)) \theta(\lambda(x_{dt})) - \lambda_B \rangle}{\langle h_{\mathcal{A}}(x_0) \rangle} \\ &= \frac{\langle h^b_{AB}(x_0) \dot{\lambda}(x_0) \delta(\lambda(x_0) - \lambda_B) \theta(\dot{\lambda}(x_0)) \rangle}{\langle h_{\mathcal{A}}(x_0) \rangle} \end{aligned} \tag{2.29}$$

The resulting expression is basically the effective positive flux (EPF) expression through the interface $\lambda_B$. An effective positive crossing is defined as the first crossing on the trajectory that transits from the stable state A to the stable state B. One can prove that equation 2.29 is equivalent to the product of the initial flux times the overall probability,

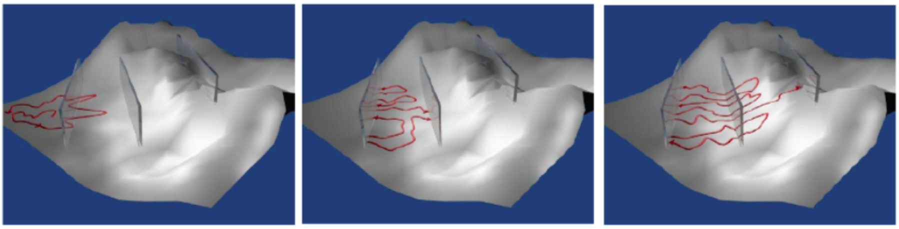

**Figure 2.2:** Graphical illustration of TIS trajectories on a free energy surface. The glassy plates represent the TIS interfaces. The first type of simulation (left), is a straightforward MD simulation which is required to calculate the flux $f_A$ through the first interface. The middle panel shows the path-sampling simulation which generates pathways that start at $\lambda_A$ and end at either $\lambda_A$ or $\lambda_1$ to obtain $\mathcal{P}_A(\lambda_1|\lambda_0)$. The last panel shows the next path-sampling simulation to calculate $\mathcal{P}_A(\lambda_2|\lambda_1)$. It generates pathways that start at $\lambda_A$ and cross $\lambda_1$ at least once. Picture taken from Ref. 45.

$$
\begin{aligned}
k_{AB} &= \frac{\langle \dot{\lambda}(x_0)\delta(\lambda(x_0)-\lambda_0)\theta(\dot{\lambda}(x_0))\rangle}{\langle h_{\mathcal{A}}(x_0)\rangle} \times \mathcal{P}_A(\lambda_B|\lambda_A) = f_A\,\mathcal{P}_A(\lambda_B|\lambda_A) \\
\mathcal{P}_A(\lambda_B|\lambda_A) &= \mathcal{P}_A(\lambda_n|\lambda_0) = \prod_{i=0}^{n-1} \mathcal{P}_A(\lambda_{i+1}|\lambda_i)
\end{aligned}
\tag{2.30}
$$

where the first term is the flux out of region A and can be calculated by standard molecular dynamics. $\lambda_A$ and $\lambda_B$ are the boundaries of regions A and B, respectively. $f_A$ is the escape flux through the first interface and $\mathcal{P}_A(\lambda_B|\lambda_A)$ is the overall crossing probability (see figure 2.2). This is the probability that whenever the system crosses $\lambda_A$, it will cross $\lambda_B$ before it crosses $\lambda_A$ again. As $\lambda_B$ is a surface at the other side of the barrier, this probability will be very small and can not be calculated directly. However, this probability is determined by a series of path sampling simulations using the factorization given in the second line. $\mathcal{P}_A(\lambda_{i+1}|\lambda_i)$ is a conditional crossing probability that can be calculated efficiently via path sampling. This theoretical technique has paved the way for several other related methods [46–48]. The efficiency of TIS is relatively insensitive to the choice of reaction coordinate, which is very advantageous in complex condensed systems where it is extremely difficult to find a proper reaction coordinate. A simple inter-atomic distance for a bond that has to break, will work for TIS while the other methods might need more complex reaction coordinates to describe the solvent rearrangement in the process. TIS method and its derivatives have already been applied to a variety of systems such as protein folding [49], nucleation [50], chemical reactions [51], and biochemical networks [47].

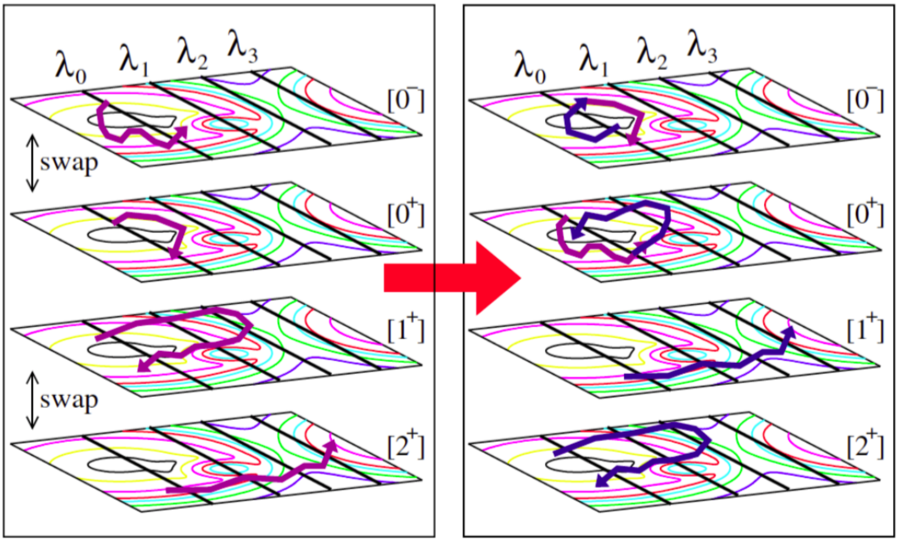

**Figure 2.3:** Illustration of the replica exchange move. The picture shows four possible paths on a free energy surface corresponding to different path ensembles (called $[0^-]$, $[0^+]$, $[1^+]$, $[2^+]$ which indicates which interface needs to be crossed (threshold condition) and in which direction they go ). In the next step the swaps are performed simultaneously yielding four new paths. Note that $[1^+]$ and $[2^+]$ both have moved to another reaction channel. Picture taken from Ref. 52.

In this work we used the replica exchange TIS (RETIS). It is a useful extension of the TIS method based on the replica exchange method. RETIS is more efficient than TIS, but has a somewhat more complicated implementation. It applies replica exchange moves between the different path simulations which can significantly improve the TIS efficiency. A crucial difference with the standard replica exchange is that instead of simulating systems at different temperatures, RETIS uses the different TIS path ensembles to attempt swaps between them. It is based on the fact that some trajectories, generated for one path ensemble, are also valid trajectories for another path ensemble. So if two simulations generate simultaneously two paths that are valid for each others path ensemble, these two paths can be swapped (figure 2.3). To this end, the initial MD simulation was replaced by another path ensemble, called $[0^-]$, that consists of all path that start at $\lambda_0 = \lambda_A$, then go in the opposite direction away from the barrier inside state $A$, and finally end at $\lambda_0$ again. The flux is then obtained from the average path length of the $[0^-]$ and $[0^+]$ ensembles [52, 53]. Since the dynamical process is now entirely defined by path simulations with different interface-crossing conditions, the exchange of trajectories between them becomes highly efficient [53, 54]. RETIS methodology avoids the need for additional simulations at elevated temperatures and even provides additional paths for free as for most swapping moves whole trajectories are being swapped. Only when a swapping between the $[0^-]$ and $[0^+]$ ensembles are attempted, two phase points are interchanged [53]. From the last point of the $[0^-]$ trajectory a new path in the $[0^+]$ is generated. Reversely, the first point of the old $[0^+]$ path will serve to generate a new path in the $[0^-]$ ensemble by integrating the equations of motion backward in time [53]. (figure 2.3). The swapping move does not only give two new trajectories for each path ensemble for free, but also tremendously reduces the correlations between the shooting moves. The correlation reduces sometimes by more than a factor of 150 as was found for the case of DNA denaturation [52].

The RETIS has become a very efficient approach to calculate quantitative properties, like reaction rates, and to analyze the complex reaction mechanism. In this work we employed a new implementation of the RETIS method in combination of CP2K to get a much more quantitative and deeper qualitative analysis of two fundamental processes: autoionization of water and silicate oligomerization in aqueous solution.

# Bibliography

[1] F. Jensen. *Introduction to Computational Chemistry*. Wiley-Interscience: New York, 1999.

[2] R. G. Parr and W. Yang. *Density Functional Theory of Atoms in Molecules*. Oxford University Press: New York, 1989.

[3] D. C. Young. *Computational Chemistry: A Practical Guide for Applying Techniques to Real-World Problems*. Wiley-Interscience: New York, 2001.

[4] J. C. Slater. The theory of complex spectra. *Phys. Rev.*, 34:1293–1322, 1929.

[5] L. H. Thomas. The calculation of atomic fields. *Proc. Cambridge Phil. Soc.*, 23:542–548, 1927.

[6] E. Fermi. Un metodo statistico per la determinazione di alcune priopriet`a dell'atomo. *Rend. Accad. Naz. Lincei*, 6:602–607, 1927.

[7] P. Hohenberg and W. Kohn. Inhomogeneous electron gas. *Phys. Rev.*, 136:B864–B871, 1964.

[8] W. Kohn and L. J. Sham. Self-consistent equations including exchange and correlation effects. *Phys. Rev.*, 140:A1133–A1138, 1965.

[9] D. Ceperley and B. Alder. Quantum monte carlo. *Science*, 231:555–560, 1986.

[10] A. D. Becke. A new mixing of Hartree-Fock and local density functional theories. *J. Chem. Phys.*, 98:1372–1377, 1993.

[11] A. D. Becke. Density-functional thermochemistry. III. the role of exact exchange. *J. Chem. Phys.*, 98:5648–5652, 1993.

[12] A. Szabo and N. S. Ostlund. *Modern Quantum Chemistry, Introduction to Advanced Electronic Structure Theory*. McGraw-Hill: New York, 1989.

[13] E. van Lenthe and E. J. Baerends. Optimized Slater-type basis sets for the elements 1-118. *J. Comput. Chem.*, 24:1142–1156, 2003.

[14] G. Maroulis. *Computational Aspects of Electric Polarizability Calculations: Atoms, Molecules and Clusters*. IOS Press: Amsterdam, 2006.

[15] G. te Velde, F. M. Bickelhaupt, E. J. Baerends, C. Fonseca Guerra, S. J. A. van Gisbergen, J. G. Snijders, and T. Ziegler. Chemistry with ADF. *J. Comp. Chem.*, 22:931–967, 2001.

[16] J. VandeVondele, M. Krack, F. Mohamed, M. Parrinello, T. Chassaing, and J. Hutter. Quickstep: Fast and accurate density functional calculations using a mixed gaussian and plane waves approach. *ChemPhysChem*, 167:103–128, 2005.

[17] CP2K: High Performance Computing, http://www.nanosim.mat.ethz.ch/ research/cp2k.

[18] A. Leach. *Molecular Modelling: Principles and Applications*. Pearson: Essex, 1996.

[19] W. D. Cornell, P. Cieplak, C. I. Bayly, I. R. Gould, K. M. Merz, D. M. Ferguson, D. C. Spellmeyer, T. Fox, J. W. Caldwell, and P. A. Kollman. A second generation force field for the simulation of proteins, nucleic acids, and organic molecules. *J. Am. Chem. Soc.*, 117:5179–5197, 1995.

[20] B. R. Brooks, R. E. Bruccoleri, B. D. Olafson, D. J. States, S. Swaminathan, and M. Karplus. Charmm: A program for macromolecular energy, minimization, and dynamics calculations. *J. Comput. Chem.*, 4:187–217, 1983.

[21] W. L. Jorgensen, D. S. Maxwell, and J. Tirado-Rives. Development and testing of the OPLS all-atom force field on conformational energetics and properties of organic liquids. *J. Am. Chem. Soc.*, 118:11225–11236, 1996.

[22] A. C. T. van Duin, S. Dasgupta, F. Lorant, and W. A. Goddard. ReaxFF: A reactive force field for hydrocarbons. *J. Phys. Chem. A*, 105:9396–9409, 2001.

[23] K. Vanommeslaeghe, O. Guvench, and A. D. MacKerell. Molecular mechanics. *Curr Pharm Des.*, 20:3281–3292, 2014.

[24] B. Kirchner and J. Vrabec. *Multiscale Molecular Methods in Applied Chemistry*. Springer-Verlag Berlin Heidelberg, 2012.

[25] P. Ehrenfest. Bemerkung über die angenäherte gültigkeit der klassischen mechanik innerhalb der quantenmechanik. *Zeitschrift für Physik*, 45:455–457, 1927.

[26] R. Car and M. Parrinello. Unified approach for molecular dynamics and density-functional theory. *Phys. Rev. Lett.*, 55:2471–2474, 1985.

[27] T. D. Kühne, M. Krack, F. R. Mohamed, and M. Parrinello. Efficient and accurate Car-Parrinello-like approach to Born-Oppenheimer molecular dynamics. *Phys. Rev. Lett.*, 98:066401, 2007.

[28] J. Hutter, M. Iannuzzi, F. Schiffmann, and J. VandeVondele. CP2k: Atomistic simulations of condensed matter systems. *WIREs Comput Mol Sci*, 4:15–25, 2014.

[29] D. Marx and J. Hutter. *Ab Initio Molecular Dynamics: Basic Theory and Advanced Methods*. Cambridge University Press, 2009.

[30] J. C. Fogarty, H. M. Aktulga, A. Y. Grama, A. C. T. van Duin, and S. A. Pandit. A reactive molecular dynamics simulation of the silica-water interface. *J. Chem. Phys*, 132:4704–4714, 2010.

[31] A. C. T. van Duin. *ReaxFF User Manual*. Materials and Process Simulation Center, 2002.

[32] A. C. T. van Duijn, S. Dasgupta, F. Lorant, and W. A. Goddard. ReaxFF reactive force field for hydrocarbons. *J. Phys. Chem. A*, 105:9396–9409, 2001.

[33] A. C. T. van Duin, A. Strachan, S. Stewman, Q. Zhang, X. Xu, and W. A. Goddard. ReaxFF$_{SiO}$ reactive force field for silicon and silicon oxide systems. *J. Phys. Chem. A*, 107:3803–3811, 2003.

[34] W. J. Mortier, S. K. Ghosh, and S. Shankar. Electronegativity equalization method for the calculation of atomic charges in molecules. *J. Am. Chem. Soc.*, 108:4315–4320, 1986.

[35] M. Moqadam, E. Riccardi, T. T. Trinh, P.-O. Åstrand, and T. S. van Erp. A test on reactive force fields for the study of silica dimerization reactions. *J. Chem. Phys.*, 143:184113–8, 2015.

[36] G. M. Torrie and J. P. Valleau. Nonphysical sampling distributions in Monte Carlo free-energy estimation - Umbrella sampling. *Chem. Phys. Lett.*, 23:187–199, 1977.

[37] D. Frenkel and B. Smit. *Understanding Molecular Simulation, Second Edition: From Algorithms to Applications*. Academic Press: San Diego, 2005.

[38] A. F. Voter. Parallel replica method for dynamics of infrequent events. *Phys. Rev. B*, 57:R13985–R13988, 1998.

[39] A. F. Voter and M. R. Sørensen. Accelerating atomistic simulations of defect dynamics: hyperdynamics, parallel replica dynamics, and temperature-accelerated dynamics. *Mat. Res. Soc. Symp. Proc.*, 538:427–440, 1999.

[40] D. Moroni, T. S. van Erp, and P. G. Bolhuis. Investigating rare events by transition interface sampling. *Physica A*, 340:395–401, 2004.

[41] E. A. Carter, G. Ciccotti, J. T. Hynes, and R. Kapral. Constrained reaction coordinate dynamics for the simulation of rare events. *Chem. Phys. Lett.*, 156:472–477, 1989.

[42] A. Lervik and T. S. van Erp. Gluing potential energy surfaces with rare event simulations. *J. Chem. Theory Comput.*, 11:2440–2450, 2015.

[43] C. Dellago, P. G. Bolhuis, F. S. Csajka, and D. Chandler. Transition path sampling and the calculation of rate constants. *J. Chem. Phys.*, 108:1964–1977, 1998.

[44] T. S. van Erp. Efficiency analysis of reaction rate calculation methods using analytical models I: The two-dimensional sharp barrier. *J. Chem. Phys.*, 125:174106–20, 2006.

[45] T. S. van Erp, T. P. Caremans, C. E. A. Kirschhock, and J. A. Martens. Prospects of transition interface sampling simulations for the theoretical study of zeolite synthesis. *Phys. Chem. Chem. Phys.*, 9:1044–1051, 2007.

[46] D. Moroni, P. G. Bolhuis, and T. S. van Erp. Rate constants for diffusive processes by partial path sampling. *J. Chem. Phys.*, 120:4055–4065, 2004.

[47] R. J. Allen, P. B. Warren, and P. R. ten Wolde. Sampling rare switch ing events in biochemical networks. *Phys. Rev. Lett.*, 94:018104–4, 2005.

[48] T. S. van Erp and P. G. Bolhuis. Elaborating transition interface sampling methods. *J. Comput. Phys.*, 205:157–181, 2005.

[49] P. G. Bolhuis. Transition-path sampling of beta-hairpin folding. *Proc. Natl. Acad. Sci.*, 100:12129–12134, 2003.

[50] D. Moroni, P. R. ten Wolde, and P. G. Bolhuis. Interplay between structure and size in a critical crystal nucleus. *Phys. Rev. Lett.*, 94:235703–4, 2005.

[51] T. S. van Erp. *Solvent effects on chemistry with alcohols*. PhD thesis, Universiteit van Amsterdam, 2003.

[52] T. S. van Erp. Reaction rate calculation by parallel path swapping. *Phys. Rev. Lett.*, 98:268301–4, 2007.

[53] T. S. van Erp. *Dynamical Rare Event Simulation Techniques for Equilibrium and Nonequilibrium Systems*, pages 27–60. John Wiley & Sons, Inc., 2012.

[54] T. S. van Erp. Efficient path sampling on multiple reaction channels. *Comput. Phys. Commun.*, 179:34–40, 2008.

# Chapter 3

# A Test on Reactive Force Fields for the Study of Silicate Dimerization Reactions

Mahmoud Moqadam, Enrico Riccardi, Thuat Trinh, Per-Olof Åstrand,
Titus S. van Erp

J. Chem. Phys. 143, 184113 (2015)

**Abstract -** We studied silicate dimerization reactions in the gas and aqueous phase by density functional theory (DFT) and reactive force fields based on two parameterizations of ReaxFF. For each method (both ReaxFF force fields and DFT) we performed constrained geometry optimizations, which were subsequently evaluated in single point energy calculations using the other two methods. Standard fitting procedures will typically compare the force field energies and geometries with those from quantum mechanical data after a geometry optimization. The initial configurations for the force field optimization are usually the minimum energy structures of the ab initio database. Hence, the ab initio method dictates which structures are being examined and force field parameters are being adjusted in order to minimize the differences with the ab initio data. As a result, this approach will not exclude the possibility that the force field predicts stable geometries or low transition states which are realistically very high in energy and, therefore, never considered by the ab initio method. Our analysis reveals the existence of such unphysical geometries even at unreactive conditions where the distance between the reactants is large. To test the effect of these discrepancies, we launched molecular dynamics simulations using DFT and ReaxFF and observed spurious reactions for both ReaxFF force fields. Our results suggest that the standard procedures for parameter fitting need to be improved by a mutual comparative method.

## 3.1 Introduction

The silicate oligomerization reaction is a key elementary reaction in sol-gel chemistry and zeolite synthesis [1]. Therefore, understanding how the silicate oligomers grow is of fundamental scientific and technological importance. The first step in the silicate oligomerization mechanism is the formation of the SiO$-$Si linkage between the reactants to form a five-coordinated silicon complex which is an essential intermediate in the condensation reaction. Numerous theoretical studies have investigated the mechanism of the silicate-based reaction [2–5], where the quantum mechanical calculations rely mostly on density functional theory (DFT) [6]. Quantum chemical calculations of chains, rings, and the cubic cage were reported by Pereira et al. [7]. The mechanism of silicate oligomerization reactions have been studied using the BLYP functional and a continuum solvation model COSMO (Conductor-like Screening MO method) to mimic the methanol environment.

Tossell [8] reported on the energies of the dimerization reaction of monosilic acid, in the gas-phase and aqueous solution, over a range of temperatures and dielectric constants, using the BLYP and B3LYP functionals and the COSMO model to approximate hydration energies in aqueous solution. In that study the free energy of reaction changes by varying temperature and dielectric constants of the solvent. An ab initio study of the kinetics and mechanisms of quartz dissolution in basic pH solutions is reported by Xiao and Lasaga [9] at the MP2/HF/6-31G* level of theory and the catalytic effect of $OH^-$ in promoting the dissolution process was specifically addressed. Trinh et al. performed a DFT study on this reaction for both the gas phase complemented by a COSMO model and the silicate-water interface using 6-31+G(d,p) and DZVP-MOLOPT basis sets respectively [1, 10]. They provided thermodynamics, kinetics, and mechanism of the reaction pathway for the anionic bond formation of siliceous oligomers. Recently, a study on the conformational dependence of the silicate oligomerization reaction routes has been reported by Hu et al. [11] using the B3LYP functional and the 6-311++G(2d,2p)/aug-cc-pVT(+d)Z basis sets. Conformational dependence of the dimerization reaction is proposed in view of hundreds of conformations with various inter- and intramolecular hydrogen bonding patterns along the reaction routes.

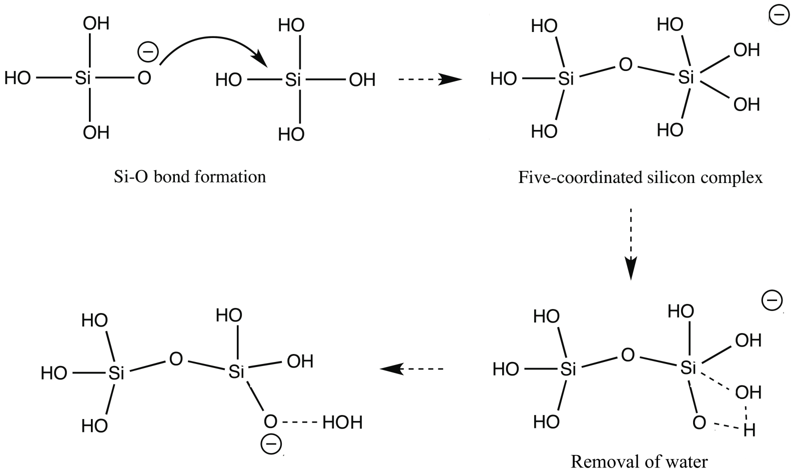

**Figure 3.1:** The anionic mechanism of silicate dimerization reaction. We focus on the formation of of five-coordinated silicate complex in this work.

Whereas calculations on the quantum level provide useful insight and quantitative data for the energy barriers for the elementary steps, the simulations of sol-gel chemistry or zeolite synthesis requires a series of such elementary reactions. To simulate such complex reaction networks one can either rely on kinetic Monte Carlo approaches [1], in which rate constants from quantum calculations are the main input, or use atomistic molecular dynamics (MD) simulations. In MD simulations one can either rely on calculating the interatomic forces by DFT methods, e.g. in the Car-Parrinello approach [12], or by a force field (classical MD). Due to the computational expense, DFT-based MD is limited to a few hundred of atoms which can be simulated for several picoseconds whereas classical MD simulations can treat millions of atoms upto the millisecond timescale [13, 14].

For the system studied here involving chemical reactions, however, a reactive force field would be required. Reactive force fields are computationally more expensive than nonreactive force fields and also their accuracy is not yet at the same level. It requires a non-trivial design of appropriate interaction functions with adjustable parameters followed by fitting procedures to quantum mechanical or experimental data. Still, molecular simulations based on reactive force fields could in principle give a much more detailed molecular description of the complex oligomerization process than kinetic Monte Carlo. Among the different types of reactive force fields, we have the empirical valence bond (EVB) method [15,16], as well as a variety of methods based on conserving the molecular bond order including the Tersoff potential [17], the Brenner potential [18] with the subsequent reactive empirical bond-order (REBO) potential [19], the bond-order potential (BOP) by Pettifor and coworkers [20], and the bond-order conservation/Morse potential (BOC-MP) [21] rephrased as the unity bond-index/quadratic exponential potential (UBI-QEP) method [22].

For silicon, the reactive Stillinger-Weber force includes both two-body and three-body terms to account for the rearrangement of Si−Si bonds [23] and it has for example been applied to fluorine [24] and hydrogen [25] interactions on a Si surface. Subsequently, the Tersoff potential was originally developed for Si [17] and the Brennner force field has been extended to include Si−C−H interactions [26, 27] as well as Si−F/Cl interactions [28].

The ReaxFF [29] combines the bond-order approach with a charge-equilibration method [30] to include also electrostatics in the force field, and it has been applied to a wide range of different types of chemical reactions [31–35]. Its accuracy is claimed to be very close to that of quantum mechanics predictions [36], though there is not a unique parameter set. For instance, van Duin et al. fitted the ReaxFFSiO reactive force field parameter set to simulate the silicon and silicon oxide systems [37, 38]. Fogarty et al. [39] used these force fields in reactive molecular dynamics (MD) simulations to analyze the changing of chemical composition for the Si/SiO/SiN interactions with water and $Na^+$ (ReaxFF1). Larsson et al. [40] improved the parameter fitting procedure using genetic algorithms leading to the SiOH ReaxFF force field (ReaxFF2).

The fitting of a force field is in general a non-trivial task, exemplified by the parametrization of atomic charges in an electronegativity equalization scheme [41]. In quantum chemistry, unphysical chemical structures are avoided efficiently by the Pauli exclusion principle, but for a reactive force field also in practice non-existing oxidation states and chemical bonds have to be included in the parametrization, which is a formidable task. Hereby, a reliable procedure for validation of a reactive force field is essential.

Here, we perform an alternative test of the reactive force fields parameter sets based on mutual single-point energy calculations. As benchmark system we took the initial step of silicate oligomerization reaction which involves the formation of five-coordinated silicate complex (see figure 3.1). For all our gas phase geometries we enforced the reaction by constraining the intermolecular distance between the anion oxygen and the silicon belonging to the opposite molecule. In our analysis, the reference geometries are generated both from DFT optimization and from the reactive force fields. The rational behind this approach is that it is directly related to hybrid classical-QM methodologies such as the Li and Yang approach [42] and the QuanTIS method [43]. These methods are exact, regardless the accuracy of the classical force field, but discrepancies between the energies of single point evaluations will affect the efficiency of these methodologies.

Since the energetic differences have been found to be rather high, we also evaluated the qualitative behavior of the two force fields by comparing DFT-based MD and simulations based on the two ReaxFF force fields. Both reactive force fields simulations show spurious chemical reactions. We will discuss these results in detail and propose a paradigmatic change for parameter fitting to develop more reliable reactive force fields.

## 3.2 Computational Details

### 3.2.1 Gas Phase

Here we briefly summarize the computational chemistry techniques used to study the dimer formation from one silicic acid $Si(OH)_4$ and its deprotonated form $Si(OH)_3O^-$. All DFT and ReaxFF calculations were performed using the Amsterdam Density Functional (ADF) package [44]. For the DFT calculations we applied the exchange-correlation functional by Becke, Lee, Yang and Parr (BLYP) [45] and the three-parameter version of this functional B3LYP [46]. The latter mixes the BLYP functional with exact exchange from Hartree-Fock which has shown to improve the descriptions of the reaction profiles and especially of geometries, activation energies, heats of reaction, and vibrational properties of various molecules [47]. Grimme's dispersion correction (DFT-D3-BJ) [48] provided a further refinement upon our DFT calculations as it gives an effective way to incorporate dispersion interactions. It should be noted that dispersive corrections were absent in the DFT dataset used for the ReaxFF1 and ReaxFF2 parametrizations. However, the dispersion energies are relatively small. Two Slater Type Orbital (STO) basis sets, TZ2P and QZ4P [49–52] were used. Slater-type functions are considerably more diffuse than a corresponding Gaussian basis set and give consistent and rapidly converging results [53].

To investigate the energy barrier of the dimerization reaction, we changed the distance between the anion oxygen and the silicon of the other molecule stepwise with interval of 0.2 Å from 3.3 Å to 1.8 Å. For each value we performed an energy minimization while keeping the silicon-oxygen distance fixed. The anion oxygen at larger silicate separation determined the target oxygen defining the reaction coordinate as the $|\mathrm{Si}-\mathrm{O}|$ distance. At smaller distances we occasionally observed proton transfer from a nearby oxygen to the target oxygen, basically changing the ionic character of the oxygens. The reaction coordinate remained, however, based on the original target atoms assigned at large separation distance.

In our constrained minimization procedure, each configuration with a fixed value of the $|\mathrm{Si-O}|$ distance was obtained from the previous optimized geometry with the reaction coordinate being 0.2 Å larger. However, whenever we observed discontinuous jumps in the energy profile, a backward step was performed. The procedure has been stopped once the resulting energy profile was smooth and presumably close to the global minimum. However, this is strictly speaking not essential for the comparison between DFT and the reactive force fields since our analysis is based on single-point calculations. We checked this analysis from both sides, i.e. we either used the optimized geometries from DFT as an input to compute the energies of ReaxFF or we used the optimized geometries obtained from one of the ReaxFF force fields and computed single point calculations using DFT and the other ReaxFF force field.

### 3.2.2 Aqueous Solution

We performed DFT-based MD simulations using Quickstep [54] which is a part of the CP2K program package. [55] We used the Goedecker-Teter-Hutter (GTH) pseudopotentials [56, 57], the BLYP functional [45, 46] uses the Grimme's D2 dispersion model [58] and a DZVP-MOLOPT basis set [59]. The BLYP functional has proven to give an accurate description of the structure and dynamics of water and of the silicate-water interaction [60]. A plane-wave cutoff of 400 Ry was used. The simulations were performed using a cubic simulation box of $13\times13\times13$ Å$^3$ containing $\mathrm{Si(OH)_4}$, its deprotonated form $\mathrm{Si(OH)_3O^-}$, $\mathrm{Na^+}$ ion and 64 water molecules. A Nosé-Hoover thermostat [61] was used to maintain the temperature at 350 K. The system was equilibrated for 10 ps prior to a 50 ps production run using a 1.0 fs time step.

Since the time scales at which the silicate oligomerization occur is not accessible with current ab initio molecular dynamics methods, the constrained MD method is used to force the reaction [62]. Therefore, the $\mathrm{SiO-Si}$ distance was chosen as the reaction coordinate for the formation of five-coordinated silicate complex. The constrained MD simulation is performed keeping the value of the reaction coordinate constant. A 5 ps equilibrium run was followed by a 40 ps production run. The averaged constrained force was calculated for the production runs. The free energy profile was obtained with the thermodynamic integration method based on the following equation [63]:

$$\Delta G \approx -\int_{\xi_1}^{\xi_2} \langle f(\xi) \rangle \, d\xi \tag{3.1}$$

where $f$ is the constrained force and $\xi$ is the reaction coordinate. The integration was performed numerically by applying a polynomial fit through the calculated average forces.

The ReaxFF MD simulations were performed at the same conditions as the DFT-based MD simulations. Still there were some differences in the simulation setup other than the force field. For instance, we used a Berendsen thermostat [64] instead of Nosé-Hoover. In principle a Nosé-Hoover thermostat is preferred since it exactly generates the Boltzmann distribution unlike the Berendsen thermostat [65]. The Nosé-Hoover thermostat, on the other hand, can have ergodicity problems which can be effectively suppressed by the so-called Nosé-Hoover chain algorithm (NHC) [66]. The NHC thermostat is, however, not yet implemented in the ADF software. For our purposes the Berendsen thermostat is sufficient as our conclusions regarding the ReaxFF MD simulations will be mainly qualitative. All the ReaxFF MD simulations were equilibrated for 50 ps prior to 250 ps production run.

For completeness it should be reported that, according to suggested values in literature [67], we employed a time step of 0.1 fs in ReaxFF simulations versus the 1.0 fs of DFT-based MD. The argument for this small time step in ReaxFF is that updates in the bond order and its dependent quantities need to occur very regularly [67]. We find this argument not so satisfying. The gradient of the ReaxFF potential depends on the derivatives of the bond order parameters. If the generated potential energy surface is similar to that of DFT, then both the force and the derivatives of the bond order parameter should be slowly varying for time steps that are functioning for DFT-based MD. Hence, the need of time steps smaller than DFT seems to imply that the potential energy surface of ReaxFF is, even after parameter fitting, different from the DFT potential energy surface, e.g. presence of steeper gradients. Since the computational cost of a ReaxFF MD step is orders of magnitude lower than that of DFT-based MD, we had not the need to investigate the effects of larger time steps in ReaxFF for the here investigated systems.

## 3.3 Results and Discussion

### 3.3.1 Gas Phase

The oligomerization reaction occurs through two reaction steps. The first step is the formation of the SiO$-$Si bond between two molecules. During this step one oxygen atom of monomeric silicic acid connects with one silicon atom of another silicate to form a stable five-coordinated silicon intermediate. The second step is the removal of water to form the dimer species [68]. Here we focused on the first step of this reaction. The DFT calculations show that the transition state point is at 2.38 Å. Starting from the constrained geometries at the distances 1.9 Å and 3.3 Å we also let the system fully relax in unconstrained geometry optimization runs. This resulted in final equilibrium distances of 1.83 Å and 3.15 Å, respectively. The bond length of $|\mathrm{Si-O}|$ around fivefold-coordinated Si was around 1.83 Å, whereas other Si$-$O bonds lengths were around 1.68 Å. Xiao and Lasaga, studied the geometry elongations of the bonds around five-coordinated Si at the transition state point [9, 69] and reported values of 1.70 and 1.61 Å, for the bond length of |Si−O| and other Si−O bonds, respectively. The activation barrier of the formation of the dimer in our study is 7.07 kcal/mol. Figure 3.2 shows the details of this reaction path which value is comparable to that of Xiao and Lasaga (6.2-9.7 kcal/mol) [9, 69] and Hu et al. (5.0 kcal/mol) [11], respectively.

Figure 3.2 compares the energy profiles using the BLYP and B3LYP functionals and two different basis sets. The DFT results show reasonable agreement between B3LYP and BLYP with a difference of 0.55 kcal/mol for the barrier and 1.85 kcal/mol for the reaction

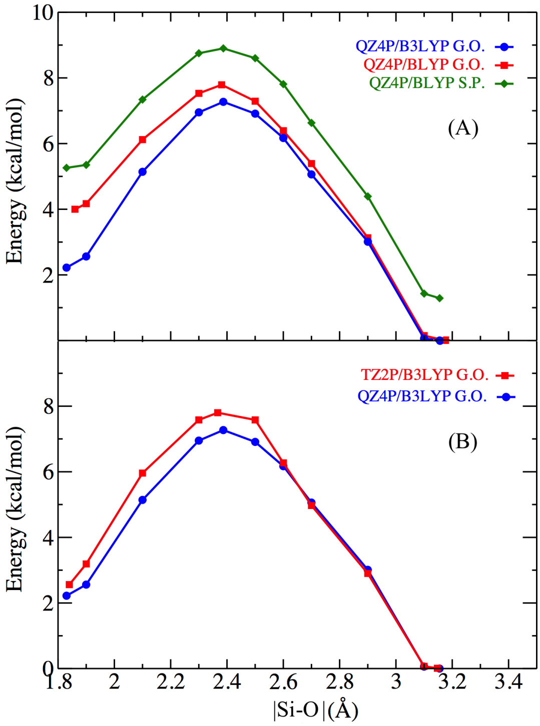

**Figure 3.2:** Energy versus |Si−O| distance. Geometry optimizations (G.O.) and single-point (S.P.) calculations are compared for different DFT functionals and basis-sets. The reference state $E = 0$ is chosen as the unconstrained optimized geometry around 3.15 Å. (A) compares the results of the exchange correlation functionals BLYP and B3LYP showing a difference in the energy barrier ( from large to small distances) within 1 kcal/mol while reaction energy has a difference around 2 kcal/mol. The single point BLYP energy calculations based on the B3LYP geometries show an overall upward shift by 1 kcal/mol compared to the optimized BLYP energies. (B) plots the B3LYP energies for two different basis sets showing a decent convergence at TZ2P/QZ4P level since energy differences at transition state and reactant state are within 0.44 kcal/mol.

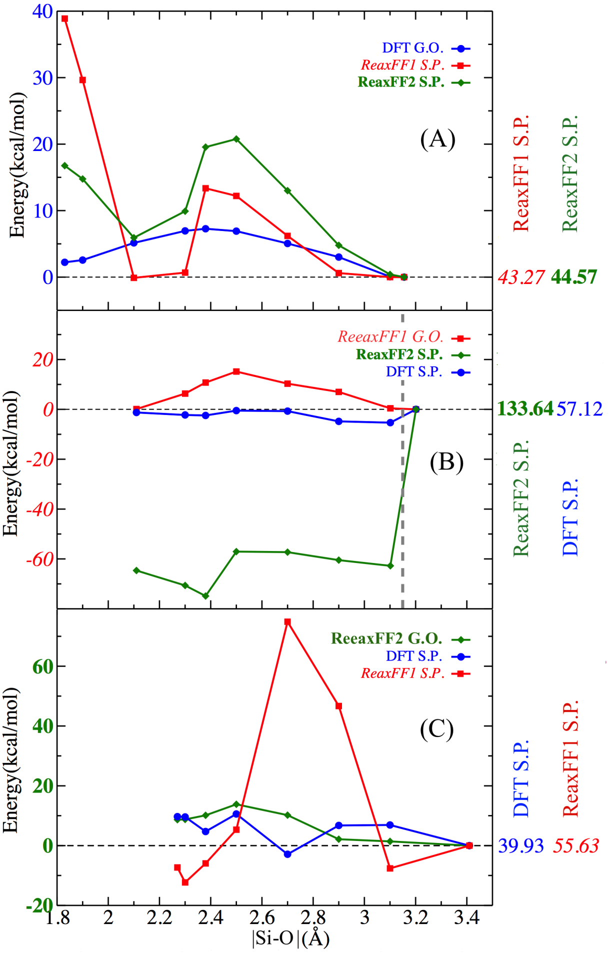

**Figure 3.3:** Energy profiles for the silicate dimer formation comparing DFT (blue), ReaxFF1 (italic, red), and ReaxFF2 (bold, green). DFT calculations are at the B3LYP/QZ4P level. The same reference energy is used as in figure 3.2. At each panel one of the methods is fully optimized (energy scale at the left axis) while these optimized geometries were used for single point calculations using the two other methods. The curves were shifted to overlap at the point describing the largest separation in order to compare the relative trend. The absolute energy scale, which defines E = 0, is simply the energy difference between different methods at the optimized geometries. Both the relative trend and the absolute energy differences are rather large considering the small system size. The vertical dashed line shows the geometric discontinuity along the reaction path (see figure 3.4).

energy. If the optimized geometries of B3LYP are used as BLYP single point calculations, we observe an approximate overall shift by 1 kcal/mol. Also the basis set convergence

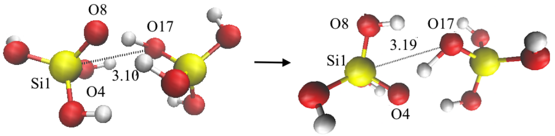

**Figure 3.4:** Geometries of the optimized ReaxFF1 geometry at 3.1 Å and the fully optimized geometry without constraining the distance. Despite that the structures only differ by 0.1 Å in the distance between atom $Si_1$ and $O_{17}$ the overall configurations has changed significantly due a proton transfer from $O_8$ to $O_4$ which happened spontaneously when the molecules where moved closer. Despite this change, only small changes in the energy are observed for the ReaxFF1 and DFT calculations while there is more than 60 kcal/mol difference between these structures for the ReaxFF2 force field.

is satisfactory with only 0.44 kcal/mol difference for the barrier when comparing TZ2P and QZ4P. Figure 3.3A illustrates the energy profiles of the ReaxFF1 and ReaxFF2 constrained geometry optimization. It shows much stronger variations compared to the DFT results, especially if we consider the absolute energy scales (as explained in the caption of figure 3.3) at the right-hand side. The energy difference between ReaxFF1 and ReaxFF2 is notable as can be seen in figure 3.3B where the optimized structure of ReaxFF1 with a $|\mathrm{Si{-}O}|$ distance of 3.2 Å lies about 133 kcal/mol higher than the optimized structure of ReaxFF2. However, the ReaxFF2 energy shows a jump downwards when the oxygen and silicon are moved 0.1 Å closer. Figure 3.4 provides some explanation of this jump; despite the reaction coordinate only differs by 0.1 Å, a spontaneous proton transfer occurs for ReaxFF1 optimization when the molecules are closer, resulting in a different structure.

### 3.3.2 Aqueous Solution

The considerable deviations between single point energies between DFT and the ReaxFF does not necessarily imply that MD simulations using these ReaxFF force fields will give similar discrepancies. An MD simulation will not generate configurations which are energetically not acceptable by its own force field. In addition, even if the configurations sampled are different, the differences might not be very relevant. For instance two water models using harmonic $|\mathrm{OH}|$ stretching potentials with large force constants and slightly different equilibrium bond lengths will also produce large single point energy deviations, but might still produce almost the same radial distribution functions and diffusion constants.

Hereby, we first used DFT based MD using the CP2K package and looked at the solvation and silicate dimerization reactions in explicit water. An additional $Na^+$ counter ion was added to the system to ensure charge neutrality. Sodium is a commonly used additive for synthesizing zeolites and its effect has been reported [70, 71] to reduce the rate of formation of the smaller silicate oligomers [63]. Figure 3.5 shows the calculated constraint force and the associated free-energy profile along the reaction path of the first step

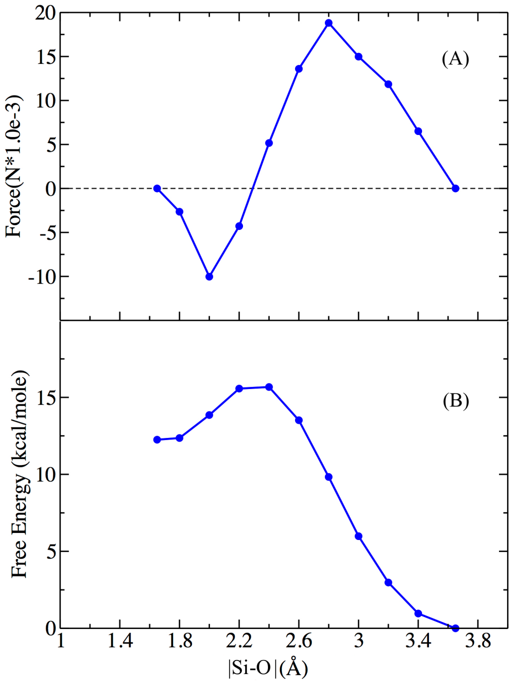

**Figure 3.5:** DFT-MD calculated (A) constrained force profiles along the reaction coordinates. (B) free energy profiles as functions of the reaction coordinate for $Si(OH)_4+Si(OH)_3O^{-}+Na^{+}+64H_2Os$ in a 13×13×13 Å$^3$ cubic box and at T=350 K.

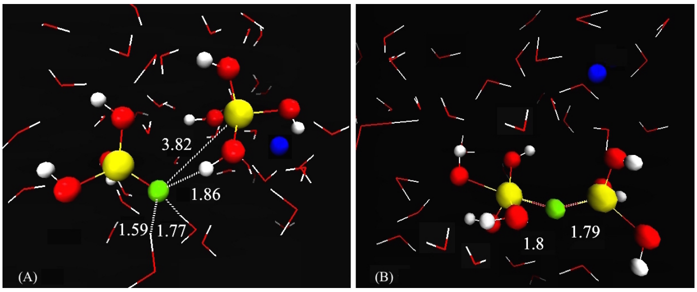

**Figure 3.6:** Representative snapshots of the Si−O bond formation step for the dimer reaction using DFT-simulation. The reactive oxygen is shown in green colour. Water molecules are shown as lines. (A) shows the reactants state. The reactive oxygen has three hydrogen bonds. (B) shows the five-coordinated silicate complex. Selected distances are shown in Å.

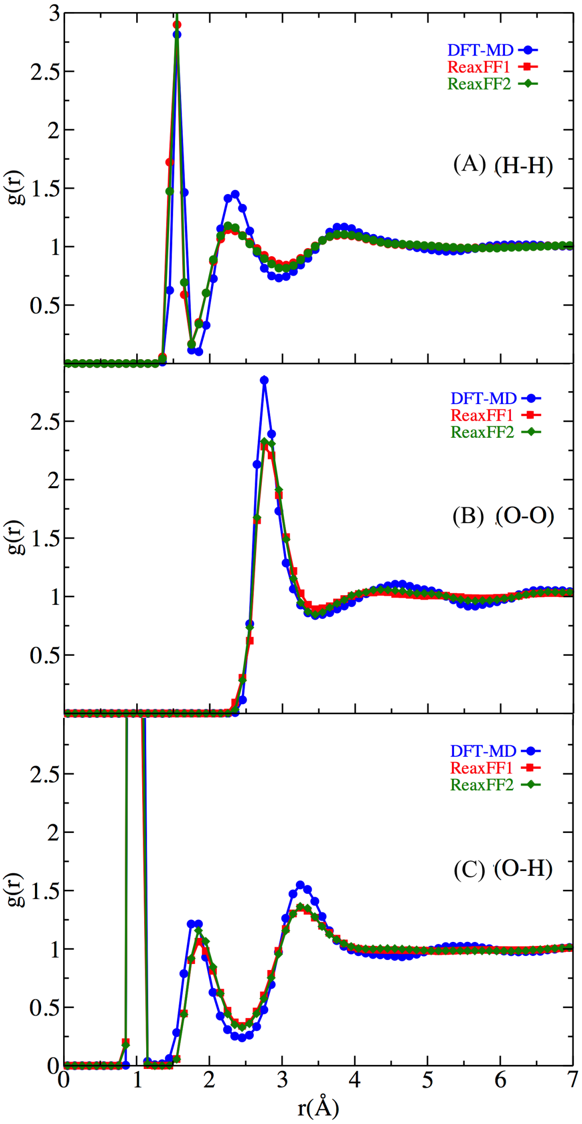

**Figure 3.7:** Radial distribution function for (A) hydrogen-hydrogen H−H, (B) oxygen-oxygen O−O and (C) oxygen-hydrogen O−H pair at T=350 K.

of silicate dimerization reaction by using Eq. (1). The reaction mechanism is controlled by a constrained value of the SiO−Si distance. We observe that at 350 K, the activation barrier of the formation of five-coordinated silicate complex is around 15.5 kcal/mol. Previous studies reported the first barrier for the anionic mechanism of the dimerization reaction in pure water as only 10.51 kcal/mol and 14.1 kcal/mole in the presence of $Na^+$ counter ion [63].

Trinh et al. [60] showed that the free energy of the first step of the silicate dimerization is unfavorable and our results are consistent for pure water. Figure 3.6 shows the representative snapshots for the first step of the silicate dimerization reaction including the production of the silicate complex. That study shows that the $Na^+$ can be in the second hydration shell of the anion oxygen or further away. In the first case, the reactive oxygen can have up to three hydrogen bonds which makes the SiO−Si bond formation step more favorable than the direct coordination of the sodium ion [63]. Figure 3.6 shows the number of hydrogen bonds for the reactive oxygen (we only counted the bonds that are shorter than the average hydrogen bond length in water which is 1.97 Å). The high observed energy barrier might be due to the electrostatic interaction of the $Na^+$ cation

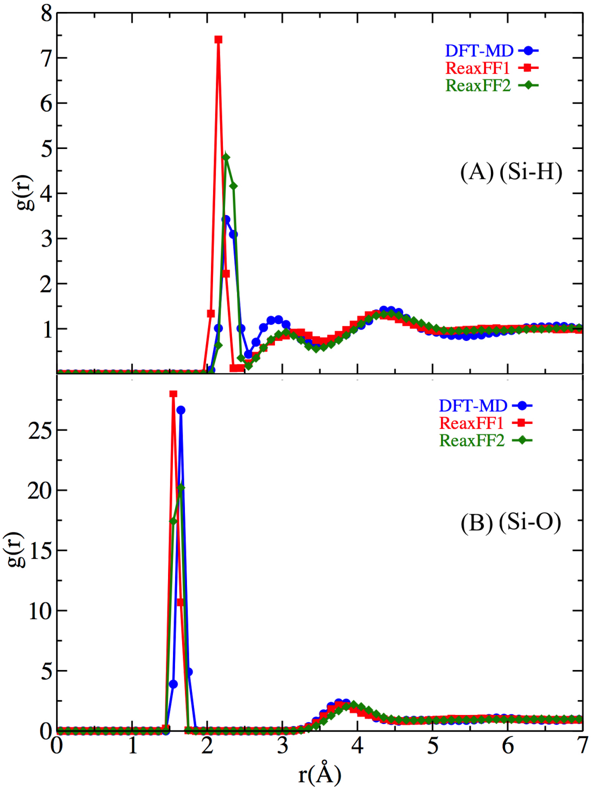

**Figure 3.8:** Radial distribution function for (A) silicon-hydrogen Si−H and (B) silicon-oxygen Si−O pair at T=350 K.

.

which can decrease the degree of hydrogen bonding with water molecules. Furthermore, the positive charge of $Na^+$ may reduce the $O^-$ and Si atom interaction prohibiting SiO−Si bond formation [63].

An important quantity for characterizing the chemical structures in liquid water is the radial distribution functions (RDF). In figure 3.7 and 3.8, we depict the shapes of RDF of (O−O), (H−H), (O−H), (Si−H) and (Si−O) obtained from 50 ps run after the equilibration step. The maximum values of the RDFs obtained from our simulations are in good agreement with Ref. 62. We have also used ReaxFF to investigate its capability to describe the thermodynamics and dynamics of the reaction. Figure 3.7 and 3.8 show that the internal structure of the solvent from ReaxFF simulations is similar to that of DFT based on the RDFs between oxygen and hydrogen. As shown in figure 3.9, we have

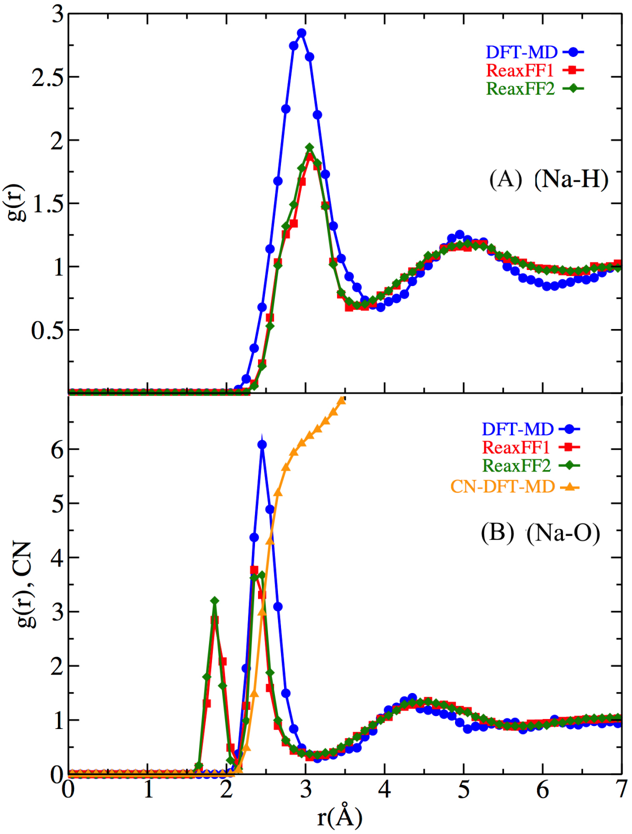

**Figure 3.9:** Radial distribution function for the Na−H, Na−O pair and the coordination number at T=350 K.

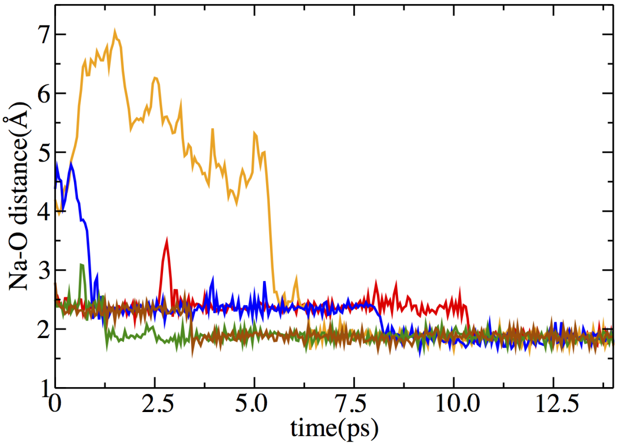

**Figure 3.10:** Time evolution of the H−O distance as function of time shows a spontaneous spurious reaction in aqueous solution of $Si(OH)_4$+$Si(OH)_3O^-$+$Na^+$+64$H_2O$s in a 13×13×13 $Å^3$ cubic box and at T=350 K.

investigated the solvation of sodium by calculating the RDF of (Na−O). In the DFT-MD simulation, the first peak in Na−O RDF is located between 2.1 and 3.1 Å and the second peak between 3.1 and 5.1 Å. The coordination number is 6.0. This results suggest that $Na^+$ is only slightly over-coordinated [72–74]. It might be due to the presence of silicate complex or effect of different functionals. However, this value is still close to the values a 5-6 most frequently reported through both experiments and other ab initio and classical MD studies of the $Na^+$ cation in bulk water [75–79].

Observing the water structure around the $Na^+$ ion, we find an unpredicted peak at 1.8 Å for the ReaxFF simulations. This peak is caused by a reaction forming sodium hydroxide in aqueous solution, a species that is stable only in the solid state. In fact, dissolution of solid sodium hydroxide in water forming $Na^+$ and $OH^-$ is a highly exothermic reaction. We repeated both ReaxFF1 and ReaxFF2 simulations using different initial configurations obtained from the DFT-simulation, but each time this spurious reaction occurred, except once.

In most ReaxFF cases, $H_2O$ dissociated to $OH^-$ and $H^+$. The proton transferred to $Si(OH)_3O^-$ to form $Si(OH)_4$ and the $Na^+$ and $OH^-$ ions formed NaOH. In another case, the released $OH^-$ reacted with $H_2O$ to give $H_3O_2{}^-$ which reacted further to form $H_3O_2Na$. Figure 3.10 shows the time evolution of the H−O distance as function of time for the oxygen that finally forms a bond with Na. Here we just reported the reactions that happened during the first 13 ps.

As shown in figure 3.10, the oxygen that finally forms a bond with $Na^+$ first approaches upto a distance of 2.42 Å. The oxygen is then still part of a water molecule in the first sodium solvation shell. Then, catalyzed by the silicate anion the water molecule splits into $H^+$ and $OH^-$ which the $OH^-$ quickly attaches to the sodium. It is interesting to note that these spurious reactions happened with both the ReaxFF parameters. We can conclude that, although the genetic algorithm was able to significantly improve the cost function [40] for ReaxFF2, it has not removed the unphysical artifacts of ReaxFF1 shown in our simulations. Therefore, the fitting procedure itself need to be reconsidered.

## 3.4 Conclusions

We have presented a comparison between DFT and ReaxFF calculations for the initial step of silicate dimerization reaction. The reactive force field was based on two different ReaxFF parameter sets. We based our analysis on two-way single point calculations along the reaction coordinate. In this approach, we optimized the geometry for constrained reaction coordinate values with one method and use the optimized geometries in single point calculations performed by the other two methods. The differences between the shifted energy curves (all starting at $E = 0$ at a reference distance) were substantial, and the differences in absolute energies (using $E = 0$ for the unconstrained optimized geometries) are even more pronounced. Then, we examined the consequences of these discrepancies in molecular dynamics simulations for the aqueous phase. Both ReaxFF force fields generated an unphysical formation of sodium hydroxide. This shows that despite a significant improvement regarding the global optimization algorithm to find the best possible force field parameter set, both force fields suffer from the same unphysical behavior. Therefore, it seems that the optimization algorithm is not sufficient in improving force field accuracy. The reference data set of configurations but also the cost function are essential. In specific, it is important that geometries are not only provided by quantum methods, it is also important that configurations provided by the reactive force field are energetically reasonable when analyzed by quantum mechanical calculations. Hence, a change in the force field fitting procedures is required to make reactive force field a reliable predictive tool. An interesting method to achieve this is the adaptive force field optimization in QuanTIS method [43]. This algorithm creates database of configurations while simulating chemical events and, in addition, compares these configurations from both sides; The energies of configuration points produced by a DFT-based MD simulation should be reproduced by the force field, and vice versa. The formation of sodium hydroxide would, directly be penalized since DFT energies will be much higher. The force field parameters will then, in the next optimization cycle, be changed such that this spurious reaction would not happen again. This might be an effective way to improve ReaxFF parameters, but it could also reveal that a completely new mathematical form is needed to achieve the required accuracy. Therefore, we hope that our results will encourage the development of a new generation reactive force fields which is essential to make computational tools a dominant factor regarding the discoveries of new materials or for making already existing materials in more energy-efficient or environmental-friendly way.

# Bibliography

[1] T. T. Trinh, A. P. J. Jansen, R. A. van Santen, and E. J. Meijer. Role of water in silica oligomerization. *J. Phys. Chem. C*, 113:2647–2652, 2009.

[2] J. C. G. Pereira, C. R. A. Catlow, and G. D. Price. Ab initio studies of silica-based clusters. part I. energies and conformations of simple clusters. *J. Phys. Chem. A*, 103:3252–3267, 1999.

[3] J. C. G. Pereira, C. R. A. Catlow, and G. D. Price. Ab initio studies of silica-based clusters. part II. structures and energies of complex clusters. *J. Phys. Chem. A*, 103:3268–3284, 1999.

[4] J. M. Fedeyko, D. G. Vlachos, and R. F. Lobo. Formation and structure of self-assembled silica nanoparticles in basic solutions of organic and inorganic cations. *Langmuir*, 21:5197–5206, 2005.

[5] S. A. Pelster, W. Schrader, and F. Schüth. Monitoring temporal evolution of silicate species during hydrolysis and condensation of silicates using mass spectrometry. *J. Am. Chem. Soc.*, 128:4310–4317, 2006.

[6] R. G. Parr and W. Yang. *Density Functional Theory of Atoms and Molecules*. Oxford University Press, New York, Oxford, 1989.

[7] J. C. G. Pereira, C. R. A. Catlow, and G. D. Price. Silica condensation reaction: An ab initio study. *Chem. Commun.*, 115:1387–1388, 1998.

[8] J. A. Tossell. Theoretical study on the dimerization of $Si(OH)_4$ in aqueous solution and its dependence on temperature and dielectric constant. *Geochim. Cosmochim. Acta*, 69:283–291, 2005.

[9] Y. T. Xiao and A. C. Lasaga. Ab initio quantum mechanical studies of the kinetics and mechanisms of quartz dissolution: OH-catalysis. *Geochim. Cosmochim. Acta*, 60:2283–2295, 1996.

[10] T. T. Trinh, A. P. J. Jansen, and R. A. Santen. Mechanism of oligomerization reactions of silica. *J. Phys. Chem. B*, 110:23099–23106, 2006.

[11] H. Hu, H. Hou, Z. He, and B. Wang. Theoretical characterizations of the mechanism for the dimerization of monosilicic acid in basic solution. *Phys. Chem. Chem. Phys.*, 15:15027–15032, 2013.

[12] R. Car and M. Parrinello. Unified approach for molecular dynamics and density-functional theory. *Phys. Rev. Lett.*, 55:2471–2474, 1985.

[13] D. E. Shaw, P. Maragakis, K. Lindorff-Larsen, S. Piana, R. O. Dror, M. P. Eastwood, J. A. Bank, J. M. Jumper, J. K. Salmon, Y. Shan, and W. Wriggers. Atomic-level characterization of the structural dynamics of proteins. *Science*, 330:341–346, 2010.

[14] R. O. Dror, T. J. Mildorf, D. Hilger, A. Manglik, D. W. Borhani, D. H. Arlow, A. Philippsen, N. Villanueva, Z. Yang, M. T. Lerch, W. L. Hubbell, B. K. Kobilka, R. K. Sunahara, and D. E. Shaw. Structural basis for nucleotide exchange in heterotrimeric g proteins. *Science*, 348:1361–1365, 2015.

[15] A. Warshel and R. M. Weiss. An empirical valence bond approach for comparing reactions in solution and in enzymes. *J. Am. Chem. Soc.*, 102:6218–6226, 1980.

[16] J. Åqvist and A. Warshel. Simulation of enzyme reactions using valence bond force fields and other hybrid quantum/classical approaches. *Chem. Rev.*, 93:2523–2544, 1993.

[17] J. Tersoff. New empirical model for the structural properties of silicon. *Phys. Rev. Lett.*, 56:632–635, 1986.

[18] D. W. Brenner. Empirical potential for hydrocarbons for use in simulating the chemical vapor deposition of diamond films. *Phys. Rev. B*, 42:9458–9471, 1990. Erratum in 46, 1948, 1992.

[19] D. W. Brenner, O. A. Shenderova, J. A. Harrison, S. J. Stuart, B. Ni, and S. B. Sinnott. A second-generation reactive empirical bond order (REBO) potential energy expression for hydrocarbons. *J. Phys.: Condens. Matter*, 14:783–802, 2002.

[20] D. G. Pettifor. New many-body potential for the bond order. *Phys. Rev. Lett.*, 63:2480–2483, 1989.

[21] E. Shustorovich. The bond-order conservation approach to chemisorption and heterogeneous catalysis: applications and implications. *Adv. Catal.*, 37:101–163, 1990.

[22] E. Shustorovich and H. Sellers. The UBI-QEP method: a practical theoretical approach to understanding chemistry on transition metal surfaces. *Surf. Sci. Rep.*, 31:1–119, 1998.

[23] F. H. Stillinger and T. A. Weber. Computer simulation of local order in condensed phases of silicon. *Phys. Rev. B*, 31:5262–5271, 1985. Erratum in 33, 1451, 1986.

[24] F. H. Stillinger and T. A. Weber. Fluorination of the dimerized Si(100) surface studied by molecular-dynamics simulation. *Phys. Rev. Lett.*, 62:2144–2147, 1989.

[25] D. Kohen, J. C. Tully, and F. H. Stillinger. Modeling the interaction of hydrogen with silicon surfaces. *Surf. Sci.*, 397:225–236, 1998.

[26] A. J. Dyson and P. V. Smith. Extension of the Brenner empirical interatomic potential to C-Si-H systems. *Surf. Sci.*, 355:140–150, 1996.

[27] A. J. Dyson and P. V. Smith. Empirical potential study of the chemisorption of $C_2H_2$ and $CH_3$ on the $\beta$-SiC(001) surface. *Surf. Sci.*, 396:24–39, 1998.

[28] D. Humbird and D. B. Graves. Improved interatomic potentials for silicon-fluorine and silicon-chlorine. *J. Chem. Phys.*, 120:2405–2412, 2004.

[29] A. C. T. van Duin, S. Dasgupta, F. Lorant, and W. A. Goddard. ReaxFF: A reactive force field for hydrocarbons. *J. Phys. Chem. A*, 105:9396–9409, 2001.

[30] A. K. Rappe and W. A. Goddard. Charge equilibration for molecular dynamic simulation. *J. Phys. Chem.*, 95:3358–3363, 1991.

[31] J. E. Mueller, A. C. T. van Duin, and W. A. Goddard. Development and validation of ReaxFF reactive force field for hydrocarbon chemistry catalyzed by nickel. *J. Phys. Chem. C*, 114:4939–4949, 2010.

[32] S. Agrawalla and A. C. T. van Duin. Development and application of a ReaxFF reactive force field for hydrogen combustion. *J. Phys. Chem. A*, 115:960–972, 2011.

[33] X. M. Cheng, Q. D. Wang, J. Q. Li, J. B. Wang, and X. Y. Li. ReaxFF molecular dynamics simulations of oxidation of toluene at high temperatures. *J. Phys. Chem. A*, 116:9811–9818, 2012.

[34] M. Raju, S. Y. Kim, A. C. T. van Duin, and K. A. Fichthorn. ReaxFF reactive force field study of the dissociation of water on titania surfaces. *J. Phys. Chem. C*, 117:10558–10572, 2013.

[35] A. Ostadhossein, E. D. Cubuk, G. A. Tritsaris, E. Kaxiras, S. Zhang, and A. C. T. van Duin. Stress effects on the initial lithiation of crystalline silicon nanowires: Reactive molecular dynamics simulations using ReaxFF. *Phys. Chem. Chem. Phys.*, 17:3832–3840, 2015.

[36] A. C. T. van Duin. *ReaxFF User Manual*. Materials and Process Simulation Center, 2002.

[37] A. C. T. van Duin, A. Strachan, S. Stewman, Q. Zhang, X. Xu, and W. A Goddard. ReaxFF$_{SiO}$ reactive force field for silicon and silicon oxide systems. *J. Phys. Chem. A*, 107:3803–3811, 2003.

[38] S. Dumpala, S. R. Broderick, U. Khalilov, E. C. Neyts, A. C. T. van Duin, J. Provine, R. T. Howe, and K. Rajan. Integrated atomistic chemical imaging and reactive force field molecular dynamic simulations on silicon oxidation. *Appl. Phys. Lett.*, 106:011602–5, 2015.

[39] J. C. Fogarty, H. M. Aktulga, A. Y. Grama, A. C. T. Van Duin, and S. A Pandit. A reactive molecular dynamics simulation of the silica-water interface. *J. Chem. Phys.*, 132:174704–174710, 2010.

[40] H. R. Larsson, A. C. T. van Duin, and B. Hartke. Global optimization of parameters in the reactive force field ReaxFF for SiOH. *J. Comput. Chem.*, 34:2178–2189, 2013.

[41] T. Verstraelen, P. Bultinck, V. Van Speybroeck, P. W. Ayers, D. Van Neck, and M. Waroquier. The significance of parameters in charge equilibration methods. *J. Chem. Theory Comput.*, 7:1750–1764, 2011.

[42] H. Li and W. Yang. Sampling enhancement for the quantum mechanical potential based molecular dynamics simulations: A general algorithm and its extension for free energy calculation on rugged energy surface. *J. Chem. Phys.*, 126:114104–114107, 2007.

[43] A. Lervik and T. S. van Erp. Gluing potential energy surfaces with rare event simulations. *J. Chem. Theory Comput.*, 11:2440–2450, 2015.

[44] G. te Velde, F. M. Bickelhaupt, E. J. Baerends, C. Fonseca Guerra, S. J. A. van Gisbergen, J. G. Snijders, and T. Ziegler. Chemistry with ADF. *J. Comput. Chem.*, 22:931–967, 2001.

[45] A. D. Becke. Density-functional exchange-energy approximation with correct asymptotic behavior. *Phys. Rev. A*, 38:3098–3100, 1988.

[46] C. Lee, W. Yang, and R. G. Parr. Development of the Colle-Salvetti correlation-energy formula into a functional of the electron density. *Phys. Rev. B*, 37:785–789, 1988.

[47] J. Andzelm J. Baker, M. Muir and A. Scheiner. Hybrid Hartree-Fock density-functional theory functionals: The adiabatic connection method. *ACS Symposium Series*, 629:342–367, 1996.

[48] S. Grimme, S. Ehrlich, and L. Goerigk. Effect of the damping function in dispersion corrected density functional theory. *J. Comput. Chem.*, 32:1456–1465, 2011.

[49] E. van Lenthe and E. J. Baerends. Optimized Slater-type basis sets for the elements 1-118. *J. Comput. Chem.*, 9:1142–1156, 2003.

[50] D. P. Chong. Augmenting basis set for time-dependent density functional theory calculation of excitation energies: Slater-type orbitals for hydrogen to krypton. *Mol. Phys.*, 103:749–761, 2005.

[51] D. P. Chong, E. van Lenthe, S. J. A. van Gisbergen, and E. Jan Baerends. Even-tempered Slater-type orbitals revisited:from hydrogen to krypton. *J. Comput. Chem.*, 25:1030–1036, 2003.

[52] G. Maroulis. *Computational Aspects of Electric Polarizability Calculations: Atoms, Molecules and Clusters*. IOS Press, Amsterdam, 2006.

[53] M. Güell, J. M. Luis, M. Solà, and M. Swart. Importance of the basis set for the spin-state energetics of iron complexes. *J. Phys. Chem. A*, 112:6384–6391, 2008.

[54] J. VandeVondele, M. Krack, F. Mohamed, M. Parrinello, T. Chassaing, and J. Hutter. Quickstep: Fast and accurate density functional calculations using a mixed Gaussian and plane waves approach. *Comput. Phys. Commun.*, 167:103–128, 2005.

[55] CP2K: High Performance Computing, http://www.nanosim.mat.ethz.ch/research/cp2k.

[56] S. Goedecker, M. Teter, and J. Hutter. Separable dual-space Gaussian pseudopotentials. *Phys. Rev. B*, 54:1703–1710, 1996.

[57] C. Hartwigsen, S. Goedecker, and J. Hutter. Relativistic separable dual-space Gaussian pseudopotentials from H to Rn. *Phys. Rev. B*, 58:3641–3662, 1998.

[58] S. Grimme. Semiempirical GGA-type density functional constructed with a long-range dispersion correction. *J. Comput. Chem.*, 27:1787–1799, 2006.

[59] J. VandeVondele and J. Hutter. Gaussian basis sets for accurate calculations on molecular systems in gas and condensed phases. *J. Chem. Phys.*, 127:114105–114105, 2007.

[60] T. T. Trinh, A. P. J. Jansen, R. A. van Santen, and E. Jan Meijer. The role of water in silicate oligomerization reaction. *Phys. Chem. Chem. Phys.*, 11:5092–5099, 2009.

[61] S. Nosé. A unified formulation of the constant temperature molecular dynamics methods. *J. Chem. Phys.*, 81:511–519, 1984.

[62] E. Carter, G. Ciccoti, and J. T. Hynes. Constrained reaction coordinate dynamics for the simulation of rare events. *Chem. Phys. Lett.*, 156:472–477, 1989.

[63] A. Pavlova, T. T. Trinh, R. A. van Santen, and E. J. Meijer. Clarifying the role of sodium in the silica oligomerization reaction. *Phys. Chem. Chem. Phys.*, 15:1123–1129, 2013.

[64] H. J. C. Berendsen, J. P. M. Postma, W. F. van Gunsteren, A. DiNola, and J. R. Haak. Molecular dynamics with coupling to external bath. *J. Chem. Phys.*, 81:3684–3690, 1984.

[65] D. Frenkel and B. Smit. *Understanding Molecular Simulation, Second Edition: From Algorithms to Applications*. Academic Press, San Diego, CA, 2005.

[66] G. J. Martyna, M. L. Klein, and M. Tuckerman. Nosé-hoover chains: The canonical ensemble via continuous dynamics. *J. Chem. Phys.*, 97:2635–2643, 1992.

[67] K. Chenoweth, A. C. T. van Duin, and W. A. Goddard. ReaxFF reactive force field for molecular dynamics simulations of hydrocarbon oxidation. *J. Phys. Chem. A*, 112:1040–1053, 2008.

[68] T. T. Trinh, A. P. Jansen, R. A. van Santen, J. VandeVondele, and E. J. Meijer. Effect of counter ions on the silica oligomerization reaction. *Comput. Phys. Commun.*, 10:1775–1782, 2009.

[69] Y. T. Xiao and A. C. Lasaga. Ab initio quantum mechanical studies of the kinetics and mechanisms of silicate dissolution: $H^+$ ($H_3O^+$) catalysis. *Geochim. Cosmochim. Acta*, 58:5379–5400, 1994.

[70] C. C. Harrison and N. Loton. Novel routes to designer silicas: studies of the decomposition of $(M^+)_2[Si(C_6\ H_4O_2)_3].xH_2O$. importance of $M^+$ identity of the kinetics of oligomerisation and the structural characteristics of the silicas produced. *J. Chem. Soc., Faraday Trans.*, 91:4287–4297, 1995.

[71] S. L. Burkett and M. E. Davis. Mechanism of structure direction in the synthesis of pure-silica zeolites. 2. hydrophobic hydration and structural specificity. *Chem. Mater.*, 7:1453–1463, 1995.

[72] A. Grossfield, P. Ren, and J. W. Ponder. Ion solvation thermodynamics from simulation with a polarizable force field. *J. Am. Chem. Soc.*, 125:15671–15682, 2003.

[73] D. Bucher, L. Guidoni, P. Carloni, and U. Rothlisberger. Coordination numbers of $K^+$ and $Na^+$ ions inside the selectivity filter of the KcsA potassium channel: Insights from first principles molecular dynamics. *Biophys. J.*, 98:L47–L49, 2010.

[74] C. N. Rowley and B. Roux. The solvation structure of $Na^+$ and $K^+$ in liquid water determined from high level ab initio molecular dynamics simulations. *J. Chem. Theory Comput.*, 8:3526–3535, 2012.

[75] S. B. Zhu and G. W. Robinson. Molecular dynamics computer simulation of an aqueous NaCl solution: Structure. *J. Chem. Phys.*, 97:4336–4348, 1992.

[76] D. A. Schmidt and K. Miki. Defective continuous hydrogen-bond networks: An alternative interpretation of ir spectroscopy. *Comput. Phys. Commun.*, 9:1914–1919, 2008.

[77] N. T. Skipper and G. W. Neilson. X-ray and neutron diffraction studies on concentrated aqueous solutions of sodium nitrate and silver nitrate. *J. Phys.: Condens. Matter*, 1:4141–4154, 1989.

[78] R. Mancinelli, A. Botti, F. Bruni, M. A. Ricci, and A. K. Soper. Hydration of sodium, potassium, and chloride ions in solution and the concept of structure maker/breaker. *J. Phys. Chem. B*, 111:13570–13577, 2007.

[79] A. Tongraar, K. R. Liedl, and B. M. Rode. Born-Oppenheimer ab initio QM/MM dynamics simulations of $Na^+$ and $K^+$ in water: From structure making to structure breaking effects. *J. Phys. Chem. A*, 102:10340–10347, 1998.

# Chapter 4

# Rare Event Ab Initio Simulations Reveal Subtle Key Steps in Aqueous Silicate Dimerization

Mahmoud Moqadam, Enrico Riccardi, Thuat Trinh, Anders Lervik,
Titus S. van Erp

Manuscript

**Abstract -** A replica exchange transition interface sampling (RETIS) study combined with Born-Oppenheimer molecular dynamics (BOMD) is used to investigate the dynamics, thermodynamics and mechanism of the early stages of the silicate condensation process. In this process, two silicate monomers, of which one anion species, form a negatively charged five-coordinated silicate dimer. In a second stage, this dimer can fall apart again, forming the original monomers, or release a water molecule into the solution. We studied the association and dissociation reaction in the gas phase, and the dissociation and water removal step in the aqueous phase. The results on the aqueous phase dissociation suggest two possible mechanisms. The breakage of the bond between the intermediate oxygen and the five-coordinated silicon is sometimes accompanied with a proton transfer. After the dissociation into silicate monomers, the anionic monomer is either the previously four-coordinated silicon or the previously five-coordinated silicon depending on whether the hydrogen transfer occurs or not. Our results show that the mechanism with proton transfer is highly predominant. The water removal simulations also show two possible mechanisms distinguished by the proton transfer reaction path. The proton transfer can either occur via a direct or via a water mediated reaction step. The calculations reveal that although both mechanisms contribute to the water removal process, the direct proton transfer is slightly favorable and occurs roughly in six out of ten occasions.

## 4.1 Introduction

The silicate condensation reaction is the basic step in the sol-gel chemistry and zeolite synthesis. Therefore, understanding the earlier stages of silicate oligomerization is of fundamental scientific and technological importance. The formation of the silicate dimer from two silicate monomers, a neutral and an anionic species, basically consists of two steps. The first step in this process is formation of the SiO$-$Si linkage between the reactants to form a five-coordinated silicate complex. This is an essential intermediate stage in the oligomerization reaction. In the second step, a water molecule is released from the silicate complex forming the silicate dimer (see figure 4.1). The mechanism of silicate based reactions have been subject of intensive research during last decades, both experimentally [1–5] and theoretically [6–16].

Several of the previous theoretical studies have concentrated on the energetics of cluster models either based on Hartree-Fock [11, 14, 15, 17, 18], MP2 [11, 14, 15, 18], or density functional theory (DFT) [6–8, 10, 13, 19–22] in which the clusters are either described in the gas phase or in a solvent using continuum solvent models. In particular, Pereira et al. [6–8] studied the silicate clusters using DFT coupled with the continuum solvation model COSMO (Conductor-like Screening MO method) to mimic the electrostatic conditions found in real silica solutions. Similarly, Xiao and Lasaga addressed the catalytic effect of $OH^-$ in promoting the dissolution process in basic pH solutions [18]. The limited size of the silicate clusters allowed relatively high-level quantum chemical computations. In addition to energy barriers, reaction rates can be approximated using transition state theory [11, 14]. However, these barriers and rates are not necessarily representable for the actual reactions in a solvent. Especially for water it is known that the solvent actively directs chemical reactions via its hydrogen bond network or participates in the reaction by accepting or donating protons.

The thermodynamic properties of silicate oligomerization process in explicit water have also been studied using Ab Initio molecular dynamics [10, 13, 16]. Since the accessible timescale of Ab Initio molecular dynamics is on the order of several picoseconds while the expectation time for a chemical reaction is many orders of magnitude larger, straightforward Ab Initio molecular dynamics is generally not useful to study chemical reactions. Still, thermodynamic quantities like the reaction free energy barriers and equilibrium constants can be obtained using standard constrained molecular dynamics methods and

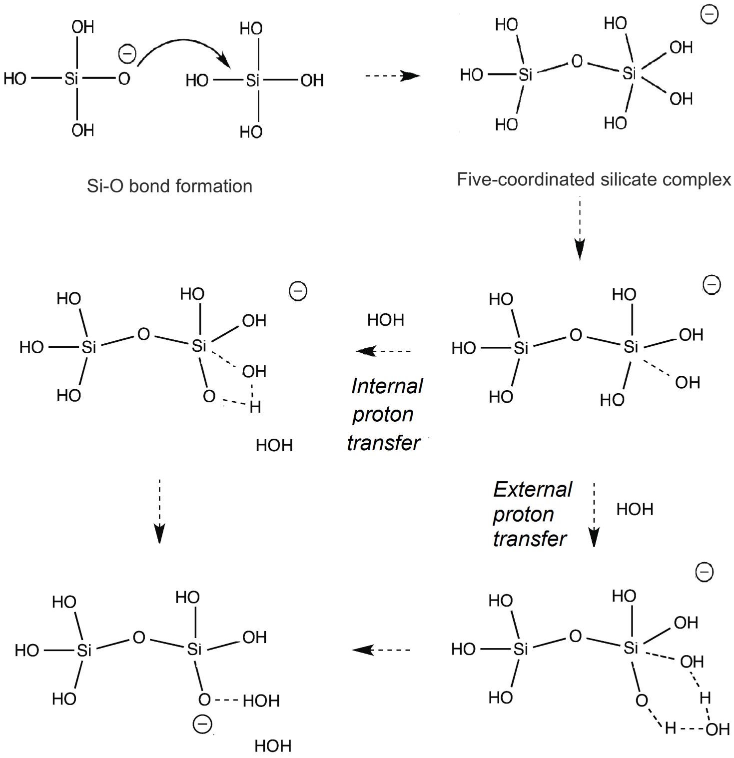

**Figure 4.1:** The anionic mechanism of the silicate condensation reactions. The first step is formation of a five-coordinated silicate complex. Then, a water molecule dissociates from silicate complex either by an internal or external proton transfer and forms the silicate dimer.

thermodynamic integration [10, 13, 16, 20–22].

Thermodynamic integration via constraint molecular dynamics [23] implies running several molecular dynamics simulations in which a predefined reaction coordinate (RC) is kept fixed by an artificial constraining force. Although it allows obtaining thermodynamic properties, information on the spontaneous dynamics is lost. An alternative approach is the use of classical molecular dynamics simulations based on reactive forcefields [24–31]. At this point, reactive force fields do not reach the same accuracy as DFT and might not always reliable [16], but the accessible timescale of molecular dynamics with reactive forcefields is in the range of several nanoseconds. Therefore, it is able to capture the spontaneous reactive events in a wide range of chemical systems. Still, these studies often require temperatures far above experimental conditions to increase the frequency of reactive events.

Even faster than classical molecular dynamics is kinetic Monte Carlo (kMC) [32] which has been applied to investigate silicate oligomerization reactions [33–35]. The kinetic Monte Carlo typically requires as an input the diffusion constants of the reactants and rate constants of several elementary reaction steps. Zhang et al. developed a continuum off-lattice kMC model for the initial stage of silicate oligomerization based on rate constants from transition state theory from DFT calculations with explicit water molecules [34]. This method allows exploring initial stage of silicate oligomerization and the effect of pH at experimental conditions. More recently, a lattice-based kinetic Monte Carlo model was introduced by Ciantar et al. [35] to study the effect of molecular diffusion, synthesis parameters and initial monomer concentration on the steady state concentrations of silicate oligomers at the earlier stages of zeolite synthesis. This model allows automatic allocation of each species with a flexible use of various lattice types. The accessible timescale of kinetic Monte Carlo is enormous (minutes, hours) but its accuracy highly depends on the accuracy of the rate constants of the elementary steps which need to be provided as an input. In addition, detailed information about the actual reaction mechanism is lost.

Clearly, the above review shows that the computational study of the actual unbiased dynamics of the oligomerization process is still a huge challenge. Ideally, we would like to use accurate forces based on Ab Initio methods and still reach large timescales. Kinetic Monte Carlo has limited accuracy as mentioned above. ReaxFF increases the timescale compared to Ab Initio based molecular dynamics, but generally not enough to study the reactions at ambient condition. In addition, it requires choosing a parameter set or developing a new purpose-specific parameter set since we showed that simulations based on present ReaxFF forcefields [36, 37] can produce unphysical reactions [16].

An alternative approach which can be used in combination with any type of molecular dynamics is path sampling [38–40]. Path sampling allows the harvesting of statistically relevant ensembles of unbiased dynamical trajectories based on a combined

Monte Carlo/molecular dynamics approach. Based on the ensemble conditions, these sets of paths will describe different stages of the reaction process. For instance, one ensemble condition could be that all path should start from the reactant state and end in the product state. Hence, this path ensemble only consists of reactive paths. Other path ensembles might only require the paths to reach a certain threshold point at the barrier. Path sampling allows overcoming high free energy barriers without artificially constraining the system or by applying an additional biasing force. Hence, it will provide the real dynamics of the process and, by combining the results of the different path ensembles, it can provide rate constants orders of magnitude faster than straightforward molecular dynamics. The efficiency of the original transition path sampling method [38] was consecutively improved by the TIS [39] and RETIS [40] algorithms and has now matured as a powerful method to study unbiased reactive events. In this chapter, we will use RETIS in combination with Ab Initio molecular dynamics, which has not been used before, in order to shed light on yet unresolved questions regarding the spontaneous oligomeriztion process.

For example, Pavlova et al. [13] reported that the water removal step of silicate dimerization and trimerization reaction occurs through the external proton transfer mechanism, while Trinh et al. [10] denoted that in the dimerization reaction only the internal proton transfer mechanism occurs. In some cases, they observed the external proton transfer mechanism in the trimerization reaction. In contrast, McIntosh detected both internal and external mechanisms in the silicate dimerization reactions [11]. However, the author concluded that internal mechanism is highly favorable compared to the external mechanism. Based on the available literature it is difficult to state a final conclusion since the aforementioned studies all depend on different level of assumptions and approximations or steer the reaction in an artificial manner. RETIS with Ab Initio molecular dynamics is, therefore, a very valuable complementary method to the studies above as it is the only method that can provide the correct statistics of unbiased dynamical reactive trajectories in explicit water based on state-of-the-art DFT level energies and forces.

Path sampling with Ab Initio molecular dynamics has been used before for the study of water autoionization [41], fenton reactions [42], gas-phase decomposition reactions [43], and enzyme catalysis [44]. However, these papers are based on the original TPS [38] algorithm employing a single path ensemble of reactive trajectories. This study is the first one where the RETIS methodology is applied in combination with Ab Initio dynamics using many different path ensembles. Hence, it is the first really quantitative Ab Initio path sampling study which allows the calculation of rates, crossing probabilities, and activation energies.

This chapter is organized as follows. In Section 4.2 we give an explanation of the RETIS methodology used in the work. In Section 4.3 we give the computational details for our approach. In Section 4.4 we provide the results accompanied with discussion for the gas-phase dissociation and association reaction, and the aqueous phase dissociation and water removal step. We end with concluding remarks in Section 4.5.

## 4.2 Methodology

The typical reaction times of the chemical reaction steps in the dimerization process are generally beyond the accessible timescale of molecular dynamics. Hence, it is extremely unlikely to detect any of such rare events in a direct simulation. Still, these events can be captured via the RETIS algorithm [40], which can be combined with any type of dynamics such as classical MD, Langevin, or Ab Initio MD. Whereas the first Ab Initio MD simulations were based on the Car-Parrinello approach [45], which launched the sudden popularity of these type of simulations, the advance in speed of electronic ground-state optimization algorithms have made BOMD the method of choice for Ab Initio MD. In this chapter, the RETIS algorithm has been combined with the BOMD utility of the CP2K [46] Quickstep routine.

RETIS is a path sampling method based on transition path sampling techniques (TPS) [38] allowing for an efficient quantitative analysis of chemical reaction and rare events in general. TPS has pioneered the idea to use Monte Carlo (MC) to sample short molecular dynamics reactive trajectories. In this way, the approach allows us to focus on those segments of the time evolution where the rare events actually occur. The original TPS publication [38] also provided a strategy to use this approach for calculating rate constants though not in the most efficient way. The TIS algorithm [39] improved the efficiency by a factor five for a simple two-state dimer molecule imersed in a solvent by allowing flexible path lengths and the introduction of interface path ensemble averages. The efficiency was further improved in the RETIS algorithm [40] by applying replica exchange between the different path ensembles. This approach showed a factor 20 improvement compared to TIS when studying the denaturation of a mesoscopic DNA model [47]. Although it is difficult to make a statement about the relative algorithmic efficiency in general, one can prove that the efficiency always increases when going from the original TPS algorithm to TIS and from TIS to RETIS. Based on the numbers above, the RETIS approach can easily account for a two orders of magnitude overall improvement compared to the original TPS algorithm. It is important to note that is improvement is achieved without invoking any approximation. On the contrary, the TIS/RETIS approach is also slightly more accurate since they are not restricted to a fixed path length; the average path length in TIS/RETIS is reduced compared to TPS but occasionally longer than the typical fixed path length used in TPS simulations.

The TIS/RETIS algorithm introduces a set of interfaces between the reactant and the product state and computes the overall crossing probability as a product of crossing probabilities for the intermediate interfaces. The TIS equations for transition between two stable states are:

$$k_{AB} \quad = \quad f_A \mathcal{P}_A(\lambda_B|\lambda_A) \tag{4.1}$$

$$\mathcal{P}_A(\lambda_B|\lambda_A) \quad = \quad \mathcal{P}_A(\lambda_n|\lambda_0) = \prod_{i=0}^{n-1} \mathcal{P}_A(\lambda_{i+1}|\lambda_i) \tag{4.2}$$

where $f_A$ is the flux through the first interface $\lambda_0$. The flux term is determined in the RETIS algorithm from the average path lengths in the first two path ensembles, called $[0^-]$ and $[0^+]$ [40]. These path ensembles have as only condition that they should start at the first interface $\lambda_0 = \lambda_A$ and from there move towards the reactant state ($[0^-]$) or towards the product state ($[0^+]$). These paths are ended when they recross $\lambda_A$ or $\lambda_B = \lambda_n$. The latter is only possible for the $[0^+]$ ensemble, but unlikely since it is a rare event. The chance that this happens is equal to $\mathcal{P}_A(\lambda_B|\lambda_A)$ which is called the overall crossing probability. This is the probability that whenever the system crosses $\lambda_A$, it will cross $\lambda_B$ before it crosses $\lambda_A$ again. As $\lambda_B$ is positioned a surface at the other side of the barrier, this probability is very small and can not be calculated directly. However, in TIS/RETIS it is determined by a series of path sampling simulations using the factorization given in equation (4.2). Here, $\mathcal{P}_A(\lambda_{i+1}|\lambda_i)$ is the conditional crossing probability that $\lambda_{i+1}$ will be crossed before $\lambda_A$ under the condition that the trajectory starting from $\lambda_A$ has also crossed $\lambda_i$. Determination of this term requires the sampling of the $[i^+]$ path ensemble which contain all possible trajectories starting at $\lambda_A$, ending at $\lambda_A$ or $\lambda_B$, and having at least one crossing with interface $\lambda_i$ in between. This sampling can be done efficiently via MC moves in trajectory space such as shooting and time-reversal moves, which were developed within the TPS framework [48]. In RETIS this is completed with replica exchange moves. $\mathcal{P}_A(\lambda_{i+1}|\lambda_i)$ is finally estimated from the fraction of trajectories in the $[i^+]$ ensemble that cross $\lambda_{i+1}$ as well. It should be noted that the overall reaction rate does not depend on the positions or the number of the interfaces, however, efficiency does. If the crossing probabilities are all around 0.2 the simulation set up is considered to be close to optimum [49].

As reaction coordinate we chose the Si$-$O distance of the bond that will be created or broken in the dissociation and association reaction. In the water removal step, the reaction coordinate is MAX[Si$-$OH] which implies that the value of the reaction coordinate corresponds to the largest Si$-$OH distance in the five-coordinated silicon. This approach guarantees that the leaving OH group can be any Si$-$OH bond of the five-coordinated silicon (see figure 4.2).

Besides reaction rates, path sampling also allows determining the activation energy of the reaction [50]. In the case of deterministic dynamics, the activation energy is equivalent to the difference between the average energy of state $A$ and the average energy

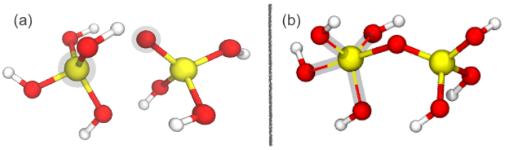

**Figure 4.2:** Illustration of the reaction coordinate used in the RETIS simulation. Highlighted atoms and bonds show the atoms and bonds related to the reaction coordinate. (a) Formation and dissociation of silicate complex. The reaction coordinate is defines as Si−O distance, the distance between the five-coordinated silicon and the bridging or the anion oxygen. (b) Water removal step. The reaction coordinate is MAX[Si−OH] which is the maximum distance between oxygen and the five-coordinated silicon.

of the transition pathways connecting state $A$ with state $B$ [50]. Consequently, the calculation of activation energy barrier does not require all interface ensembles. However, if all the path ensembles are available, like in a TIS or RETIS simulation, an activation energy profile as function of the reaction coordinate can be obtained [49]. Analogous to the crossing probability, the function converges to a plateau value equal to the activation energy of the reaction. The function is expected to be strictly increasing, but not necessarily. Dips or sudden changes in slope of the activation energy function might indicate a complex reaction step at the value of the reaction coordinate where it happens. The total energy of the system is an extensive variable. Hence, it increases if, for instance, more solvent molecules are added to the system. However, the activation energy is an intensive variable. This implies that for large systems this activation energy is a relative small energy difference between two ensemble average which have much larger standard deviation than this difference. Therefore, accurate evaluation of the activation energy becomes problematic for the larger systems.

## 4.3 Computational Details

We studied the formation of five-coordinated silicate complex from one silicic acid $Si(OH)_4$ and its deprotonated form $Si(OH)_3O^-$ in gas and aqueous phase by coupling the RETIS algorithm with the DFT-based molecular dynamics simulation package Quickstep of the CP2K code [46, 51]. The CP2K part of the simulation scheme employed the BLYP functional with Grimme's empirical dispersion correction [52–55] and Goedecker-Teter-Hutter (GTH) pseudopotentials [56, 57]. The BLYP functional has shown to give an accurate description of the structure and dynamics of water [10, 16, 58]. A Gaussian basis set DZVP-MOLOPT [59] was chosen in addition to a plane-wave basis set with a cutoff of cutoff 400 Ry. In the gas phase, the simulations were performed using a cubic simulation box of $13\times13\times13$ Å$^3$ with periodic boundaries containing $Si(OH)_4$ and its deprotonated form $Si(OH)_3O^-$. In the aqueous phase, it also includes a $Na^+$ ion and 64 water molecules. All simulations were performed at a temperature of 350 K with a time step of 0.5 fs.

In the RETIS part, we employed 10 and 15 interfaces for the dissociation and association of silicate complex in the gas phase, and 7 and 15 interfaces for the dissociation of silicate complex and water removal step in aqueous phase, respectively. We used previously computed free energy profiles [16] as a guideline to identify suitable positions of the interfaces. Additionally we used some initial trial simulations to adjust the number of interfaces and their positions. For the water removal step the reaction coordinate is based on the distance between the five-coordinated silicon and hydroxyl oxygen that is released. The first interface, defining the reactant state $A$, was set at $\lambda_A = 1.85$ Å and the last interface, defining product state $B$, was set at $\lambda_B = 3.8$ Å. For the cases in which $\lambda_B$ was crossed without the second reaction step being completed, we used the last configuration and atomistic velocities to start a straightforward molecular trajectory. All of these trajectories showed that the second reaction step followed eventually and none of these trajectories showed the reverse reaction. This implies that crossing $\lambda_B$ is a valid criterion to assume that basin of attraction of the product state is reached.

At each cycle and each path ensemble, we randomly choose among the different MC moves to be carried out. These are shooting, time-reversal, and replica exchange moves. The selection probability for these moves are equal to 25%, 50%, and 25%, respectively. In total, at least 5000 cycles were performed for the dissociation reaction and 2000 cycles for the association reaction in the gas phase. Each cycle implies an update of each path ensemble with a single Monte Carlo move. In the aqueous phase, we also performed at least 2200 cycles for the dissociation reaction in the aqueous phase and 2500 cycles for the water removal step.

## 4.4 Results and Disscusion

For the gas phase we focused on the association and dissociation mechanism, since the water removal step is of little physical relevance in the gas phase. The surrounding hydrogen-bonded network of the aqueous solution is essential element to facilitate the departure of the hydroxyl group. For the aqueous phase, we focused on the dissociation and the water removal step since the height of the association barrier proved to require too much computational resources.

### 4.4.1 Gas Phase

**Dissociation and association.** Here we analyze the first step of this reaction in a small-scale gaseous system in both forward (association) and backward (dissociation). For this purpose, several reactive trajectories along the reaction coordinate were used to investigate the reaction mechanism in the gas phase. Analysis of the reactive molecular dynamics trajectories showed that the dissociation and association reactions occur by the direct mechanism, in which the Si$-$O bond is dissociated or created without significant disturbance of any of the other molecular bonds (see figure 4.3). Figure 4.3 shows that the

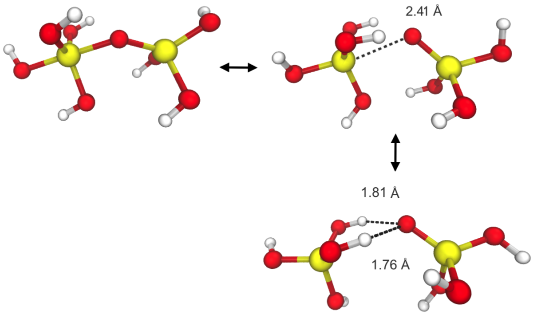

**Figure 4.3:** Representative snapshots of dissociation of silicate complex in gas phase. Distances of Si−O and hydrogen bonds are shown in angstrom (Å)

**Table 4.1:** The flux $f_A$ through $\lambda_A$, crossing probability $P(\lambda_B|\lambda_A)$, and rate constant k$_{AB}$ for the silicate complex dissociation (Dissoc.), association (Assoc.), and water removal step (Remov.) at 350 K. Results are shown for (a) gas-phase and (b) aqueous phase.

| (a) Gas | $f_A$ ($s^{-1}$) | $P(\lambda_B\|\lambda_A)$ | k$_{AB}$ ($s^{-1}$) |
|---|---|---|---|
| Dissoc. | $6.20\times10^{12}$ | $1.24\times10^{-2}$ | $7.68\times10^{10}$ |
| Assoc. | $2.23\times10^{12}$ | $7.13\times10^{-8}$ | $1.59\times10^{5}$ |
| **(b) Aqueous** | $f_A$ ($s^{-1}$) | $P(\lambda_B\|\lambda_A)$ | k$_{AB}$ ($s^{-1}$) |
| Dissoc. | $6.87\times10^{12}$ | $6.92\times10^{-5}$ | $4.75\times10^{8}$ |
| Remov. | $8.04\times10^{12}$ | $2.53\times10^{-6}$ | $2.04\times10^{7}$ |

silicon atoms and the intermediate oxygen are not exactly aligned, the Si-O-Si angle has a small bend, tilting the oxygen a little upwards (Figure 4.3). In the dissociation process, the upper hydroxyl groups of the four-coordinated silicate group flip their orientation and make hydrogen bonds with the intermediate oxygen. This process is highly symmetric with both hydroxyl groups forming the hydrogen bonds almost simultaneously. However, this process does not lead to a transfer of the proton of any of the hydroxyl groups towards the intermediate oxygen.

Table 4.1a shows the flux through interface $\lambda_A = 1.95$ Å for dissociation and $\lambda_A = 3.1$ Å for association, the overall crossing probability, and the rate constants which follows as the product of the two for the dissociation and association reactions in gas phase. The rate constant for dissociation is five orders of magnitude higher than the one of the association process. Block analysis indicates statistical errors of 15% and 66% for dissociation and association, respectively.

Figure 4.4a,b shows the activation energy profiles and the crossing probabilities for association and dissociation calculated from the RETIS path ensembles. The activation

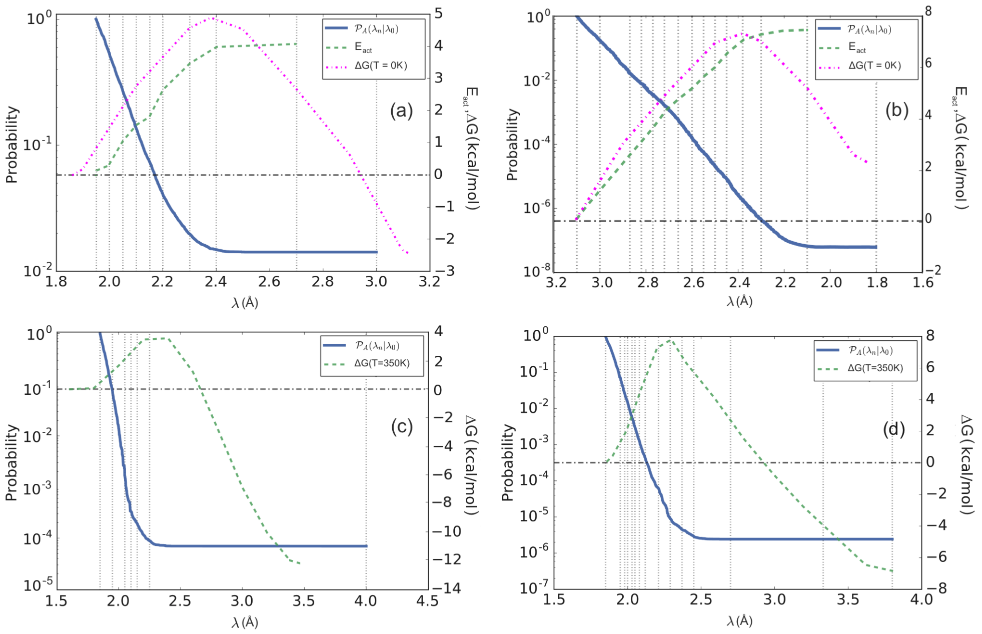

**Figure 4.4:** Crossing probabilities as function of RC for the silicate dimerization at 350 K. The positions of the interfaces are indicated with vertical dashed lines. (a) Dissociation reaction of silicate complex, (b) Association reaction of silicate complex in gas phase. The DFT free energy profile was calculated at 0 K using the BLYP functional including Grimme dispersion correction [60] and the QZ4P [61] basis set [16]. (c) Dissociation reaction of silicate complex in aqueous phase. The free energy profile was calculated from constrained molecular dynamics simulation using the BLYP functional and the DZVP-MOLOPT basis set [16]. (d) Water removal step, free energy profile obtained from Ref. 13.

energy profile clearly converges to a plateau analogous to the crossing probability. In both panels a, b of Figure 4.4 we showed the minimized energy previously obtained [16] using DFT geometry optimizations in which the Si-O distance was held fixed at different values ranging from 1.83 til 3.15 Å. This curve corresponds to the so-called zero temperature free energy curve and shows a transition state at 2.38 Å [16], just before the point were the activation energy curve and the crossing probability starts to become flat. The mismatch in position between the maximum of energy curve obtained from the constrained geometry optimization and the plateau value of the activation energy obtained from RETIS simulation is due to hysteresis [62] caused by the reaction coordinate not being aligned with the eigenvector with negative eigenvalue. The zero temperature free energy barrier for both association and dissociation is close (within 1 kcal/mol) but not identical, which is also logical since they describe related but conceptual different quantities. In our simulations, length of the reactive trajectories ranges between 100 and 400 fs for the dissociation and between 150 and 650 fs for the association process in gas phase.

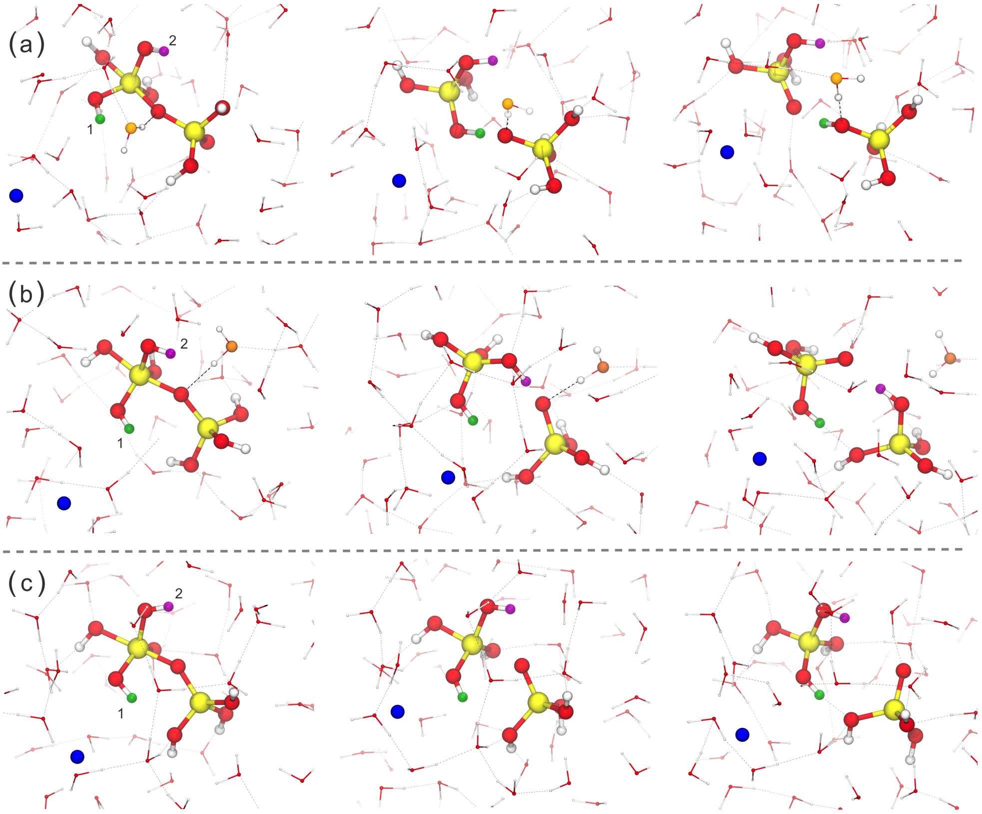

**Figure 4.5:** Representative snapshots of different dissociation mechanism of silicate complex in aqueous phase. Hydrogens with possibility of involving in the dissociation process are shown in green and purple colors. Water molecule with hydrogen bond to the bridging oxygen is shown in orange and $Na^+$ ion is colored in blue. (a), (b) Mechanism with hydrogen transfer (c) Mechanism without hydrogen transfer.

### 4.4.2 Aqueous Phase

**Dissociation.** Figure 4.4c shows the crossing probability along the reaction coordinate for the dissociation in the aqueous phase. As mentioned above, an accurate evaluation of the activation energy is difficult to obtain for large systems and this was confirmed by our analysis which did not convergence enough to provide a meaningful result. Instead, we show the free energy barrier at 350 K obtained from Ref. 16 as a reference. Table 4.1b shows the flux through $\lambda_A = 1.85$ Å and overall crossing probability. The rate constants of dissociation in the aqueous phase is about 160 times smaller than in the gas phase implying that the aqueous solution stabilizes the five-coordinated silicate dimer. The length of the reactive trajectories ranged between 0.15 and 4.0 ps.

Representative snapshots for the mechanisms of the dissociation process are shown in figure 4.5. The dissociation process can occur through two possible mechanisms which are distinguished from each other by the presence or the absence of an additional proton transfer step. Figure 4.5a and 4.5b show two trajectories involving the proton transfer mechanism while figure 4.5c shows a reactive trajectory which does not involve a proton transfer. Just like the gas-phase reaction two hydroxyl groups (labeled 1 and 2) at the five-coordinated silicate group tend to point their hydrogens (colored green and purple, respectively) in the direction of the intermediate bridging oxygen. Our path sampling simulations produce reactive transitions which involve either the transfer of hydrogen number 1 (Figure 4.5a) or number 2 (Figure 4.5b). The fact that the RETIS simulation manages to produce both types of trajectories provides confidence that the sampling is ergodic. Although the orientation of the hydroxyl groups look initially symmetric, just like the gas-phase reaction, the symmetry is sometimes broken by the solvent structure which seems to catalyze the proton transfer step. Figure 4.5a and 4.5b show the presence of water molecule (with its oxygen colored orange) forming a hydrogen bond with the bridging oxygen atom. The hydrogen bond creates a pulling force on the bridging oxygen which brings the oxygen closer towards one of the hydroxyl groups 1 or 2 which enables the proton transfer at the point where the silicon-oxygen bond breaks. In the reactive trajectories where the hydrogen bond is absent no proton transfer was observed (like in figure 4.5c) similar to the gas phase reaction. In all cases where the bridging oxygen accepted a hydrogen bond from the solvent, the proton transfer from one of the two hydroxyl groups always occurred at the side of the water molecule donating the bond. Although both mechanisms contribute to the dissociation of the silicate complex, our results infer that the mechanism with proton transfer is predominant with a probability of about 80% compared to the mechanism without proton transfer.

**Removal of water.** The energy barrier for water removal step is higher than dissociation process [10, 11, 13]. Free energy for the water removal step in the silicate dimerization has a maximum at silicon-oxygen distance 2.4 Å [13]. Figure 4.4d illustrates the overall crossing probability as function of reaction coordinate for the water removal step. It clearly shows a plateau at 2.4 Å, indicating that the barrier of water removal step has been crossed. The flux and overall crossing probability are shown in table 4.1b. The rate constant for the water removal step is almost one order of magnitude less than dissociation process and is about $2.04{\times}10^7\ s^{-1}$. The length of trajectories ranges from 0.06 to 40 ps depending on the mechanism and number of water molecules involved in the proton transfer process.

During the water removal process, one hydroxyl group leaves the five-coordinated silicon, remains in the solution for a while, and then receives a proton, neutralizing the $OH^-$ ion. The last step can either occur directly via the silicate complex (internal) or by means

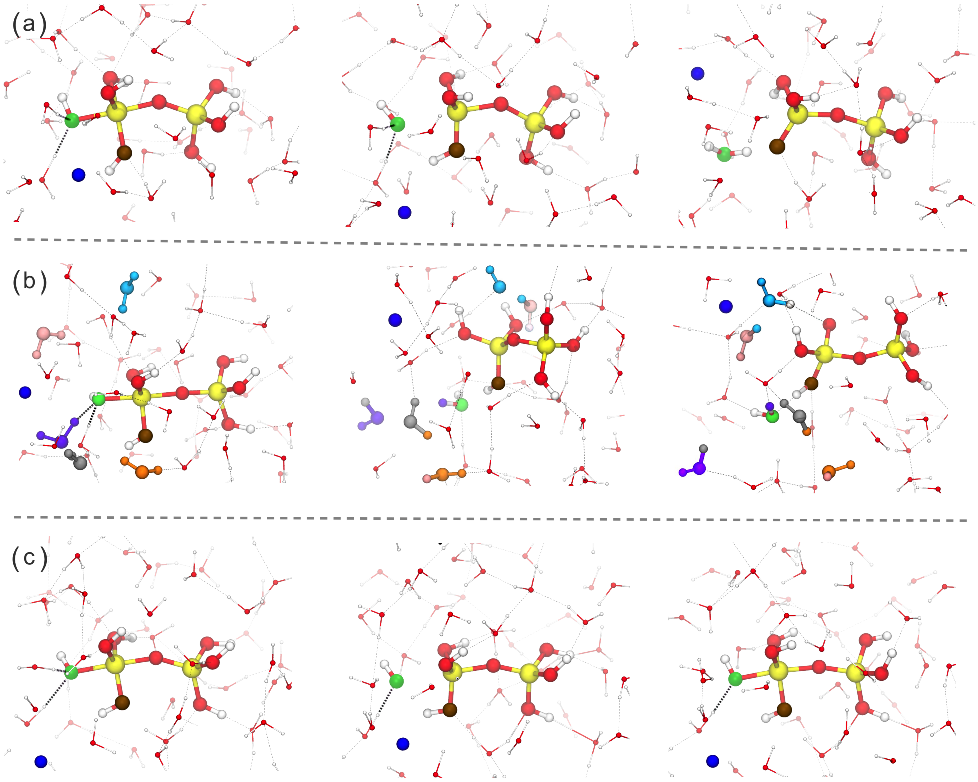

**Figure 4.6:** Representative snapshots of water removal step in the silicate dimerization process. The oxygen of leaving OH group and $Na^+$ ion are shown in green and blue colors respectively. (a) Internal mechanism: Proton transfers directly from the deprotonation of a Si−OH group (b) External mechanism: Proton transfer occurs through the Grotthuss mechanism. Water molecules involved in the hydrogen bonds network are shown bold and different colors, (c) Non-reactive trajectory and effect of the presence and absence of hydrogen bonds on the leaving OH group in the water removal step. In the first frame of the three trajectories always one hydroxyl group is pointed towards the leaving OH group (colored brown). It is this hydroxyl group that always gets deprotonated in the internal mechanism and most often in the external mechanism as well (but not for trajectory (b)). Having at least two hydrogen bonds between the leaving OH group and the solvent seems a prerequisite for the reaction to succeed. The second frame of trajectory (c) shows that only one hydrogen bond remained after the initial release and since the OH group is still in the vicinity of the silicate complex the five-coordinated silicate complex is quickly reformed.

of the solvent via a hydrogen bond network (external). The internal proton transfer mechanism implies that the leaving OH group receives a proton directly via a deprotonation of a Si−OH group, while in the external proton transfer, one or several water molecules transfer their proton through a hydrogen bond wire via a Grotthuss mechanism [63]. This process ends when the Si−OH group releases a proton neutralizing the $OH^-$ ion. Hence, in both cases the reaction ends after the deprotonation of a Si$-$OH group generating the anionic silicate dimer $H_5Si_2O_7{}^-$ (see figure 4.6).

Despite that the reaction coordinate is flexible, not specifying which hydroxyl group at the five-coordinated silicon should release (see figure 4.2b), our simulation showed that the leaving OH group is always the group most distant from the other silicon (with its oxygen colored green in figure 4.6). In addition, the simulations reveal that both internal and external mechanisms contribute to the overall reaction, though the internal proton transfer is favored and happens in 58% of the occasions. Previous studies suggested that the hydroxyl release step occurs simultaneously with the deprotonation of the Si$-$OH group [10,11,13]. However, our study indicates that the OH group remains in the solution 0.06$-$3.5 ps in the internal mechanism and 0.1$-$40 ps in the external mechanism before it neutralizes. Hence, the reaction forming the anionic silicate dimer $H_5Si_2O_7{}^-$ is stepwise and not concerted. This illustrates the advantage of the RETIS approach compared to constrained MD. In the constrained MD simulations, the release of the OH group occurs more gradually since at each increment of the reaction coordinate its value is fixed for a while and the system is given time to adapt to the new situation. In the unbiased MD trajectories harvested by the RETIS algorithm, there is no adaptation time and the hydroxyl can escape into the solvent without giving a chance to the rest of the silicate complex to release its proton. Hence, RETIS is able to disclose the true dynamical evolution of a complex process. Figure 4.6 shows the selected snapshots for initial stages of water removal process. In most cases, as shown in figure 4.6a and 4.6b, one of Si$-$OH groups (oxygen colored in brown) on the five-coordinated silicon is pointing towards the leaving OH group, acting as a proton donor to the hydroxide via an internal proton transfer. Also for the cases in which the proton transfers externally, i.e. via the solvent, it is this hydroxyl group that most often releases its proton. However, if the release of the OH group is not rapidly follow-up by the proton release, also the other hydroxyl groups may act as proton donor (as in figure 4.6b). In 24% of the cases of the external proton transfer a Si$-$OH group from the four-coordinate silicon acts as proton donor. This can occur when the hydroxide ion has sufficient time to effectively diffuse (via the Grotthuss mechanism) towards the four-coordinated silicon. In some but not all cases this happens via the periodic boundaries. Figure 4.7 shows the time distribution of the reactive trajectories indicating the time interval between OH release and silicate deprotonation for both internal and external mechanism. Clearly, the average trajectory length of the external mechanism is considerably longer than that of the internal mechanism. This is a result of the external mechanism consisting of several proton transfer reaction steps.

However, as can be seen from figure 4.7a, also the internal mechanism has a relatively broad double peaked distribution. This is because also in the internal mechanism solvent molecules can participate in intermediate reaction steps. The released OH group then receives a proton from the solvent but eventually gives it back and finally accepts a pro-

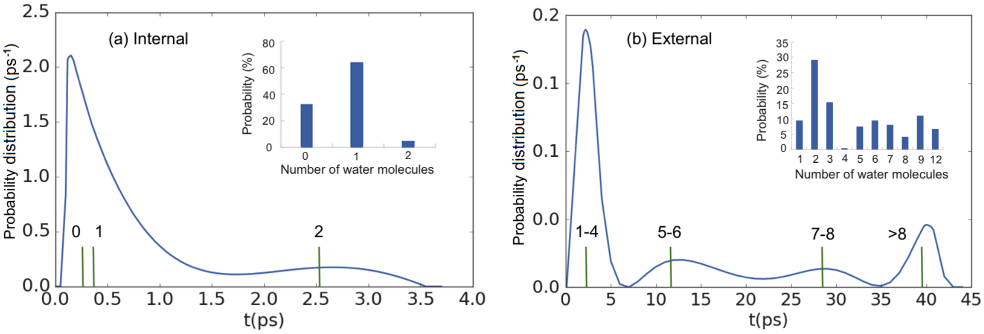

**Figure 4.7:** Time distribution of the reactive trajectories indicating the time interval between OH group release and silicate deprotonation for (a) internal mechanism and (b) external mechanism. The inset (a) shows number of water molecules involved in temporary proton excursions in the internal mechanism. The inset (b) shows number of water molecules involved in the hydrogen wire in the external mechanism of water removal step. Vertical lines show the average trajectory length with respect to the number of water molecules involved in the hydrogen bond wire.

ton from the silicate complex. We observed that there can be a maximum of two water molecules involved in these temporary proton excursions as shown in the inset of figure 4.7a. The double peaked distribution is a direct result of having either zero or one solvent molecule or two molecules involved.

In the external mechanism, the proton transfer occurs along a hydrogen bond wire. Water molecules in solution construct a hydrogen bonds network that facilitates the water removal step. The inset of figure 4.7b shows the number of water molecules involved in the hydrogen wire before neutralization occurs via the deprotonation of the silicate. In some cases, the proton transfer from a solvent molecule towards the hydroxide jumps back after a very short time. These water molecules were not counted as being part of the hydrogen bond wire. The silicon deprotonation seems irreversible which is in contrast to what constraint molecular dynamics suggest [13].

Figure 4.6c shows a non-reactive trajectory in the water removal step. We observed that at least two hydrogen bonds are required to pull and dissociate the OH group from the five-coordinate silicon. These hydrogen bonds are essential to depart the hydroxyl group from silicate in opposite directions and to avoid the recombination process. After that the hydroxide ion can participate in the Grotthuss mechanism and becomes neutralized.

## 4.5 Conclusions

In this paper, we have performed a path sampling simulation based on the RETIS algorithm in combination with Ab Initio molecular dynamics to investigate the mechanisms and the rate of silicate dimerization reactions in gas and aqueous phase. For this purpose, we generated in total around one hundred thousand trajectories. Regarding force evaluations, each reaction study in the aqueous phase corresponded to ca. 1000-1400 ps. Still, by means of the RETIS rare event approach, we obtain inverse rate constants (the expectation time of the chemical event) as high as 50 000 ps and a couple of thousands reactive trajectories. In other words, the RETIS simulations provide results which would otherwise require a 100 $\mu$s brute force molecular dynamics simulation which is far beyond reach for Ab Initio molecular dynamics.

As expected, the RETIS simulations show that the rates of SiO$-$Si bond dissociation in the aqueous phase is relatively reduced, compared to the gas phase results. This implies that the aqueous solution stabilizes the five-coordinated silicate dimer. Interestingly, the dissociation of silicate complex in the aqueous phase may either occur via a proton assisted mechanism or via a mechanism without proton transfer. We highlighted the role and importance of water molecule arrangement in the dissociation mechanism. A water molecule forms a hydrogen bond with the bridging oxygen atom in silicate complex and causes a pulling force on the oxygen towards one of the hydroxyl groups and enables the proton transfer at the silicon-oxygen bond breakage point. The mechanism with proton transfer is highly predominant compared to the mechanism without proton transfer.

Also the water removal step may occur through two possible mechanisms, the internal and external mechanism, which are distinguished by the proton transfer reaction path. This implies that proton transfer can either occur via a direct or via a water mediated reaction step. In the internal proton transfer mechanism the leaving hydroxyl group accepts a proton directly via a silicate deprotonation step, while in the external proton transfer, one or several water molecules transfer their protons through a hydrogen bond wire via a Grotthuss mechanism. Previous studies have provided contradicting conclusions regarding the role of solvent in the water removal step in the silicate dimerization reaction as some have reported that it occurs solely via the internal mechanism [10] while other studies suggest it occurs via the external mechanism [13]. More recently, McIntosh [11] observed both mechanisms, but claimed that it is unlikely that the external proton transfer is competitive with the direct proton transfer. In contrast, the unbiased dynamical trajectories generated by the RETIS simulation show that both mechanisms can occur and the internal mechanism only is slightly favorable compared to the external mechanism. The length of these trajectories highly depend on the mechanisms and number of water molecules involved in the hydrogen bonds wire. The presence of hydrogen bonds between the leaving hydroxyl group and the solvent acts as a prerequisite for the reaction to succeed.

In summary, RETIS allowed the calculation of rate constants as well as to give valuable insight into which reaction mechanism dominates when dynamics and explicit solvent are taken into account. We believe that the technique presented here can open many possible avenues in the field of silicate oligomerization reactions and chemical reactions in general. Besides the fundamental new insight, these type of simulations will eventually help to obtain a better control of chemical reactions and provide new inspiration for alternative synthesis methods.

## Acknowledgments

The authors thank the Research Council of Norway project no. 237423 and the Faculty of Natural Sciences and Technology (NTNU) for support. Computational resources were granted by The Norwegian Metacenter for Computational Science (NOTUR), project NN9254K.

# Bibliography

[1] P. E. A. de Moor, T. P. M. Beelen, R. A. van Santen, K. Tsuji, and M. E. Davis. SAXS and USAXS investigation on nanometer-scaled precursors in organic-mediated zeolite crystallization from gelating systems. *Chem. Mater.*, 11:36–43, 1999.

[2] P. E. A. de Moor, T. P. M. Beelen, R. A. van Santen, L. W. Beck, and M. E. Davis. Si-MFI crystallization using a Dimer and Trimer of TPA studied with small-angle X-ray scattering. *J. Phys. Chem. B*, 104:7600–7611, 2000.

[3] A. R. Felmy, H. Cho, James R. Rustad, and M. J. Mason. An aqueous thermodynamic model for polymerized silica species to high ionic strength. *J. Solution Chem.*, 30:509–525, 2001.

[4] J. M. Fedeyko, D. G. Vlachos, and R. F. Lobo. Formation and structure of self-assembled silica nanoparticles in basic solutions of organic and inorganic cations. *Langmuir*, 21:5197–5206, 2005.

[5] S. A. Pelster, W. Schrader, and F. Schüth. Monitoring temporal evolution of silicate species during hydrolysis and condensation of silicates using mass spectrometry. *J. Am. Chem. Soc.*, 128:4310–4317, 2006.

[6] J. C. G. Pereira, C. R. A. Catlow, and G. D. Price. Silica condensation reaction: An ab initio study. *Chem. Commun.*, 115:1387–1388, 1998.

[7] J. C. G. Pereira, C. R. A. Catlow, and G. D. Price. Ab initio studies of silica-based clusters. part I. energies and conformations of simple clusters. *J. Phys. Chem. A*, 103:3252–3267, 1999.

[8] J. C. G. Pereira, C. R. A. Catlow, and G. D. Price. Ab initio studies of silica-based clusters. part II. structures and energies of complex clusters. *J. Phys. Chem. A*, 103:3268–3284, 1999.

[9] M. J. Mora-Fonz, C. R. A. Catlow, and D. W. Lewis. Oligomerization and cyclization processes in the nucleation of microporous silicas. *Angew. Chem. Int. Ed.*, 44:3082–3086, 2005.

[10] T. T. Trinh, A. P. J. Jansen, R. A. van Santen, and E. Jan Meijer. The role of water in silicate oligomerization reaction. *Phys. Chem. Chem. Phys.*, 11:5092–5099, 2009.

[11] G. J. McIntosh. A theoretical kinetic model of the temperature and ph dependent dimerization of orthosilicic acid in aqueous solution. *Phys. Chem. Chem. Phys.*, 14:996–1013, 2012.

[12] T. T. Trinh, X. Rozanska, F. Delbecq, and P. Sautet. The initial step of silicate versus aluminosilicate formation in zeolite synthesis: a reaction mechanism in water with a tetrapropylammonium template. *Phys. Chem. Chem. Phys.*, 14:3369–3380, 2012.

[13] A. Pavlova, T. T. Trinh, R. A. van Santen, and E. J. Meijer. Clarifying the role of sodium in the silica oligomerization reaction. *Phys. Chem. Chem. Phys.*, 15:1123–1129, 2013.

[14] G. J. McIntosh. Theoretical investigations into the nucleation of silica growth in basic solution part II derivation and benchmarking of a first principles kinetic model of solution chemistry. *Phys. Chem. Chem. Phys.*, 15:17496–17509, 2013.

[15] G. J. McIntosh. Theoretical investigations into the nucleation of silica growth in basic solution part I ab initio studies of the formation of trimers and tetramers. *Phys. Chem. Chem. Phys.*, 15:3155–3172, 2013.

[16] M. Moqadam, E. Riccardi, T. T. Trinh, P.-O. Åstrand, and T. S. van Erp. A test on reactive force fields for the study of silica dimerization reactions. *J. Chem. Phys.*, 143:184113–8, 2015.

[17] J. A. Tossell. Theoretical study on the dimerization of $Si(OH)_4$ in aqueous solution and its dependence on temperature and dielectric constant. *Geochim. Cosmochim. Acta*, 69:283–291, 2005.

[18] Y. T. Xiao and A. C. Lasaga. Ab initio quantum mechanical studies of the kinetics and mechanisms of quartz dissolution: OH-catalysis. *Geochim. Cosmochim. Acta*, 60:2283–2295, 1996.

[19] H. Hu, H. Hou, Z. He, and B. Wang. Theoretical characterizations of the mechanism for the dimerization of monosilicic acid in basic solution. *Phys. Chem. Chem. Phys.*, 15:15027–15032, 2013.

[20] T. T. Trinh, A. P. J. Jansen, R. A. van Santen, and E. J. Meijer. Role of water in silica oligomerization. *J. Phys. Chem. C*, 113:2647–2652, 2009.

[21] T. T. Trinh, A. P. J. Jansen, and R. A. Santen. Mechanism of oligomerization reactions of silica. *J. Phys. Chem. B*, 110:23099–23106, 2006.

[22] T. T. Trinh, A. P. Jansen, R. A. van Santen, J. VandeVondele, and E. J. Meijer. Effect of counter ions on the silica oligomerization reaction. *Comput. Phys. Commun.*, 10:1775–1782, 2009.

[23] E. A. Carter, G. Ciccotti, J. T. Hynes, and R. Kapral. Constrained reaction coordinate dynamics for the simulation of rare events. *Chem. Phys. Lett.*, 156:472–477, 1989.

[24] J. Tersoff. New empirical model for the structural properties of silicon. *Phys. Rev. Lett.*, 56:632–635, 1986.

[25] F. H. Stillinger and T. A. Weber. Computer simulation of local order in condensed phases of silicon. *Phys. Rev. B*, 31:5262–5271, 1985. Erratum in 33, 1451, 1986.

[26] F. H. Stillinger and T. A. Weber. Fluorination of the dimerized Si(100) surface studied by molecular-dynamics simulation. *Phys. Rev. Lett.*, 62:2144–2147, 1989.

[27] D. Kohen, J. C. Tully, and F. H. Stillinger. Modeling the interaction of hydrogen with silicon surfaces. *Surf. Sci.*, 397:225–236, 1998.

[28] A. Ostadhossein, E. D. Cubuk, G. A. Tritsaris, E. Kaxiras, S. Zhang, and A. C. T. van Duin. Stress effects on the initial lithiation of crystalline silicon nanowires: reactive molecular dynamics simulations using ReaxFF. *Phys. Chem. Chem. Phys.*, 17:3832–3840, 2015.

[29] A. C. T. van Duin, S.h Dasgupta, F. Lorant, and W. A. Goddard. ReaxFF: A reactive force field for hydrocarbons. *J. Phys. Chem. A*, 105:9396–9409, 2001.

[30] S. Agrawalla and A. C. T. van Duin. Development and application of a ReaxFF reactive force field for hydrogen combustion. *J. Phys. Chem. A*, 115:960–972, 2011.

[31] A. C. T. van Duin, A. Strachan, S. Stewman, Q. Zhang, X. Xu, and W. A Goddard. ReaxFF$_{SiO}$ reactive force field for silicon and silicon oxide systems. *J. Phys. Chem. A*, 107:3803–3811, 2003.

[32] W. M. Young and E. W. Elcock. Monte carlo studies of vacancy migration in binary ordered alloys: I. *Proc. Phys. Soc. London*, 89:735–746, 1966.

[33] X. Zhang, T. T. Trinh, R. A. van Santen, and A. P. J. Jansen. Structure-directing role of counterions in the initial stage of zeolite synthesis. *J. Phys. Chem. C*, 115:9561–9567, 2011.

[34] X. Zhang, T. T. Trinh, R. A. van Santen, and A. P. J. Jansen. Mechanism of the initial stage of silicate oligomerization. *J. Am. Chem. Soc.*, 133:6613–6625, 2011.

[35] M. Ciantar, C. Mellot-Draznieks, and C. Nieto-Draghi. A kinetic Monte Carlo simulation study of synthesis variables and diffusion coefficients in early stages of silicate oligomerization. *J. Phys. Chem. C*, 119:28871–28884, 2015.

[36] J. C. Fogarty, H. M. Aktulga, A. Y. Grama, A. C. T. Van Duin, and S. A Pandit. A reactive molecular dynamics simulation of the silica-water interface. *J. Chem. Phys.*, 132:174704–174710, 2010.

[37] H. R. Larsson, A. C. T. van Duin, and B. Hartke. Global optimization of parameters in the reactive force field ReaxFF for SiOH. *J. Comput. Chem.*, 34:2178–2189, 2013.

[38] C. Dellago, P. G. Bolhuis, F. S. Csajka, and D. Chandler. Transition path sampling and the calculation of rate constants. *J. Chem. Phys.*, 108:1964–1977, 1998.

[39] T. S. van Erp, D. Moroni, and P. G. Bolhuis. A novel path sampling method for the calculation of rate constants. *J. Chem. Phys.*, 98:7762–7774, 2003.

[40] T. S. van Erp. Reaction rate calculation by parallel path swapping. *Phys. Rev. Lett.*, 98:268301–4, 2007.

[41] P. L. Geissler, C. Dellago, D. Chandler, J. Hutter, and M. Parrinello. Autoionization in liquid water. *Science*, 291:2121–2124, 2001.

[42] B. Ensing, , and E. J. Baerends. Reaction path sampling of the reaction between iron(II) and hydrogen peroxide in aqueous solution. *J. Phys. Chem. A*, 106:7902–7910, 2002.

[43] G. Reinisch, J. Leyssale, and G. L. Vignoles. Theoretical study of the decomposition of $BCl_3$ induced by a h radical. *J. Phys. Chem. A*, 115:4786–4797, 2011.

[44] Z. Wang, D. Antoniou, S. D. Schwartz, and V. L. Schramm. Hydride transfer in DHFR by transition path sampling, kinetic isotope effects, and heavy enzyme studies. *Biochemistry*, 55:157–166, 2016.

[45] R. Car and M. Parrinello. Unified approach for molecular dynamics and density-functional theory. *Phys. Rev. Lett.*, 55:2471–2474, 1985.

[46] CP2K: High Performance Computing, http://www.nanosim.mat.ethz.ch/ research/cp2k.

[47] T. Dauxois, M. Peyrard, and A. R. Bishop. Entropy-driven DNA denaturation. *Phys. Rev. E*, 47:R44–R47, 1993.

[48] C. Dellago, P. G. Bolhuis, and D. Chandler. Efficient transition path sampling: Application to lennard-jones cluster rearrangements. *J. Chem. Phys.*, 108:9236–9245, 1998.

[49] T. S. van Erp and P. G. Bolhuis. Elaborating transition interface sampling methods. *J. Comp. Phys.*, 205:157–181, 2005.

[50] C. Dellago and P. G. Bolhuis. Activation energies from transition path sampling simulations. *Mol Simul*, 30:795–799, 2004.

[51] J. VandeVondele, M. Krack, F. Mohamed, M. Parrinello, T. Chassaing, and J. Hutter. Quickstep: Fast and accurate density functional calculations using a mixed Gaussian and plane waves approach. *Comput. Phys. Commun.*, 167:103–128, 2005.

[52] A. D. Becke. Density-functional exchange-energy approximation with correct asymptotic behavior. *Phys. Rev. A*, 38:3098–3100, 1988.

[53] C. Lee, W. Yang, and R. G. Parr. Development of the Colle-Salvetti correlation-energy formula into a functional of the electron density. *Phys. Rev. B*, 37:785–789, 1988.

[54] J. Andzelm J. Baker, M. Muir and A. Scheiner. Hybrid Hartree-Fock density-functional theory functionals: The adiabatic connection method. *ACS Symposium Series*, 629:342–367, 1996.

[55] S. Grimme. Semiempirical GGA-type density functional constructed with a long-range dispersion correction. *J. Comput. Chem.*, 27:1787–1799, 2006.

[56] S. Goedecker, M. Teter, and J. Hutter. Separable dual-space Gaussian pseudopotentials. *Phys. Rev. B*, 54:1703–1710, 1996.

[57] C. Hartwigsen, S. Goedecker, and J. Hutter. Relativistic separable dual-space Gaussian pseudopotentials from H to Rn. *Phys. Rev. B*, 58:3641–3662, 1998.

[58] M. Sprik, J. Hutter, and M. Parrinello. Ab initio molecular dynamics simulation of liquid water: Comparison of three gradient-corrected density functionals. *J. Chem. Phys.*, 105:1142–1152, 1996.

[59] J. VandeVondele and J. Hutter. Gaussian basis sets for accurate calculations on molecular systems in gas and condensed phases. *J. Chem. Phys.*, 127:114105–114105, 2007.

[60] S. Grimme, S. Ehrlich, and L. Goerigk. Effect of the damping function in dispersion corrected density functional theory. *J. Comput. Chem.*, 32:1456–1465, 2011.

[61] G. Maroulis. *Computational Aspects of Electric Polarizability Calculations: Atoms, Molecules and Clusters*. IOS Press, Amsterdam, 2006.

[62] T. S. van Erp and E. J. Meijer. Proton assisted ethylene hydration in aqueous solution. *Angew. Chemie*, 43:1659–1662, 2004.

[63] C. J. T. de Grotthuss. Memoir on the decomposition of water and of the bodies that it holds in solution by means of galvanic electricity. *Biochimica et Biophysica Acta*, 1757:871–875, 2006.

# Chapter 5

# Analyzing Complex Reaction Mechanisms Using Path Sampling

Titus S. van Erp, Mahmoud Moqadam, Anders Lervik, Enrico Riccardi

J. Chem. Theory Comput. 12, 5398, (2016)

**Abstract -** We introduce an approach to analyze collective variables regarding their predictive power for a reaction. The method is based on already available path sampling data produced by for instance transition interface sampling or forward flux sampling which are path sampling methods used for efficient computation of reaction rates. By a search in collective variable space a measure of predictiveness can be optimized and, in addition, the number of collective variables can be reduced using projection operations which keep this measure invariant. The approach allows testing hypotheses on the reaction mechanism, but could in principle also be used to construct the phase space committor surfaces without the need of additional trajectory sampling. The procedure is illustrated for a one-dimensional double well potential, a theoretical model for an ion-transfer reaction in which the solvent structure can lower the barrier, and an Ab Initio molecular dynamics study of water auto-ionization. The analysis technique enhances the quantitative interpretation of path sampling data which can provide clues on how chemical reactions can be steered in desired directions.

## 5.1 Introduction

Systematic approaches to analyze reaction mechanisms in terms of descriptive reaction coordinates have been focused on committor analysis [1–7]. The committor function tells for each phase point or configuration point what the probability is that a dynamical trajectory launched from that point will end up in the product state rather than the reactant state. Points having the same committor value form iso-committor surfaces. A reaction can then be described by a Markov process in which the system moves from one iso-committor surface to another one. The committor can, hence, be interpreted as a progress coordinate and a growing number of researchers in the field believe it should be viewed as the true reaction coordinate. Literature is, however, not always consistent whether the phase space or configuration space committor should be considered. In principle only the phase space committor gives the full mechanistic information [8, 9], but the configurational committor fits better into the original concept of reaction coordinate which is traditionally a purely geometric function [10]. Moreover, the determination of the committor surfaces is computationally intensive since it requires the release of many trajectories from each individual phase- or configuration-point. Although there are systematic approaches based on genetic neural networks [11] and Bayesian techniques [4, 5] which can reduce the computational burden, accurate determination of the committor values is difficult especially for low values. Hence, computational studies investigating the committor generally tend to focus on the surface with committor value $1/2$, the separatrix. Therefore, a systematic analysis on the required conditions, of how and when the system can reach the separatrix, has received much less attention.

On one hand, the beauty of the phase-space and configurational-space committors is that they are mathematically well-defined and do not require any pre-assumptions or chemical intuition. On the other hand, however, this also implies a disadvantage. If a divine power would give us the full phase space committor (from which the configurational committor can be obtained by velocity averaging) as an exact nonlinear function of all atom positions and velocities, it will not directly give us a lot of insight. We would probably not be able to make any sense out of this multi-dimensional nonlinear function unless we could simplify it, if necessary through approximations, and rewrite it in a human understandable function of just a few parameters to which we can relate to; i.e parameters based on well-known concepts which are intuitive. An example of such a concept is that of the hydrogen bond (or any chemical bond in general) and order parameters based on it such as the number of hydrogen bonds that a specific molecule donates or accepts. Although there is not a single unique microscopic definition for something like a hydrogen bond [12, 13], it provides a tool which helps our understanding of solvent dynamics and the functioning of bio-molecules such as DNA. The knowledge that some well-ordered hydrogen-bonded water networks are essential for reactions [14, 15] might eventually lead to rationalized approaches to steer chemical reactions, produce new materials, or design more efficient catalysts.

So in one way or another, we need to translate our findings into intuitively understandable parameters, in other words, gaining an understanding of the reaction mechanism. In this chapter, we introduce an analysis method to test hypotheses about the reaction mechanism and to identify the essential circumstances which make a reaction proceed or not. The analysis method uses the path sampling data which are produced by rare event sampling methods such as transition interface sampling (TIS) [16], replica exchange TIS (RETIS) [17], and forward flux sampling [18]. These methods employ a Monte Carlo (MC) sampling of trajectories within a series of simulations, each evaluating a different path ensemble.

A trajectory belongs to an ensemble whenever it starts at the boundary of the reactant state, moves along the barrier up to a certain minimum progression, and then either ends by re-entering the reactant state or entering the product state. The minimum progression requirement is enforced by an interface crossing condition: associated with each path ensemble there is an unique interface defined by the value of the progress coordinate ("reaction coordinate") which needs to be crossed. The results from the different path ensembles can be combined and allow one to obtain the reaction rate without additional approximations, but orders of magnitude faster than straight-forward molecular dynamics (MD). Although the progress coordinate in the TIS methods [16–18] is not related to the committor, some have argued that the committor as progress coordinate [19] would give the best possible efficiency for these methods. However, it should be noted that there is a crucial difference between TIS and RETIS on the one hand and FFS on the other hand regarding the efficiency scaling. Whereas the efficiency of TIS and RETIS is relatively insensitive to the choice of progress coordinate and outperforms standard free energy based methods to compute rates whenever both are based on a poor reaction coordinate, FFS is doing worse than the standard methods in that case [20, 21]. It is interesting to note that Ref. 19 actually refers to the phase space committor implying that the reaction coordinate providing the most efficient sampling should be momentum-dependent, something which is very unusual. However, as shown in Ref. 21, FFS indeed requires such momentum-dependent reaction coordinate in an underdamped one-dimensional system while it is neither needed nor more efficient for TIS and RETIS.

The aim of our analysis method is, therefore, not finding the committor or a single coordinate per se. Rather, it tries to identify which additional coordinates (possibly momentum-dependent) other than the chosen reaction coordinate determine the progress of the reaction. Though, as we will show below, in principle our method can also be used to determine the full phase-space committor just using the data of the TIS methods. Our chapter is organized as follows. In Section 5.2 we give the theoretical definitions that are being used in our methodology. In Section 5.3 we show how these theoretical measures of predictiveness can be computed using path sampling data from TIS, RETIS or FFS. In Section 5.4, we show numerical results for a one-dimensional double well potential, a theoretical model for an ion-transfer reaction, and an Ab Initio molecular dynamics study of water auto-ionization. In Section 5.5 we elaborate further on the possibilities of our methodology, in particular we discuss how the number of CVs can be reduced while maintaining the same predictive power and how that ultimately can be used to determine the phase space committor. We end with concluding remarks in Section 5.6.

## 5.2 Definitions

TIS, FFS, and RETIS are based on a partitioning of the phase space using interfaces (from here on called TIS interfaces). Let $\lambda(x)$ be a progress coordinate which is in principle a function of phase space point $x$. In many cases it can be taken as a geometric function like the length of a bond that needs to be broken, the largest solid cluster in a nucleation study, the radius of gyration for protein folding, etc. Then, the collection of phase points $x$ having a specific value $\lambda_i$ form the interfaces. This implies that $\{x|\lambda(x) = \lambda_i\}$ comprises interface number $i$. In the case of $M + 1$ interfaces, $\lambda_0 = \lambda^A$ is placed within the reactant well, $\lambda_M = \lambda^B$ is placed in the product well, and the interfaces in between, $\lambda_i$ for $0 < i < M$, are placed in the barrier region. Here, we use the subscript notation to indicate the integer index for the TIS interfaces and a superscript to indicate a specific value of the $\lambda$-parameter. The system is then considered belonging to the *overall state* $\mathcal{A}$ if it crossed $\lambda^A$ more recently than $\lambda^B$. If there is a clear separation of time scales, the overall states will be insensitive to the exact positioning of $\lambda^A$ and $\lambda^B$ as long as they are reasonable; it is assumed that once $\lambda^A$ or $\lambda^B$ is crossed from the barrier region side the system will relax to that respective state (commit). The other interfaces are placed in order to maximize efficiency.

Within the TIS theory, the rate constant $k_{AB}$ is defined as the number of transitions from *overall state* $\mathcal{A}$ to *overall state* $\mathcal{B}$ per time unit which can be expressed as the flux through $\lambda^A$ times the overall crossing probability $\mathcal{P}_A(\lambda_M|\lambda_0)$. The last term equals the chance that the system will cross $\lambda_M$ before $\lambda_0$ provided that it just crossed $\lambda_0$ in the positive direction (as convention we assume that the reactant state and the product state are situated at the left and right side of the barrier, respectively). This probability is generally too low to be determined directly, but it can be computed by a series of path simulations using the following relation [16]

$$\mathcal{P}_A(\lambda_M|\lambda_0) = \prod_{i=1}^{M} \mathcal{P}_A(\lambda_i|\lambda_{i-1}) \tag{5.1}$$

Here, $\mathcal{P}_A(\lambda_i|\lambda_{i-1})$ is the conditional probability that the system coming from $\lambda_0$ and then crossing $\lambda_{i-1}$ for the first time will cross $\lambda_i$ as well before recrossing $\lambda_0$ again. Naturally, $\mathcal{P}_A(\lambda_i|\lambda_{i-1})$ will be much larger than the overall crossing probability whenever $\lambda_i$ is sufficiently close to $\lambda_{i-1}$ and this property can be computed by Monte Carlo walk in path space.

We denote with $X$ a path of $L+1$ time slices

$$X = \{x_0, x_1, \ldots, x_L\} \tag{5.2}$$

where $L$ is the path length and $x_k$ is the $k$-th phase point of the path, also called time slice. We will further refer to the nomenclature of RETIS where the path ensemble $[i^+]$ comprises the collection of trajectories with the following properties:

$$\begin{aligned} X \in [i^+] \ \text{ if:} & \\ & \lambda(x_0) < \lambda_0, \\ & \lambda(x_L) < \lambda_0 \text{ or } \lambda(x_L) > \lambda_M, \\ & \lambda_0 < \lambda(x_k) < \lambda_M \text{ for } k = 1, 2, \ldots, L-1, \\ & \lambda_{\max} \equiv \max[\lambda(x_1), \lambda(x_2), \ldots, \lambda(x_L)] > \lambda_i \end{aligned} \tag{5.3}$$

We define characteristic binary functions which relate to whether $X$ is within $[i^+]$ or not

$$h_i(X) = 1 \ \text{ if } \ X \in [i^+], \quad 0 \ \text{ otherwise} \tag{5.4}$$

and the weight, $\varrho_i(X)$, of a path in ensemble $[i^+]$ is given by

$$\varrho_i(X) = h_i(X)\rho(x_0) \prod_{k=0}^{L-1} p(x_k \to x_{k+1}) \tag{5.5}$$

Here, $\rho$ is the phase space density and $p(x_k \to x_{k+1})$ are the hopping probability densities; the chance that the system moves to phase point $x_{k+1}$ in a single $\Delta t$ time step given that it is in $x_k$. An ensemble average of an arbitrary path function $a(X)$ in the $[i^+]$ ensemble equals

$$\langle a(X) \rangle_{\varrho_i} = \frac{\int a(X)\varrho_i(X)\mathcal{D}X}{\int \varrho_i(X)\mathcal{D}X} \tag{5.6}$$

where the integral is formally equal to $\int \ldots \mathcal{D}X = \sum_{L=1,\infty} \int \cdots \prod_{k=0,L} \mathrm{d}x_k$. In practice, however, we only compute ratios of two path space integrals like the one of equation 5.6 using MC in trajectory space. In this method we collect a Markov chain of trajectories for specific path ensembles using MC moves (like e.g. shooting [22]) obeying detailed balance $\varrho_i(X^{(\mathrm{o})})P_{\mathrm{gen}}(X^{(\mathrm{o})} \to X^{(\mathrm{n})})P_{\mathrm{acc}}(X^{(\mathrm{o})} \to X^{(\mathrm{n})}) = \varrho_i(X^{(\mathrm{n})})P_{\mathrm{gen}}(X^{(\mathrm{n})} \to X^{(\mathrm{o})})P_{\mathrm{acc}}(X^{(\mathrm{n})} \to X^{(\mathrm{o})})$ where $X^{(\mathrm{o})}$ and $X^{(\mathrm{n})}$ are the old and new paths, respectively, and $P_{\mathrm{gen}}$ and $P_{\mathrm{acc}}$ are the generation and acceptance probabilities of the MC algorithm. Equation 5.6 is then a simple average of the simulation $\langle a(X) \rangle_{\varrho_i} \approx \frac{1}{N_{\mathrm{sim}}} \sum_{n=1,N_{\mathrm{sim}}} a(X_n)$ where $X_n$ is the $n$-th path sampled in the simulation and $N_{\mathrm{sim}}$ is the total number of paths.

In the following we will focus on first crossing points with interfaces as defined by our progress coordinate. We define $x^{\lambda^c}$ as the first crossing point with interface $\lambda^c$:

$$\begin{aligned} & x^{\lambda^c}(X) = x_k \in X \text{ if } \lambda(x_k) \geq \lambda^c \\ & \text{while } \lambda(x_l) < \lambda^c \text{ for all } l < k \end{aligned} \tag{5.7}$$

Naturally $\lambda(x^{\lambda^c}(X)) \gtrsim \lambda^c$, but there are many other collective variables (CVs) which can characterize this crossing point. Let us call these coordinates $\Psi_1$, $\Psi_2$, …, $\Psi_N$. For instance, if $\lambda(x)$ is the bond length between two atoms, which needs to be broken to establish the reaction, $\Psi_1(x)$ could be related to the relative position of a catalyst, $\Psi_2(x)$ a coordinate describing the solvent structure etc. For a set of $N$ collective variables in addition to $\lambda(x)$ we denote $\Psi^N(x) = \{\Psi_1(x), \Psi_2(x), \ldots, \Psi_N(x)\}$ as the vector describing the additional collective variables. Hence, whereas $\lambda(x^{\lambda^c}(X))$ describes the interface that is being crossed, $\Psi^N(x^{\lambda^c}(X))$ describes the position within this surface where the crossing takes place. We will therefore call $\Psi^N$ the orthogonal coordinates, though we should stress that this does not imply any strict orthogonality as in a Euclidean sense. In fact, $\lambda$, $\Psi_1$, $\Psi_2$, …, or $\Psi_N$ do not even have to have the same dimensionality; these can be a mix of distances, angles, integer values like the number of hydrogen bonds, Boolean functions, etc. Also, $\lambda(x)$ and $\Psi^N(x)$ do not necessarily have to be mutually independent. For instance, $\Psi_1(x) = (\lambda(x))^2$ would be a valid option. Of course, this $\Psi_1$ does not add any information about the system which we could not have already known from $\lambda$. However, this is a conclusion which should come out of our analysis method. Therefore, there is not a strict need to think very carefully about possible dependencies at this stage. We can choose $\Psi^N(x)$ based on our intuition; the collective variables which we think are important for the reaction.

We will consider three interfaces, the reactant interface $\lambda^A$, the crossing interface $\lambda^c >$

$\lambda^A$, and the (partial) reaction interface $\lambda^r > \lambda^c$. Considering all trajectories coming from $\lambda^A$ which cross $\lambda^c$, we can characterize "reactive" and "unreactive" trajectories up to $\lambda^r$. The reactive ones cross $\lambda^r$, the unreactive ones recross $\lambda^A$ without crossing $\lambda^r$. Naturally, if $\lambda^r = \lambda^B$ the "reactive" trajectories are then fully reactive, but for $\lambda^r < \lambda^B$ we get useful information about the reaction mechanism at intermediate stages of the reaction, and probably better statistics since crossing $\lambda^r < \lambda^B$ is less rare than crossing $\lambda^B$.

In the following methodology both $\lambda^c$ and $\lambda^r$ can be shifted to the desired region at the reaction barrier. As explained below, we can use the output of standard TIS, RETIS, or FFS simulations to extract a statistically representative subset of trajectories that cross $\lambda^c$. This subset can then be used to analyze the first crossing points in CV space: $\Psi_1(x^{\lambda^c}), \Psi_2(x^{\lambda^c}), \ldots$.

By constructing a grid in the collective variable space $\Psi^N$, we can define bins covering the full accessible surface of the $\lambda^c$ interface. Let $q$ be the index of these bins. Then, of all trajectories crossing $\lambda^c$ let $t_q$ be the fraction of trajectories passing through bin $q$ in the $\lambda^c$ surface, $r_q$ the fraction of trajectories passing through bin $q$ *and* cross $\lambda^r$, and $u_q$ the fraction of trajectories passing through bin $q$ but do *not* reach $\lambda^r$ (see figure 5.1).

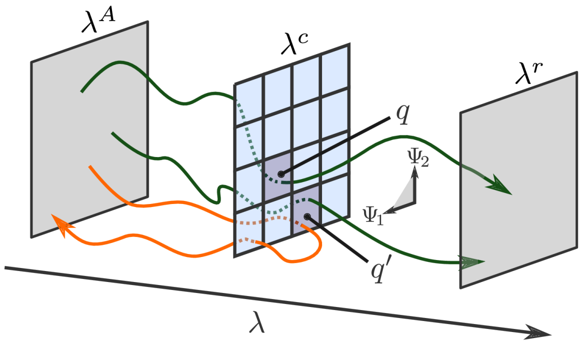

**Figure 5.1:** (Color online). Visualization of reactive and unreactive trajectories passing through bins as defined by two orthogonal CVs $\Psi_1$ and $\Psi_2$. The green trajectories are reactive up to $\lambda^r$ while the orange trajectory is unreactive. If we would only base our analysis on these three trajectories we would have $t_q = 1/3, t_{q'} = 2/3$ and $t_{q''} = 0$ for any other bin $q''$. In addition, the reactive and unreactive distributions for bins $q, q'$ would be $r_q = 1/3$, $u_q = 0$ and $r_{q'} = u_{q'} = 1/3$.

We can write down following relations

$$\begin{aligned}
t_q = u_q + r_q, \quad \sum_q t_q = 1, \\
\sum_q r_q = \mathcal{P}_A(\lambda^r|\lambda^c), \quad \sum_q u_q = 1 - \mathcal{P}_A(\lambda^r|\lambda^c)
\end{aligned} \tag{5.8}$$

Depending on the CVs and grid spacing we will get different fractions of reactive and unreactive paths in each bin. If we would be able to partition the first crossing points such that $r_q/t_q = 1$ or $r_q = 0$ for each bin, the predictive ability is optimal; each time that $\lambda^c$ is crossed for the first time, we check through which bin it passes and, then, we would be able to say whether it will cross $\lambda^r$ or not (assuming that there is no problem with the accuracy of our beforehand estimated distributions $r$ and $u$). In practice this might not be possible, either because the dynamics is stochastic or because it turns out to be too difficult to find the right CVs. In that case each bin $q$ can have any fractional value between zero and one for the reactive ratio $r_q/t_q$. The overall measure of predictive power, that can be obtained from the orthogonal coordinates, must then be a weighted average of $r_q/t_q$ over $q$. This measure should be high if there are many bins with $r_q/t_q = 1$. However, if only a very small fraction of the reactive trajectories move through bin $q$, this will not have a large impact on the overall predictive power. Therefore, we introduce a measure $\mathcal{T}$ for the CVs regarding their predictive ability which is a weighted average of $r_q/t_q$ where each bin is weighted with the fraction of reactive trajectories passing through $q$:

$$\begin{aligned}
\mathcal{T} &\equiv \sum_q \left( \frac{r_q}{\sum_v r_v} \right) \frac{r_q}{t_q} = \frac{1}{\mathcal{P}_A(\lambda^r|\lambda^c)} \sum_q \frac{r_q^2}{t_q} \\
&= \frac{1}{\mathcal{P}_A(\lambda^r|\lambda^c)} \sum_q \frac{r_q(t_q - u_q)}{t_q} \\
&= \frac{1}{\mathcal{P}_A(\lambda^r|\lambda^c)} \sum_q r_q - \frac{1}{\mathcal{P}_A(\lambda^r|\lambda^c)} \sum_q \frac{r_q u_q}{t_q} \\
&= 1 - \frac{1}{\mathcal{P}_A(\lambda^r|\lambda^c)} \sum_q \frac{r_q u_q}{t_q} \equiv 1 - \mathcal{S}
\end{aligned} \tag{5.9}$$

In continuous space, $S$ is the overlap integral of the reactive and unreactive distributions.

$$\begin{aligned}
&\mathcal{S}_A^{\lambda^c,\lambda^r}[\Psi^N] = \\
&\frac{1}{\mathcal{P}_A(\lambda^r|\lambda^c)} \int \left( \frac{r^{\lambda^c,\lambda^r}(\Psi^N) u^{\lambda^c,\lambda^r}(\Psi^N)}{t^{\lambda^c}(\Psi^N)} \right) \mathrm{d}\Psi^N
\end{aligned} \tag{5.10}$$

The overlap $\mathcal{S}_A^{\lambda^c,\lambda^r}$ will depend on the selection of CVs which are functions of phase space $x$. Hence, $\mathcal{S}_A^{\lambda^c,\lambda^r}$ is a functional of $\Psi^N(x)$. The highest possible predictive ability is obtained by finding the collective variables that minimize the overlap

$$\mathcal{S}_{A,0}^{\lambda^c,\lambda^r} = \frac{1}{\mathcal{P}_A(\lambda^r|\lambda^c)} \times \min_{\Psi^N} \left[ \int \left( \frac{r^{\lambda^c,\lambda^r}(\Psi^N) u^{\lambda^c,\lambda^r}(\Psi^N)}{t^{\lambda^c}(\Psi^N)} \right) \mathrm{d}\Psi^N \right] \tag{5.11}$$

and we call the corresponding collective variables $\Psi^N_{\text{min}}$

$$\mathcal{S}_{A}^{\lambda^c,\lambda^r}[\Psi^N_{\text{min}}] = \mathcal{S}_{A,0}^{\lambda^c,\lambda^r} \tag{5.12}$$

The $\Psi^N_{\text{min}}$ variables are in general not unique. For instance, if $\Psi_1(x)$ is a distance between two atoms, we could as well have taken the squared distance. Similarly, we could add or remove CVs to total set of CVs which have no correlation with reactivity. These operations will not change the overlap value. However, since our goal is to gain insight and to provide inspiration how to steer chemical reactions, the ideal set of orthogonal coordinates are those that minimize $\mathcal{S}_A^{\lambda^c,\lambda^r}$ *and* are also intuitive; e.g. based on known concepts such as number of hydrogen bonds, radii of gyration, nucleus size etc.

In the case that the CVs do not correlate with reactivity: $P_A(\lambda^r|\lambda^c,\Psi^N) = P_A(\lambda^r|\lambda^c)$. In other words, the chance to cross $\lambda^r$ after crossing $\lambda^c$ is independent of where the first crossing with $\lambda^c$ takes place in the $\Psi^N$ space. This might either indicate that the CVs were badly chosen or because the $\lambda^c$ surface is an iso-committor surface with respect to $\lambda^r$. The former implies that these specific CVs do not improve predictivity, while the latter implies that there simply are no CVs which potentially could improve the predictive power. For both cases, the absence of correlation implies that $r^{\lambda^c,\lambda^r}(\Psi^N) = \mathcal{P}_A(\lambda^r|\lambda^c)t^{\lambda^c}(\Psi^N)$, $u^{\lambda^c,\lambda^r}(\Psi^N) = [1-\mathcal{P}_A(\lambda^r|\lambda^c)]\, t^{\lambda^c}(\Psi^N)$. Substitution in equation 5.10 gives $\mathcal{S}_A^{\lambda^c,\lambda^r}[\Psi^N] = 1 - \mathcal{P}_A(\lambda^r|\lambda^c)$ and $\mathcal{T}_A^{\lambda^c,\lambda^r} = \mathcal{P}_A(\lambda^r|\lambda^c)$. In other words, $\Psi^N$ does not provide more information which can help us to tell whether $\lambda^r$ will be crossed or not. Based on the fact that we observe an effective positive crossing with $\lambda^c$, we know already that the chance of a (partial) reaction is $\mathcal{P}_A(\lambda^r|\lambda^c)$. Any knowledge about the orthogonal space expressed in the CVs $\Psi^N$ does not increase the quality of our predictions. Of course, if $\lambda^c$ is sufficiently beyond the transition state $\mathcal{P}_A(\lambda^r|\lambda^c) = 1$. Hence, we can still have a high predictive power. However, $\Psi^N$ does not improve it and $\mathcal{T}_A^{\lambda^c,\lambda^r}/\mathcal{P}_A(\lambda^r|\lambda^c)$ will be equal to one. Therefore, $\mathcal{T}_A^{\lambda^c,\lambda^r}$ is a useful measure of predictive capacity using all information (both $\lambda^c$ and $\Psi^N$) while $\mathcal{T}_A^{\lambda^c,\lambda^r}/\mathcal{P}_A(\lambda^r|\lambda^c)$ is a measure of the enhancement of predictive capacity due to the information of the selected orthogonal coordinates. Note that $\mathcal{T}_A^{\lambda^c,\lambda^r} \leq 1$ and $\mathcal{T}_A^{\lambda^c,\lambda^r}/\mathcal{P}_A(\lambda^r|\lambda^c) \geq 1$, which basically means that predictions can never be more than 100% correct and additional information on $\Psi^N$ can never be harmful for the predictive power.

Since, the path sampling data allow computing the overlap for different values of $\lambda^c$ and $\lambda^r$, these functions can be plotted for the full range, $\lambda^A \leq \lambda^c < \lambda^B$ and $\lambda^c \leq \lambda^r < \lambda^B$, in order to provide information about the predictive power of the CVs $\Psi^N$ at each stage of the reaction. Numerical examples showing such plots are given in Section 5.4.

## 5.3 Path Reweighing

In this section we will show how the results from TIS, FFS, or RETIS can be used to compute $\mathcal{S}_A^{\lambda^c,\lambda^r}[\Psi^N]$ for a predefined set of CVs. As mentioned above, these path sampling methods for computing reaction rates consist of a series of simulations. Each simulation samples a so-called path ensemble. The $[i^+]$ path ensemble consists of trajectories that start at $\lambda^A$, cross $\lambda_i$ at least once, and then might end at either $\lambda^A$ or $\lambda^B$. In TIS, RETIS, and FFS different path simulations sample the different ensembles $[0^+], [1^+], \dots [(M-1)^+]$. In addition, TIS and FFS also require a short MD simulation initiated from the reactant state while RETIS employs an extra path ensemble $[0^-]$. These will not be part of our analysis and in the following, when referring to the $i$-th simulation, we mean the simulation exploring the $[i^+]$ path ensemble.

Hence, from the trajectories generated in the $i$-th path ensemble, we can in principle straightforwardly determine $\mathcal{S}_A^{\lambda^c,\lambda^r}[\Psi^N]$ for $\lambda^c = \lambda_i$. We simple gather the effective crossing points with $\lambda_i$ and from these we can construct histograms for $t^{\lambda^c}$, $r^{\lambda^c,\lambda^r}$, and $u^{\lambda^c,\lambda^r}$ in the $\Psi^N$ space choosing appropriate bin widths, and by checking whether the trajectories cross $\lambda^r$ or not. Once the histograms are constructed, integrations of equation 5.10 can be carried out to obtain $\mathcal{S}_A^{\lambda^c,\lambda^r}$ and $\mathcal{T}_A^{\lambda^c,\lambda^r}$.

However, we would like to determine $\mathcal{S}_A^{\lambda^c,\lambda^r}[\Psi^N]$ or $\mathcal{T}_A^{\lambda^c,\lambda^r}[\Psi^N]$ on the full range and not restrict $\lambda^c$ to any of the TIS interfaces. In addition, we would also like to combine all data of the different path simulations to reduce statistical errors, especially if crossing $\lambda^r$ from $\lambda^c$ is a rare event. We can achieve this by path reweighting [23] based on the weighted histogram analysis method (WHAM) [24–26].

For convenience, we introduce following notation for the multidimensional Dirac delta function in CV space

$$\delta^{\lambda^c}(\Psi'^N, X) \equiv \prod_{m=1}^{N} \delta(\Psi_m(x^{\lambda^c}(X)) - \Psi'_m) \tag{5.13}$$

Now, suppose that $\lambda^c = \lambda_i$ and $\lambda^r = \lambda_j$ are both identical to one of TIS interfaces. Then we can write for $r^{\lambda_i,\lambda_j}$:

$$\begin{aligned} r^{\lambda_i,\lambda_j}(\Psi^N) &= \Big\langle h_j(X)\delta^{\lambda_i}(\Psi^N, X)\Big\rangle_{\varrho_i} \\ &= \frac{\int \varrho_i(X) h_j(X)\delta^{\lambda_i}(\Psi^N, X)\mathcal{D}X}{\int \varrho_i(X)\mathcal{D}X} \end{aligned} \tag{5.14}$$

Then, using that for $j > i$: $h_i(X)h_j(X) = h_j(X)$ or $\varrho_i(X)h_j(X) = \varrho_j(X)$, we can rewrite the above expression to get an ensemble average in $[j^+]$ ensemble.

$$\begin{aligned}
&r^{\lambda_i,\lambda_j}(\Psi^N) = \\
&\left(\frac{\int \varrho_j(X)\delta^{\lambda_i}(\Psi^N, X)\mathcal{D}X}{\int \varrho_j(X)\mathcal{D}X}\right)\left(\frac{\int \varrho_i(X)h_j(X)\mathcal{D}X}{\int \varrho_i(X)\mathcal{D}X}\right) \\
&= \left\langle \delta^{\lambda_i}(\Psi^N, X)\right\rangle_{\varrho_j} \mathcal{P}_A(\lambda_j|\lambda_i) \qquad (5.15)
\end{aligned}$$

Here, $\mathcal{P}_A(\lambda_j|\lambda_i)$ is a known result from the interface path sampling simulation since the computation of the full crossing probability $\mathcal{P}_A(\lambda|\lambda_0)$ is a central output to the TIS, FFS, and RETIS and $\mathcal{P}_A(\lambda_j|\lambda_i) = \mathcal{P}_A(\lambda_j|\lambda_0)/\mathcal{P}_A(\lambda_i|\lambda_0)$. In principle, also the data of the other path ensembles can be used to obtain $r^{\lambda_i,\lambda_j}$ since for any $k < j$:

$$r^{\lambda_i,\lambda_j}(\Psi^N) = \left\langle \delta^{\lambda_i}(\Psi^N, X)h_j(X)\right\rangle_{\varrho_k} \mathcal{P}_A(\lambda_k|\lambda_i) \qquad (5.16)$$

The ensembles $[k^+]$ with $k > j$ can by itself not be used to fully compute the $r^{\lambda_i,\lambda_j}$ distribution, but still these data can be used to reduce its statistical errors. WHAM [24–26] provides a way to take a weighted average of the distributions which have been obtained using different bias functions (also called windows). That is, for an arbitrary parameter $\xi(x)$ the most accurate distribution that can be obtained from the different biased simulations is

$$\rho(\xi) = \frac{\sum_{i=1}^{N_w} \omega_i(\xi)\rho_i^{\text{unb.}}(\xi)}{\sum_{j=1}^{N_w} \omega_j(\xi)} \qquad (5.17)$$

Here $N_w$ is the number of windows and $\rho(\xi)_i^{unb}$ is the unbiased distribution of simulation $i$. This is the distribution after proper rescaling to remove the effect bias. Further, $\omega_i$ are weights depending on $\xi$, chosen to be proportional to inverse square of the estimated error in each simulation.

As shown in the appendix, also the crossing probability itself can then be expressed using WHAM:

$$\mathcal{P}_A(\lambda|\lambda_0) = \frac{\sum_{i=0}^{K(\lambda)} n_i[\lambda]}{\sum_{j=0}^{K(\lambda)} n_j[\mathcal{P}_A(\lambda_j|\lambda_0)]^{-1}} \qquad (5.18)$$

Here $n_i[\lambda]$ is the number of trajectories in simulation $i$ having a $\lambda_{\text{max}} > \lambda$, $n_j$ is the total number of trajectories in simulation $j$, and $K(\lambda)$ is the integer which fulfills

$$K(\lambda) = \begin{cases} k & \text{if } \lambda_k < \lambda \leq \lambda_{k+1} \text{ and } \lambda < \lambda^B \\ M-1 & \text{if } \lambda > \lambda^B \end{cases} \qquad (5.19)$$

The maximum of $M-1$ is due to the fact that there is generally not a simulation that just considers the $[M^+]$ ensemble since it gives the trivial unit contribution in the product expression, equation 5.1. Equation 5.18 can be solved iteratively and is presumably somewhat more accurate than equation 5.1 since it is based on more data. If $n_j$ is equal for all simulations, then equation 5.18 is identical to the crossing probability derived by Rogal et al. [23] in a different manner. In our derivation (see appendix) we also provide two refinements of the above expression. One is standard and appears also in e.g Roux [26] and is related to the effect of correlated trajectories which might be more severe in some of the simulation than in the others. Another refinement, that is non-standard, is related to the non-negligible size of the bins in the determination of crossing probability. The use of more refined expressions is not always preferred since they rely on the facts that errors can be obtained accurately while, in practice, simulations which tend to get trapped for a long time can provide artificially low standard deviations. In the refined expression these simulations could get the highest weights and overwhelm the more converged results of the other simulations. We have therefore used the simpler expression, equation 5.18, in the remainder of this chapter.

In order to obtain our distributions $t_q^{\lambda^c}$, $r_q^{\lambda^c,\lambda^r}$, and $u_q^{\lambda^c,\lambda^r}$ we first compute the following ensemble averages $\left\langle H_{q,\lambda^c}^{[\lambda^a:\lambda^b]}\right\rangle_{\varrho_0}$ in which $H_{q,\lambda^c}^{[\lambda^a:\lambda^b]}(X)$ is 1 (otherwise 0) if and only if trajectory $X$ passes through bin $q$ on the $\lambda^c$ surface while $\lambda_{\max}(X)$ is inside the interval $[\lambda^a : \lambda^b]$. Moreover, we restrict ourselves to intervals which do not overlap with any of the TIS interfaces. In other words $\lambda^b \leq \lambda_{K(\lambda^a)+1}$. Then for any $i \leq K(\lambda^a)$:

$$\begin{aligned}
\left\langle H_{q,\lambda^c}^{[\lambda^a:\lambda^b]}\right\rangle_{\varrho_0} &= \frac{\int H_{q,\lambda^c}^{[\lambda^a:\lambda^b]}\varrho_0(X)\mathrm{d}X}{\int \varrho_0(X)\mathrm{d}X} \\
&= \frac{\int H_{q,\lambda^c}^{[\lambda^a:\lambda^b]}\varrho_i(X)\mathrm{d}X}{\int \varrho_i(X)\mathrm{d}X}\frac{\int \varrho_i(X)\mathrm{d}X}{\int \varrho_0(X)\mathrm{d}X} \\
&= \left\langle H_{q,\lambda^c}^{[\lambda^a:\lambda^b]}\right\rangle_{\varrho_i} \mathcal{P}_A(\lambda_i|\lambda_0) \qquad (5.20)
\end{aligned}$$

Here we used the relation $H_{q,\lambda^c}^{[\lambda^a:\lambda^b]}\varrho_0 = H_{q,\lambda^c}^{[\lambda^a:\lambda^b]}\varrho_i$ valid for $\lambda_i < \lambda^a$. Hence, this property can be determined using different interface ensemble simulations. As shown in the appendix, the WHAM weights which are assumed to minimize the error equals

$$\omega_i = \frac{[\mathcal{P}_A(\lambda_i|\lambda_0)]^{-1}}{\sum_{j=0}^{K(\lambda^a)}[\mathcal{P}_A(\lambda_j|\lambda_0)]^{-1}} \qquad (5.21)$$

This implies that the WHAM expression equals

$$\left\langle H_{q,\lambda^c}^{[\lambda^a:\lambda^b]}\right\rangle_{\varrho_0} = \frac{\sum_{i=0}^{K(\lambda^a)} n_i(q,\lambda^c;[\lambda^a:\lambda^b])}{\sum_{j=0}^{K(\lambda^a)} n_j[\mathcal{P}_A(\lambda_j|\lambda_0)]^{-1}} \qquad (5.22)$$

where $n_i(q, \lambda^c; [\lambda^a : \lambda^b])$ is the number of trajectories in simulation $i$ moving through bin $q$ at its first crossing with $\lambda^c$ and having $\lambda_{\max}$ in the interval $[\lambda^a : \lambda^b]$.

Our distributions can then be constructed from these since

$$\begin{aligned}
R_q^{\lambda^c,\lambda^r} &= \left\langle H_{q,\lambda^c}^{[\lambda^r:\lambda_{K(\lambda^r)+1}]} \right\rangle_{\varrho_0} + \sum_{k=K(\lambda^r)+1}^{M} \left\langle H_{q,\lambda^c}^{[\lambda_k:\lambda_{k+1}]} \right\rangle_{\varrho_0} \\
U_q^{\lambda^c,\lambda^r} &= \left\langle H_{q,\lambda^c}^{[\lambda^c:\lambda^r]} \right\rangle_{\varrho_0} \text{ if } \lambda^r < \lambda_{K(\lambda^c)+1} \text{ or} \\
&= \left\langle H_{q,\lambda^c}^{[\lambda^c:\lambda_{K(\lambda^c)+1}]} \right\rangle_{\varrho_0} + \sum_{k=K(\lambda^c)+1}^{K(\lambda^r)} \left\langle H_{q,\lambda^c}^{[\lambda_k:\lambda_{k+1}]} \right\rangle_{\varrho_0} \\
&+ \left\langle H_{q,\lambda^c}^{[\lambda_{K(\lambda^r)}:\lambda_r]} \right\rangle_{\varrho_0} \text{ if } \lambda^r > \lambda_{K(\lambda^c)+1}
\end{aligned} \tag{5.23}$$

where $\lambda_{M+1} = \infty$. Now, by rescaling we obtain the actual distributions

$$r_q^{\lambda^c,\lambda^r} = \frac{R_q^{\lambda^c,\lambda^r}}{\mathcal{P}_A(\lambda^c|\lambda_0)}, \quad u_q^{\lambda^c,\lambda^r} = \frac{U_q^{\lambda^c,\lambda^r}}{\mathcal{P}_A(\lambda^c|\lambda_0)} \tag{5.24}$$

## 5.4 Numerical Results

In this section we will give a detailed description of the implementation for calculating the crossing probability and distribution functions. We will also exemplify the method by applying it to three systems we have studied with RETIS simulations.

### 5.4.1 Implementation

#### The Crossing Probability

In order to obtain the distribution functions using WHAM we need, first of all, to obtain the crossing probability. This can be done using the product expression, equation 5.1, or the more accurate expression based on WHAM, equation 5.18. We will discuss the last one. The first step is to obtain the values of the crossing probability at the TIS interfaces. Setting $\mathcal{P}_A(\lambda_0|\lambda_0) = 1$ gives directly

$$\mathcal{P}_A(\lambda_1|\lambda_0) = \frac{n_0(\lambda_1)}{n_0} \tag{5.25}$$

or simply the number of trajectories in simulation 0 crossing $\lambda_1$ divided by the total number of trajectories in simulation 0. The next interface gives

$$\mathcal{P}_A(\lambda_2|\lambda_0) = \frac{n_0(\lambda_2) + n_1(\lambda_2)}{n_0 + n_1 \left[\mathcal{P}_A(\lambda_1|\lambda_0)\right]^{-1}} \tag{5.26}$$

and so we can continue determining $\mathcal{P}_A(\lambda_3|\lambda_0)$, $\mathcal{P}_A(\lambda_4|\lambda_0)$, ..., $\mathcal{P}_A(\lambda_M|\lambda_0)$. For convenience we define

$$Q_k \equiv \frac{1}{\sum_{j=0}^{k} n_j \left[\mathcal{P}_A(\lambda_j|\lambda_0)\right]^{-1}} \tag{5.27}$$

and the crossing probability for any continuous value $\lambda$ is then obtained by a simple summation which includes all trajectories $X$ in all path sampling data of ensembles $i = 0, 1, \ldots, M-1$

$$\begin{aligned} \mathcal{P}_A(\lambda|\lambda_0) &= Q_{K(\lambda)} \sum_{i=0}^{K(\lambda)} n_i[\lambda] \\ &= Q_{K(\lambda)} \sum_{i=0}^{M-1} n_i[\lambda]\theta(\lambda-\lambda_i) \\ &= Q_{K(\lambda)} \sum_{i=0}^{M-1} \sum_{X\in[i^+]} \theta(\lambda_{\max}(X)-\lambda)\theta(\lambda-\lambda_i) \end{aligned} \tag{5.28}$$

with $\theta(\cdot)$ being the Heaviside step function.

In an actual computer algorithm, $\mathcal{P}_A(\lambda|\lambda_0)$ is computed using a small step-size along the $\lambda$-parameter which define a fine grid of sub-intervals. Let $v(\alpha)$ be the vector for determining $\mathcal{P}_A(\lambda|\lambda_0)$ on this fine grid such that $\alpha$ is an index of the sub-interface $\lambda^\alpha$ and $v(\alpha) = \mathcal{P}_A(\lambda^\alpha|\lambda_0)$ after completion of the algorithm. We can then determine the full vector $v$ as follows:

1. Set all entries of $v(\alpha)$ equal to 0: $v(\alpha) = 0$.
2. Loop over all data sets corresponding to the path ensembles $i = 0, 1, \ldots, M-1$, and for each trajectory $X$ in data set $i$:
    - 2.1. Determine $\lambda_{\max}(X)$.
    - 2.2. For each $\alpha$ where $\lambda_i \leq \lambda^\alpha < \lambda_{\max}(X)$, increment $v(\alpha)$: $v(\alpha) = v(\alpha) + 1$
3. For each $\alpha$ determine $K(\alpha)$ and $Q_{K(\alpha)}$ and multiply this with the vector entry: $v(\alpha) = v(\alpha) \times Q_{K(\alpha)}$.

### Probability Distribution Functions

We can also determine the probability distribution function $u_q^{\lambda^c,\lambda^r}$, $r_q^{\lambda^c,\lambda^r}$ based on equations 5.22-5.24 using a single loop over all trajectories. Substituting equation 5.27 into equation 5.22 yields

$$\begin{aligned}\left\langle H_{q,\lambda^c}^{[\lambda^a:\lambda^b]}\right\rangle_{\varrho_0} &= Q_{K(\lambda^a)}\sum_{i=0}^{K(\lambda^a)} n_i(q,\lambda^c;[\lambda^a:\lambda^b]) \\ &= Q_{K(\lambda^a)}\sum_{i=0}^{M-1} n_i(q,\lambda^c;[\lambda^a:\lambda^b]) \\ &= \sum_{i=0}^{M-1}\sum_{X\in[i^+]} Q_{K(\lambda_{\max})}\delta_{q,\lambda^c} \\ &\times\ \theta(\lambda^a-\lambda_{\max})\theta(\lambda_{\max}-\lambda^b) \qquad (5.29)\end{aligned}$$

where $\delta_{q,\lambda^c}$ is 1 (otherwise zero) whenever $X$ has a first crossing through bin $q$ at the $\lambda^c$ surface. In the second equation we used the fact that we only consider intervals $[\lambda^a:\lambda^b]$ that are not overlapping with the TIS interfaces. This implies that $\lambda^b < \lambda_{K(\lambda^a)+1}$ and, hence, $n_i(q,\lambda^c;[\lambda^a:\lambda^b]) = 0$ for any $i \geq K(\lambda^a)+1$. In the third expression we use that whenever $\lambda_{\max}(X)$ is within this interval $[\lambda^a:\lambda^b]$, we must have $K(\lambda^a) = K(\lambda_{\max})$. Equation 5.29 shows that $\left\langle H_{q,\lambda^c}^{[\lambda^a:\lambda^b]}\right\rangle_{\varrho_0}$ can be expressed as a sum over all trajectories without considering the actual simulation $i$ it was taken from. The values to be summed are either zero or $Q_{K(\lambda_{\max})}$. A non-zero contribution can only occur whenever $\lambda_{\max}$ is within the interval $[\lambda^a:\lambda^b]$. Now let us consider equations 5.23. To calculate $R_q^{\lambda^c,\lambda^r}$ and $U_q^{\lambda^c,\lambda^r}$ we need to add $\left\langle H_{q,\lambda^c}^{[\lambda^a:\lambda^b]}\right\rangle_{\varrho_0}$ for different intervals and since these intervals are not overlapping, each $X$ can only give a contribution 0 or $Q_{K(\lambda_{\max})}$ to the total sum as well. The non-zero contribution occurs whenever there is a first crossing through bin $q$ and $\lambda_{\max}$ is within $[\lambda^c:\lambda^r]$ for $U_q^{\lambda^c,\lambda^r}$ and whenever $\lambda_{\max}$ is larger than $\lambda^r$ for $R_q^{\lambda^c,\lambda^r}$. Now, let $M_u(q,\alpha,\beta)$ and $M_r(q,\alpha,\beta)$ be the matrices used to construct the $u_q^{\lambda^\alpha,\lambda^\beta}$ and $r_q^{\lambda^\alpha,\lambda^\beta}$ distributions, respectively, where $\alpha,\beta$ are indices of the fine grid along $\lambda$. The computational algorithm is then as follows:

1. Set all entries of matrices $M_u(q,\alpha,\beta)$ and $M_r(q,\alpha,\beta)$ equal to 0.
2. Loop over all data sets corresponding to path ensembles $i = 0,1,\ldots M-1$, and for each trajectory $X$ in data set $i$:
    - 2.1. Determine $\lambda_{\max}$ and $Q_{K(\lambda_{\max})}$.
    - 2.2. For each $\alpha$ such that $\lambda^\alpha < \lambda_{\max}$:
        - Determine $x^{\lambda^\alpha}$ and the corresponding bin $q$.
        - For each $\beta$ such that $\lambda^\beta > \lambda_{\max}$, add $Q_{K(\lambda_{\max})}$ to the entries of $M_u(q,\alpha,\beta)$: $M_u(q,\alpha,\beta) = M_u(q,\alpha,\beta) + Q_{K(\lambda_{\max})}$.

  - For each $\beta$ such that $\lambda^{\beta} \leq \lambda_{\max}$, add $Q_{K(\lambda_{\max})}$ to all entries of $M_r(q, \alpha.\beta)$: $M_r(q, \alpha, \beta) = M_r(q, \alpha, \beta) + Q_{K(\lambda_{\max})}$.

3. For each $\alpha$, apply for all $\beta$ and $q$ the normalizations $M_r(q, \alpha, \beta) = M_r(q, \alpha, \beta)/v(\alpha)$ and $M_u(q, \alpha, \beta) = M_u(q, \alpha, \beta)/v(\alpha)$. The normalized matrices $M_r$ and $M_u$ are now estimates of the distributions $r_q^{\lambda^c,\lambda^r}$ and $u_q^{\lambda^c,\lambda^r}$, respectively.

The fine grid along $\lambda$ does not have to be commensurate with the TIS interfaces. The accuracy is not affected by the spacing between the sub-interfaces unlike the binning in the orthogonal directions; The bins $q$ have to be sufficiently large in order to determine the path density going through it, while still be sufficiently small enough to get enough resolution in order to discriminate between $r_q$ and $u_q$.

### 5.4.2 Numerical Example 1: 1D Double Well Potential

The 1D double well potential, $V(r) = r^4 - 2r^2$, models the transition for a single particle between two stable states (located at $r \pm 1$) separated by a barrier (at $r = 0$) [21]. The progress coordinate is in this case given by the position of the particle in the potential: $\lambda = r$. We have investigated the transition between the two stable states using RETIS simulations under Langevin dynamics with a friction coefficient $\gamma = 0.3$ and a reduced temperature of 0.07 as described in Ref. 21.

Two additional collective variables have been considered for our analysis: (1) the velocity of the order parameter $v = \mathrm{d}\lambda/\mathrm{d}t$ and (2) the random Langevin force averaged over 9 steps (labeled “9rf”) after the crossing. The use of the second parameter might be viewed as a not completely "fair" way to improve predictions since it assumes that, after crossing $\lambda^c$, one already knows which random numbers will be generated for the stochastic force. Still, it is a CV that we can use in a computer experiment in order to measure the balance of initial conditions at the crossing before the reaction takes place and the stochastic contributions during the course of the reaction. The use of velocity is also not a common parameter in reaction coordinate analysis studies. Notably exceptions are Ref. 27, 28 in which not the configurational committor but the transmission coefficient selected to choose the reaction coordinates.

The first collective variable, $v$, is expected to improve the predictive capacity for small values of $\gamma$ when the dynamics is largely deterministic, while the second, “9rf”, may improve the predictive capacity for stochastic dynamics resulting from a large friction coefficient $\gamma$. In figure 5.2, we show the crossing probability and the predictive capacities for the three combinations of collective variables ($\{v\}$, $\{9\text{rf}\}$, $\{v, 9\text{rf}\}$). These results show that the predictive capacity is largely improved by inclusion of the collective variable $v$, but only minimally with the inclusion of 9rf. This shows that the chance for a barrier crossing is much more determined by the right initial conditions than by a rare

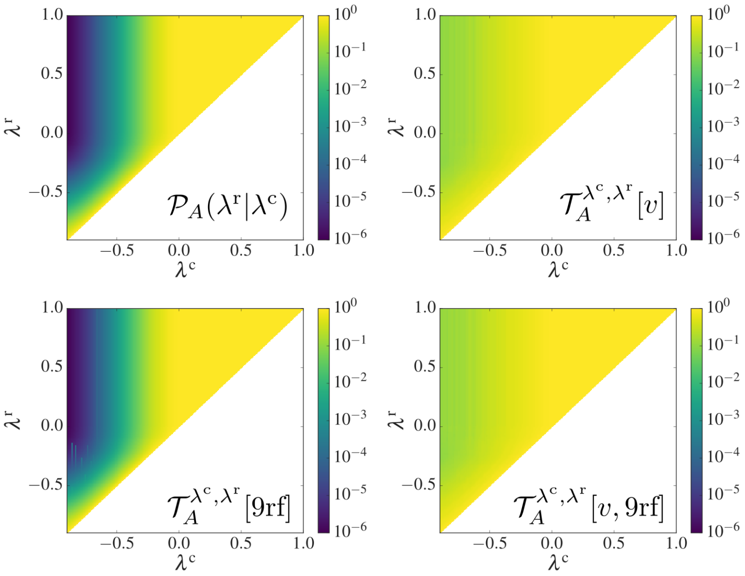

**Figure 5.2:** (Color online.) The crossing probability, $\mathcal{P}_A(\lambda^r|\lambda^c)$, and the predictive capacities, $\mathcal{T}_A^{\lambda^c,\lambda^r}$, for the 1D double well potential: (top left) the crossing probability, (top right) the predictive capacity using the velocity ($v$) of the progress coordinate as the collective variable, (bottom left) the predictive capacity using the random Langevin force averaged over 9 steps ("9rf") as the collective variable, (bottom right) the predictive capacity using both $v$ and 9rf as collective variables. We used 200 sub-interfaces both for $\lambda^r$ and $\lambda^c$. The histograms in the $\Psi^N$ space were constructed using 20 bins for $-2 < v < 2$ and 20 bins for $-3 < \mathrm{9rf} < 3$.

sequence of random kicks during the barrier crossing process. This is also the reason that FFS is not able to predict the crossing rate in an adequate manner [21].

A closer inspection (see figure 5.3) shows that the predictive capacities can be increased by several orders of magnitude due to the knowledge of $v$. The use of 9rf as CV only improves the predictions by 4% as is shown in the inset of the top panel.

### 5.4.3 Numerical Example 2: Ion Transfer Model in a Solvent

This example models the ion transfer reaction $\mathrm{Ax} + \mathrm{A} \rightarrow \mathrm{A} + \mathrm{Ax}$ where an ion, x is transferred between two molecules of the same type, A. The reaction takes place in a solvent (molecules of type B) which may reduce the barrier due to a cooperative effect. For the detailed description of the potential and the interactions, please see Ref. 29.

The ion is initially bound to one of the A molecules (labeled "$\mathrm{A_1}$") and it is transferred to the other (labeled $\mathrm{A_2}$) over the course of the reaction. The progress coordinate, $\lambda$, is

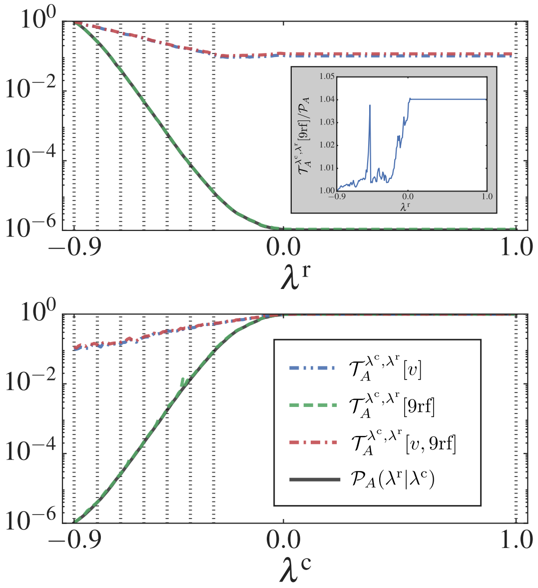

**Figure 5.3:** (Color online.) The crossing probability, $\mathcal{P}_A(\lambda^r|\lambda^c)$, and the predictive capacities, $\mathcal{T}_A^{\lambda^c,\lambda^r}$, for the double well potential at (top) $\lambda^c = -0.9$ and (bottom) $\lambda^r = 1$. The position of the interfaces used in the RETIS simulations are indicated with dotted vertical lines. In both cases we find that $\mathcal{T}_A^{\lambda^c,\lambda^r}[v, 9\text{rf}] > \mathcal{T}_A^{\lambda^c,\lambda^r}[v] >> \mathcal{P}_A(\lambda^r|\lambda^c)$ and $\mathcal{T}_A^{\lambda^c,\lambda^r}[9\text{rf}] > \mathcal{P}_A(\lambda^r|\lambda^c)$ and in the inset in the top figure we show the enhancement of the predictive capacity, $\mathcal{T}_A^{\lambda^c,\lambda^r}[9\text{rf}]/\mathcal{P}_A(\lambda^r|\lambda^c)$, when using 9rf alone as the collective variable.

defined using the distance, $r_{\mathrm{x,A_2}}$, between x and A$_2$:

$$\lambda = -r_{\mathrm{x,A_2}} \tag{5.30}$$

where the minus sign ensures that the progress coordinate changes from a low value to a high value while the ion transfer advances. The reactant state is defined by $\lambda^A = -0.7$ and the product state by $\lambda^B - 0.4$.

For our analysis we have defined two additional collective variables: (1) the velocity, $v$, of the progress coordinate ($v = \mathrm{d}\lambda/\mathrm{d}t$), and (2) the coordination number, $CN$, for solvent molecules surrounding the ion, defined by

$$CN = \sum_{j \in \{\text{type B}\}} \frac{1}{1 + \exp\left[N_{\mathrm{d}}\left(r_{\mathrm{x},j} - R_{\mathrm{coop}}\right)\right]} \tag{5.31}$$

where $r_{\mathrm{x},j}$ is the distance between the ion and solvent molecule $j$ and $R_{\mathrm{coop}}$ and $N_{\mathrm{d}}$ are parameters of the potential [29]. Like in the previous example, we expect the velocity $v$

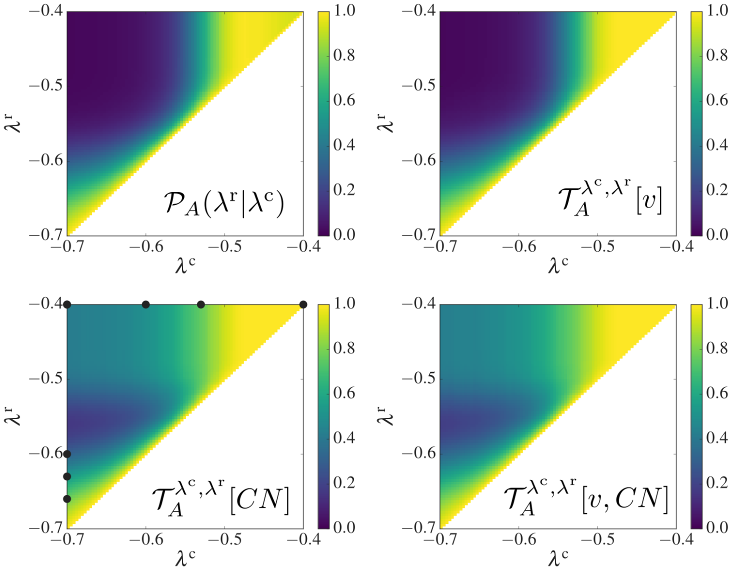

**Figure 5.4:** (Color online.) The crossing probability, $\mathcal{P}_A(\lambda^r|\lambda^c)$, and the predictive capacities, $\mathcal{T}_A^{\lambda^c,\lambda^r}$, for the ion transfer potential: the crossing probability (top left), the predictive capacity using the velocity ($v$) of the progress coordinate as the collective variable (top right), the predictive capacity using the coordination number ($CN$) as the collective variable (bottom left), the predictive capacity using both $v$ and $CN$ as collective variables (bottom right). We used 85 subinterfaces both for $\lambda^r$ and $\lambda^c$. The histograms in the $\Psi^N$ space were constructed using 20 bins for $0 < CN < 3$ and 20 bins for $-45 < v < 25$. The circles placed on the $\lambda^r$ and $\lambda^c$ axes in the bottom left figure indicate points where we have obtained the distributions in the $CN$ space, shown in figure 5.5 and 5.6

to be important if the crossing process is largely non-stochastic. This would be the case if the typical collision time with solvent molecules is larger than the time required to cross the reaction barrier. For dense systems, we expect that the second collective variable will be more important as it's directly linked to the height of the barrier [29].

In figure 5.4 we show the crossing probability and the predictive capacity for the three combinations of collective variables ($\{v\}, \{CN\}, \{v, CN\}$) using results from a RETIS simulation carried out as described in Ref. 29. In this case, we see that both variables improve the predictive capacity. However, the coordination number improves the predictive capacity more than the velocity of the progress coordinate. The distributions $t^{\lambda^c,\lambda^r}(CN)$, $r^{\lambda^c,\lambda^r}(CN)$, and $u^{\lambda^c,\lambda^r}(CN)$ for some of the $\lambda^c, \lambda^r$ values are shown in figures 5.5 and 5.6. Figure 5.5 shows the distributions with $\lambda^c = \lambda^A$ and different values for $\lambda^r$, while figure 5.6 shows the distributions for $\lambda^r$ fixed at $\lambda^B$ and different values for $\lambda^c$.

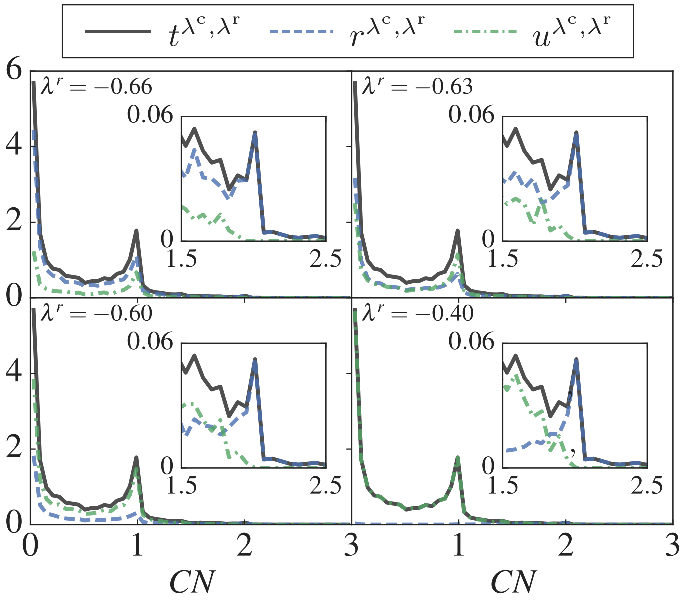

**Figure 5.5:** (Color online.) Distribution of $t^{\lambda^c,\lambda^r}$, $r^{\lambda^c,\lambda^r}$ and $u^{\lambda^c,\lambda^r}$ using the coordination number ($CN$) as the collective variable for $\lambda^c = -0.7$ and $\lambda^r = -0.66$ (top-left), $\lambda^r = -0.63$ (top-right), $\lambda^r = -0.60$ (bottom-left) and $\lambda^r = -0.4$ (bottom-right). For the analysis, we used 22 sub-interfaces both for $\lambda^r$ and $\lambda^c$, and the distributions shown here were obtained using 50 bins for $0 < CN < 3$.

The values correspond to the black dots in the left-bottom panel of figure 5.4. Figure 5.5 shows a clear cross-over for increasing $\lambda^r$. For $\lambda^r$ values close to $\lambda^c = \lambda^A$, the reactive distribution $r^{\lambda^c,\lambda^r}(CN)$ is almost identical to the total distribution $t^{\lambda^c,\lambda^r}(CN)$. However, when $\lambda^r$ is moved towards $\lambda^B$ the unreactive distribution increases at the expense of the reactive distribution. Despite, as shown by the insets, the reactive distribution is always higher at the large coordination numbers.

Figure 5.6 shows an opposite trend regarding the height of the distributions. The unreactive distribution is initially the largest but for increasing $\lambda^c$ the reactive distribution rises at the expense of $u^{\lambda^c,\lambda^r}(CN)$. At large coordination numbers, the reactive distribution is always the largest just as in figure 5.5.

Figure 5.7 shows the intersections of figure 5.4 corresponding to a fixed $\lambda^c = -0.7$ and a fixed $\lambda^r = -0.4$. The results clearly show that the coordination number is a much better indicator for the ion-transfer reaction than the velocity along the reaction coordinate $\lambda$. Still, having knowledge of both parameters will improve the predictive capacity slightly more compared to the situation in which one only knows $CN$.

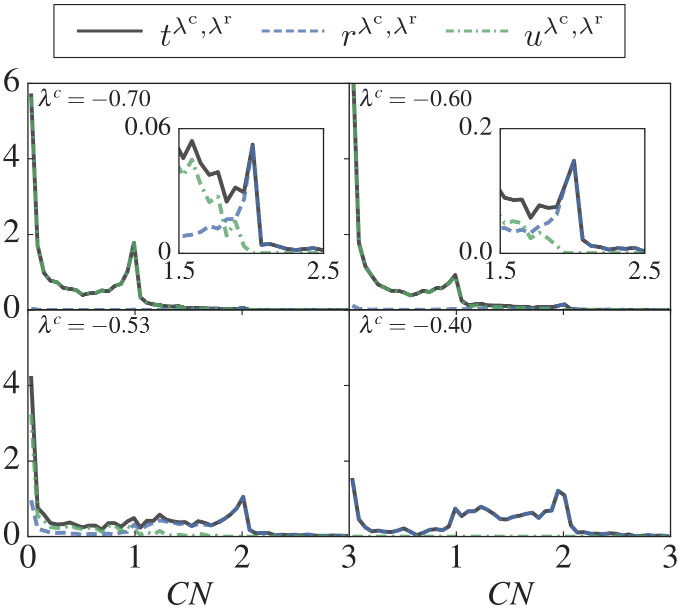

**Figure 5.6:** (Color online.) Distribution of $t^{\lambda^c,\lambda^r}$, $r^{\lambda^c,\lambda^r}$ and $u^{\lambda^c,\lambda^r}$ using the coordination number ($CN$) as the collective variable for $\lambda^r = -0.4$ and $\lambda^c = -0.70$ (top-left), $\lambda^c = -0.60$ (top-right), $\lambda^c = -0.53$ (bottom-left) and $\lambda^c = -0.40$ (bottom-right). For the analysis, we used 22 sub-interfaces both for $\lambda^r$ and $\lambda^c$, and the distributions shown here were obtained using 50 bins for $0 < CN < 3$.

### 5.4.4 Numerical Example 3: Ab Initio MD of Water Dissociation

For this example, we have performed RETIS simulations of dissociation of water at a low density. Water was modeled with the BLYP functional [30, 31] and a DZVP-MOLOPT basis set [32]. A plane-wave cut-off of 300 Ry was used and the simulations were performed at a low density with 8 water molecules in a cubic simulation box of $9.85 \times 9.85 \times 9.85$ Å$^3$. Periodic boundary conditions were employed in all directions. The DFT-based MD simulations were carried out using the CP2K program package [33] with a time step of 0.5 fs and NVE dynamics. Shooting moves were performed by randomly reselecting the velocities at the shooting point from a Maxwellian distribution corresponding to a temperature of 600 K.

The progress coordinate was defined using the distances between oxygen and hydrogen atoms. We first assign each hydrogen to the oxygen atom it is closest to. This allows us to classify molecules, e.g. as $H_2O$, $H_3O^+$ or $OH^-$, and calculate bond lengths between hydrogen and oxygen. If the system only contains $H_2O$ molecules, the progress coordinate is defined as the longest hydrogen-oxygen bond length. If the system contains $H_3O^+$ and $OH^-$ species, the order parameter is taken as the shortest distance from the oxygen

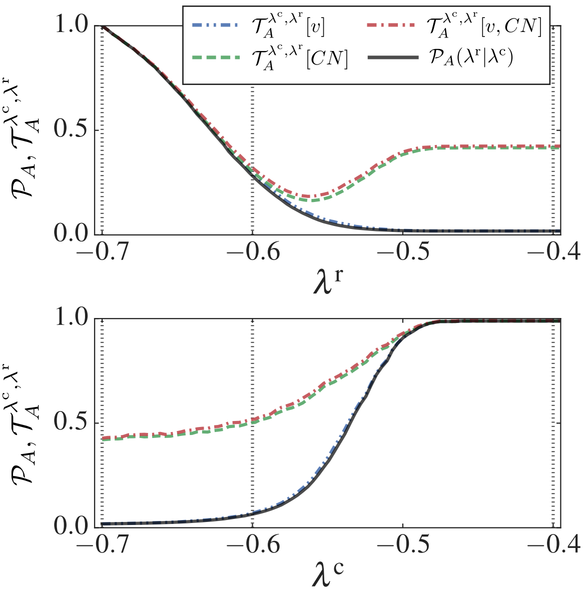

**Figure 5.7:** (Color online.) The crossing probability, $\mathcal{P}_A(\lambda^r|\lambda^c)$, and the predictive capacities, $\mathcal{T}_A^{\lambda^c,\lambda^r}$, for the ion transfer potential at (top) $\lambda^c = -0.7$ and (bottom) $\lambda^r = -0.4$. The position of the interfaces used in the RETIS simulations are indicated with dotted vertical lines.

in $OH^-$ to a hydrogen in $H_3O^+$.

For this example, we have considered one additional collective variable defined as the length, $w$, of the shortest hydrogen bond wire connecting $4$ water molecules/species where one of the species contain the oxygen atom used for the progress coordinate. Hassanali et al. [34] highlighted the importance of compression of such wires for the recombination reaction and hypothesized that a similar phenomena is likely to be the rate-limiting step for autoionization. In order to obtain the hydrogen bond wire length, we first obtained all hydrogen bonds (defined as in Ref. 35) in the system and used this to create a graph of hydrogen-bond connected water molecules. The relevant hydrogen bond wire was obtained using the following criteria: (i) The wire should contain the oxygen atom used for the order parameter (identified as explained above) when the order parameter first crossed the $1.15$ interface, (ii) the wire should contain $4$ water molecules, (iii) the wire should be the shortest of the wires where criterion (i) and (ii) is met. The length of the wire was defined as the sum of the oxygen-oxygen distances of consecutive molecules in the wire.

The results of including this additional collective variable are shown in figure 5.8. The

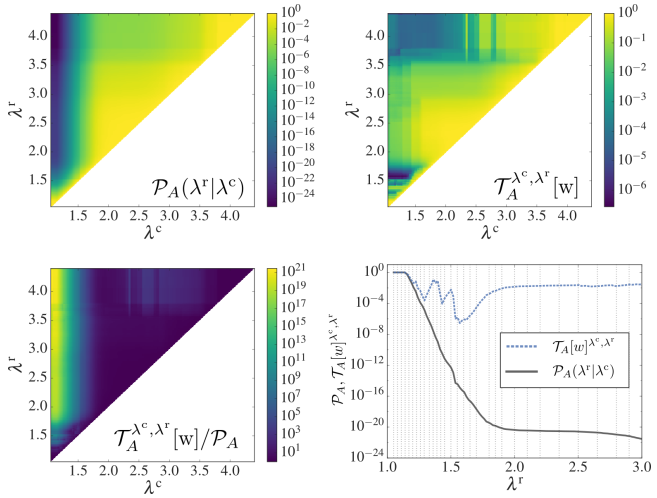

**Figure 5.8:** (Color online.) The crossing probability, $\mathcal{P}_A(\lambda^r|\lambda^c)$, and the predictive capacity, $\mathcal{T}_A^{\lambda^c,\lambda^r}$, for the ab initio water simulations: (top left) the crossing probability, (top right) the predictive capacity using the hydrogen bond wire length ($w$) the collective variable (see the main text for the definition of this quantity), (bottom left) the enhancement of the predictive capacity, $\mathcal{T}_A^{\lambda^c,\lambda^r}[w]/\mathcal{P}_A(\lambda^r|\lambda^c)$, (bottom right) the predictive capacity and crossing probability as a function of $\lambda^r$ for $\lambda^c = 1.05$ (positioned at the leftmost interface; the position of the interfaces used in the RETIS simulations are indicated with dotted vertical lines). We used 200 sub-interfaces both for $\lambda^r$ and $\lambda^c$. The histograms in the $\Psi^N$ space were constructed using 50 bins for $7 < w < 11$.

values of $\mathcal{T}_A^{\lambda^c,\lambda^r}[w]$, show that the dissociation reaction involves rare fluctuations in the hydrogen bonded network and as shown in the bottom-left and bottom-right figures, including the hydrogen bond wire length improves the predictive capacity compared by several orders of magnitude.

## 5.5 Reduction of CVs and Relation to the Isocommittor

Whenever a predictive set of CVs is obtained with a relatively low overlap value $\mathcal{S}_A^{\lambda^c,\lambda^r}[\Psi^N]$ for a certain set of interfaces $\lambda^c$, $\lambda^r$, one can attempt to reduce the number of CVs without raising the overlap value. The idea is graphically illustrated in figure 5.9 where we show how a two-dimensional CV-space can be projected on a single coordinate. In the figure the best possible one-dimensional coordinate is given as a linear combination of the previously examined coordinates $\Psi_1$ and $\Psi_2$. This approach can also be used to construct coordinates that are non-linear functions of the original CVs. However, in some cases it might be preferred to project on a more simple coordinate even if it is not the best one in terms of minimizing the overlap since the more complex functional form might be less intuitive.

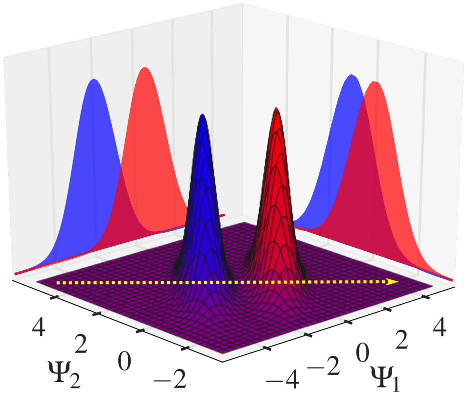

**Figure 5.9:** (Color online). Reduction of a set of CVs having a low overlap. Let red represent the distribution $r^{\lambda^c,\lambda^r}(\Psi_1,\Psi_2)$ and blue $u^{\lambda^c,\lambda^r}(\Psi_1,\Psi_2)$ where $\Psi_1,\Psi_2$ are two CVs. By selecting $\Psi_1$ as a single one-dimensional coordinate the projected distributions still show little overlap while the coordinate $\Psi_2$ is a much poorer choice since the projected distributions $r^{\lambda^c,\lambda^r}(\Psi_2)$ and $u^{\lambda^c,\lambda^r}(\Psi_2)$ will almost fully overlap. The optimal coordinate is shown by a yellow arrow and corresponds to the linear combination $c_1\Psi_1 + c_2\Psi_2$ where $c_1$ and $c_2$ are two constants.

The projection procedure can, in principle, also be used to find the committor, at least if sufficient path data is available. Suppose that we use the full phase space as orthogonal coordinates ($\Psi^N = x$) and take $\lambda^r = \lambda^B$. In that case $r^{\lambda^c,\lambda^B}(x)/t^{\lambda_i}(x) = P_B(x)$ where $P_B(x)$ is the phase space committor. For the overlap integral we get

$$\mathcal{S}_A^{\lambda^c,\lambda^B}[x] = \frac{1}{\mathcal{P}_A(\lambda^B|\lambda^c)} \int_{\lambda^c} \mathrm{d}x\, t^{\lambda^c}(x) P_B(x)(1 - P_B(x)) \tag{5.32}$$

Suppose we bin the full phase space such that the integral can be solved numerically as

$$\mathcal{S}_A^{\lambda^c,\lambda^B}[x] = \frac{\mathrm{d}x}{\mathcal{P}_A(\lambda^B|\lambda^c)} \sum_q s(x_q) \tag{5.33}$$

where

$$\begin{aligned} s(x_q) &= \frac{r^{\lambda^c,\lambda^B}(x_q) u^{\lambda^c,\lambda^B}(x_q)}{t^{\lambda^c}(x_q)} \\ &= t^{\lambda^c}(x_q) P_B(x_q)(1 - P_B(x_q)) \end{aligned} \tag{5.34}$$

is the unnormalized contribution of bin $q$ belonging to phase point $x_q$. Naturally, the contribution to equation 5.33 of two bins corresponding to phase points $x_1$ and $x_2$ is given as

$$\begin{aligned} s(x_1) + s(x_2) = (1 - P_B(x_1))P_B(x_1)t(x_1) \\ + (1 - P_B(x_2))P_B(x_2)t(x_2) \end{aligned} \tag{5.35}$$

Now, our projection operations can basically be viewed as a process in which two or more bins are merged into a single bin in the reduced coordinate space. After merging these two bins we can write for the collective bin

$$\begin{aligned} s(x_1 + x_2) &= \frac{(r(x_1) + r(x_2))\,(u(x_1) + u(x_2))}{t(x_1) + t(x_2)} \\ &= \left(\frac{(1 - P_B(x_1))t(x_1) + (1 - P_B(x_2))t(x_2)}{t(x_1) + t(x_2)}\right) \\ &\times \left(\frac{P_B(x_1)t(x_1) + P_B(x_2)t(x_2)}{t(x_1) + t(x_2)}\right)(t(x_1) + t(x_2)) \end{aligned} \tag{5.36}$$

The difference between equation 5.36 and equation 5.35 is

$$\begin{aligned} s(x_1 + x_2) - s(x_1) - s(x_2) = \\ \left(\frac{(P_B(x_1) - P_B(x_2))^2 t(x_1)t(x_2)}{t(x_1) + t(x_2)}\right) \end{aligned} \tag{5.37}$$

Naturally, this difference is always positive except if $P_B(x_1) = P_B(x_2)$, then it is zero. Therefore, any projection will increase the overlap unless it is done such that phase points having the same committor end up in the same bin after the projection. In other words, if after the projection only a single orthogonal coordinate is left while the overlap has not increased, then all points having the same value for this orthogonal coordinate must have the same committor value. As such, we basically obtain an intersection of the committor surfaces with the $\lambda^c$ plane and the final one-dimensional $\Psi$ is a descriptor of this committor.

## 5.6 Conclusions

We devised a quantitative analysis method for identifying reaction mechanisms and initiation conditions for reactive events. The analysis is performed on the path sampling data that are already produced by path sampling simulations for computing reaction rates such as TIS [16], RETIS [17], and FFS [18]. Hence, a big advantage of our technique is that it does not require additional simulations which is generally needed for other analysis methods such a committor analysis. Also, our method does not require intensive iterations such as in the FFS-least-square estimation for determining the committor on-the-fly as linear or a polynomial function of predefined CVS during a FFS simulation. In contrast, our approach is a pure *a posteriori* method that can be applied after the simulation is finished, which allows for testing any possible set of CVs, which could either come from intuition after analyzing molecular trajectories or even from machine learning techniques.

Another advantage is that it is very flexible and also allows identifying momenta dependent variables which might be crucial steps in the reaction mechanism. The main idea is to determine probability distributions of first crossing points along order parameters orthogonal to the chosen reaction coordinate. Each plane with points having the same value of the reaction coordinate, also called interface, can be used to collect the first crossing points. Another plane further towards the product state can be used to set a condition of partial reactivity. Trajectories from the first crossing points with the first plane might or might not cross the plane defining partial reactivity. Based on this, the first crossing points are categorized and define "reactive" and "unreactive" distributions. Then, a simple overlap integral defines how well the orthogonal coordinates can help in the prediction of reactivity or not. Since crossing the full barrier can be a rare event, we showed how reweighting techniques can be used based on WHAM [24–26] to improve statistics. Moreover, the number of orthogonal coordinates can be reduced by applying projection operations which keep the overlap to its minimum. The latter approach, in principle, can also be applied to determine the phase space committor. We are aware that the analysis method described here, possibly with some adaptations, could be used in a wide range of different scientific fields such as economics and social sciences. Certainly, this is not the first method that tries, based on available data, to early identify events or parameters which possibly could predict whether something happens or not. One of such techniques is determination of receiver operator characteristic curves [36, 37] which is a common method in signal detection theory. These methods, although having similar aims, are based on a rather different mathematical formulations to measure the quality of predictiveness of some parameters. In addition, it would be very instructive to compare the kind of information that can be subtracted from the predictive power method, described in this chapter, and the information obtained from likelihood maximization [4, 5]. We plan to analyze possible analogies of these approaches in a future study.

The approach presented here allows one to get more valuable data from path sampling simulations and provides a mean to analyze reaction mechanism in a quantitative way. This output is likely to unravel hidden initiation events. Knowledge of these can then be exploited for designing new synthesis routes in which either new products are made or existing chemicals are generated with a lower energy cost or impact on the environment.

# Appendix

## 5.A WHAM Approach for Path Sampling

The WHAM methodology is well explained in previous publications [24–26] and also the WHAM approach applied on path sampling simulations have been reported before. The derivation that we give here is, however, slightly different than reported elsewhere. We give it here for completeness and to show that the WHAM weights can be optimized using non-standard terms. These terms come in addition to the terms depending on the correlation number, which are standard but often omitted. Whether these more refined weights should be applied or not will mainly depend on the accuracy of the path simulations.

The WHAM approach is based on the idea that whenever different simulations produce the same output, the best numerical result should be a weighted average of these outputs in which the weights have to chosen in order to minimize the overall error. One way to derive these weights is to write an general expression of the overall error for arbitrary weights. The optimizing set of weights can then be found by minimizing this expression with respect to the weights under the condition that the sum of weights must be equal to one. Intuitively we can, however, also use the following argument. Suppose there are two simulations with different simulation lengths computing the same average. If the two simulations are equally efficient, it is obvious that the best overall result is obtained by taking a weighted average in which the weights are taken to be proportional to the simulation length. Reversely, since the error scales as the inverse square root of the simulation length, it makes sense to weight different types of simulations, possibly using different algorithmic approaches or biases, with the inverse square of their error: $\omega_i \propto \epsilon_i^{-2}$ .

Now, consider a certain probability $p(\xi)$ which is for instance the probability that the system is within a bin as defined by the order parameter $\xi$. To improve the statistics we can apply biases in the sampling and unbias the results using a proper rescaling.

$$p_i^{\text{unb.}}(\xi) = Y_i(\xi) p_i^{\text{b.}}(\xi) \tag{5.38}$$

where $p_i^{\text{b.}}$ is the biased distribution of simulation $i$ and $Y_i$ is the $\xi$-dependent scaling factor to obtain the $i$-th realization of the unbiased distribution $p_i^{\text{unb.}}$. If we assume that $Y_i(\xi)$ can be viewed as a constant not bearing any error, then the error in $p_i^{\text{unb.}}$ is simply $\epsilon(p_i^{\text{unb.}}) = Y_i \epsilon(p_i^{\text{b.}})$. Moreover, since the calculation of $p_i^{\text{unb.}}(\xi)$ is generally related to the average of a binary function (being 1 if the system visits the bin at $\xi$ and zero otherwise), we can use the well known expression for its error (see e.g. [20, 38])

$$\begin{aligned}
\epsilon(p_i^{\text{b.}}(\xi)) &= \sqrt{\frac{p_i^{\text{b.}}(\xi)\left((1-p_i^{\text{b.}}(\xi)\right)}{n_i/\mathcal{N}_i}} \\
&= \sqrt{\frac{p_i^{\text{unb.}}(\xi)}{n'_i Y_i(\xi)}}
\end{aligned} \tag{5.39}$$

Here, $\mathcal{N}_i$ is the effective correlation (also called statistical inefficiency) and $n'_i = n_1/[\mathcal{N}_i\left((1-p_i^{\text{b.}}(\xi)\right)]$. Then, by taking the weights proportional to $\epsilon_i^{-2}\left(p_i^{\text{unb.}}(\xi)\right)$ with the condition $\sum_i \omega(\xi) = 1$ we get

$$\begin{aligned}
\omega_i(\xi) &= \frac{\left[Y_i(\xi)\,\epsilon\left(p_i^{\text{b.}}(\xi)\right)\right]^{-2}}{\sum_j \left[Y_j(\xi)\,\epsilon\left(p_j^{\text{b.}}(\xi)\right)\right]^{-2}} \\
&= \frac{\frac{1}{Y_i^2(\xi)}\frac{n'_i Y_i(\xi)}{p_i^{\text{unb.}}(\xi)}}{\sum_j \frac{1}{Y_j^2(\xi)}\frac{n'_j Y_j(\xi)}{p_j^{\text{unb.}}(\xi)}} \\
&\approx \frac{n'_i Y_i^{-1}(\xi)}{\sum_j n'_j Y_j^{-1}(\xi)}
\end{aligned} \tag{5.40}$$

where we used equations 5.38 and 5.39 and the fact that $p_i^{\text{unb.}}(\xi)$ should be similar for all $i$ since these values should converge for each simulation to the true unbiased distribution $\rho(\xi)$.

Hence, the weighted average, equation 5.17, equals

$$\rho(\xi) = \frac{\sum_{i=1} n'_i \rho_i^{\text{b.}}(\xi)}{\sum_j n'_j Y_j^{-1}(\xi)} = \frac{\sum_{i=1} n'_i[\xi]}{\sum_j n'_j Y_j^{-1}(\xi)} \tag{5.41}$$

where $n'_i[\xi]$ is the effective number of cycles in simulation $i$ that visit bin $\xi$. Here, effective means that one counts all the cycles visiting bin $\xi$ but finally divides this number by

$\mathcal{N}_i\left((1-p_i^{\mathrm{b.}}(\xi)\right)$. The reduction of $n_i$ and $n_i[\xi]$ with the correlation is standard though often omitted. Although $\mathcal{N}_i$ can be large, it cancels out in Eq 5.41 if the correlation number is similar for all $i$. The other factor $\left((1-p_i^{\mathrm{b.}}(\xi)\right)$ can generally be omitted whenever the bin-width is small enough such that $p_i^{\mathrm{b.}}(\xi) \ll 1$.

Now let us come back to the crossing probability. For $\mathcal{P}_A(\lambda|\lambda_0)$ we can write:

$$\begin{aligned}\mathcal{P}_A(\lambda|\lambda_0) &= \left\langle\theta(\lambda_{\max}(X)-\lambda)\right\rangle_{\varrho 0} \\ &= \left\langle\theta(\lambda_{\max}(X)-\lambda)\right\rangle_{\varrho_i}\mathcal{P}_A(\lambda_i|\lambda_0) \text{ for any } i<K(\lambda)\end{aligned} \tag{5.42}$$

where, in the second step, we applied a similar mathematical operation as the one in equation 5.20. Now, we can use equation 5.41 in which we replace $Y_i$ with $\mathcal{P}_A(\lambda_i|\lambda_0)$ and replace the bin around $\xi$ with an extended interval $[\lambda:\infty]$ for $\lambda_{\max}$:

$$\mathcal{P}_A(\lambda|\lambda_0) = \frac{\sum_{i=0}^{K(\lambda)} n_i'[\lambda]}{\sum_{j=0}^{K(\lambda)} n_j'[\mathcal{P}_A(\lambda_j|\lambda_0)]^{-1}} \tag{5.43}$$

where

$$\begin{aligned}n_i' &= \frac{n_i}{\mathcal{N}_i[1-\left\langle\theta(\lambda_{\max}(X)-\lambda)\right\rangle_{\varrho_i}]} \\ &= \frac{n_i}{\mathcal{N}_i\left\langle\theta(\lambda-\lambda_{\max}(X))\right\rangle_{\varrho i}}\end{aligned} \tag{5.44}$$

is the number of generated paths in simulation $i$ reduced by a factor proportional to the statistical inefficiency and the fraction of trajectories with $\lambda_{\max} < \lambda$. Similarly,

$$n_i'[\lambda] = n_i'\left\langle\theta(\lambda_{\max}(X)-\lambda)\right\rangle_{\varrho i} \tag{5.45}$$

is the number of trajectories in simulation $i$ with $\lambda_{\max} > \lambda$ scaled by the same factor. The bin at position $\xi$ is here replaced by the region $\lambda_{\max} > \lambda$. The small bin-width assumption can, hence, not be made. In other words, we can't assume that $[1-\left\langle\theta(\lambda_{\max}(X)-\lambda)\right\rangle_{\varrho_i}] = \left\langle\theta(\lambda-\lambda_{\max}(X))\right\rangle_{\varrho_i} \approx 1$ for all $i$. In fact, it can even be zero which, unless it is based on bad statistics, implies that the crossing probability has reached a plateau. However, if it is based on bad statistics the infinite weight of $1/\left\langle\theta(\lambda-\lambda_{\max}(X))\right\rangle_{\varrho i}$ will influence the results in a negative way. We, therefore, used the simpler expression of equation 5.18 which involves $n_i$ and $n[\lambda]$ instead of $n_i'$ and $n'[\lambda]$.

## Acknowledgments

The authors thank the Research Council of Norway project no. 237423 and the Faculty of Natural Sciences and Technology (NTNU) for support. Computational resources were granted by The Norwegian Metacenter for Computational Science (NOTUR), project NN9254K.

# Bibliography

[1] L. P. Geissler, C. Dellago, and D. Chandler. Kinetic pathways of ion pair dissociation in water. *J. Phys. Chem. B*, 103:3706–3710, 1999.

[2] P. G. Bolhuis, D. Chandler, C. Dellago, and P. L. Geissler. Transition path sampling: Throwing ropes over rough mountain passes, in the dark. *Annu. Rev. Phys. Chem.*, 53:291–318, 2002.

[3] C. Dellago, P. G. Bolhuis, and P. L. Geissler. Transition path sampling. *Adv. Chem. Phys.*, 123:1–78, 2002.

[4] B. Peters and B. L. Trout. Obtaining reaction coordinates by likelihood maximization. *J. Chem. Phys.*, 125:054108–10, 2006.

[5] B. Peters, G. T. Beckham, and B. L. Trout. Extensions to the likelihood maximization approach for finding reaction coordinates. *J. Chem. Phys.*, 127:034109–9, 2007.

[6] R. G. Best and G. Hummer. Reaction coordinates and rates from transition paths. *Proc. Natl. Acad. Sci. U. S. A.*, 102:6732–6737, 2005.

[7] E. Weinan, W. Q. Ren, and E. Vanden-Eijnden. Transition pathways in complex systems: Reaction coordinates, isocommittor surfaces, and transition tubes. *Chem. Phys. Lett.*, 413:242–247, 2005.

[8] E. Weinan and E. Vanden-Eijnden. Towards a theory of transition paths. *J. Stat. Phys.*, 123:503–523, 2006.

[9] E. Weinan and E. Vanden-Eijnden. Transition path theory and path finding algorithms for the study of rare events. *Annu. Rev. Phys. Chem.*, 61:391–420, 2010.

[10] B. Peters. Reaction coordinates and mechanistic hypothesis tests. *Annu. Rev. Phys. Chem.*, 67:669–690, 2016.

[11] A. Ma and A. R. Dinner. Automatic method for identifying reaction coordinates in complex systems. *J. Phys. Chem. B*, 109:6769–6779, 2005.

[12] M. Ferrario, M. Haughney, I. R. McDonald, and M. L. Klein. Molecular dynamics simulation of aqueous mixtures: Methanol, acetone, and ammonia. *J. Chem. Phys.*, 93:5156–5166, 1990.

[13] A. Luzar and D. Chandler. Effect of environment on hydrogen bond dynamics in liquid water. *Phys. Rev. Lett.*, 76:928–931, 1996.

[14] P. L. Geissler, C. Dellago, D. Chandler, J. Hutter, and M. Parrinello. Autoionization in liquid water. *Science*, 291:2121–2124, 2001.

[15] T. S. van Erp and E. J. Meijer. Proton-assisted ethylene hydration in aqueous solution. *Angew. Chem.-Int. Edit.*, 43:1659–1662, 2004.

[16] T. S. van Erp, D. Moroni, and P. G. Bolhuis. A novel path sampling method for the sampling of rate constants. *J. Chem. Phys.*, 118:7762–7774, 2003.

[17] T. S. van Erp. Reaction rate calculation by parallel path swapping. *Phys. Rev. Lett.*, 98:268301–4, 2007.

[18] R. J. Allen, P. B. Warren, and P. R. ten Wolde. Sampling rare switching events in biochemical networks. *Phys. Rev. Lett.*, 94:018104–4, 2005.

[19] E. Vanden-Eijnden, M. Venturoli, G. Ciccotti, and R. Elber. On the assumptions underlying milestoning. *J. Chem. Phys.*, 129:174102–13, 2008.

[20] T. S. van Erp. Efficiency analysis of reaction rate calculation methods using analytical models I: The two-dimensional sharp barrier. *J. Chem. Phys.*, 125:174106–20, 2006.

[21] T. S. van Erp. Dynamical rare event simulation techniques for equilibrium and nonequilibrium systems. In G. Nicolis and D. Maes, editor, *Kinetics and Thermodynamics of Multistep Nucleation and Self-Assembly in Nanoscale Materials: Advances in Chemical Physics, Vol 151*, volume 151 of *Advances in Chemical Physics*, pages 27–60. John Wiley and Sons, Inc, Hoboken, NJ, USA, 2012.

[22] C. Dellago, P. G. Bolhuis, and D. Chandler. Efficient transition path sampling: Application to Lennard-Jones cluster rearrangements. *J. Chem. Phys.*, 108:9236–9245, 1998.

[23] J. Rogal, W. Lechner, J. Juraszek, B. Ensing, and P. G. Bolhuis. The reweighted path ensemble. *J. Chem. Phys.*, 133:174109–12, 2010.

[24] A. M. Ferrenberg and R. H. Swendsen. Optimized Monte Carlo data analysis. *Phys. Rev. Lett.*, 63:1195–1198, 1989.

[25] S. Kumar, D. Bouzida, R. H. Swendsen, P. A. Kollman, and J. M. Rosenberg. The weighted histogram analysis method for free-energy calculations on biomolecules .1. The method. *J. Comput. Chem.*, 13:1011–1021, 1992.

[26] B. Roux. The calculation of the potential of mean force using computer simulations. *Comput. Phys. Commun.*, 91:275–282, 1995.

[27] B. Peters. Inertial likelihood maximization for reaction coordinates with high transmission coefficients. *Chem. Phys. Lett.*, 554:248–253, 2012.

[28] R. G. Mullen, J. E. Shea, and B. Peters. Transmission coefficients, committors, and solvent coordinates in ion-pair dissociation. *J. Chem. Theory Comput.*, 10:659–667, 2014.

[29] A. Lervik and T. S. van Erp. Gluing potential energy surfaces with rare event simulations. *J. Chem. Theory Comput.*, 11:2440–2450, 2015.

[30] A. D. Becke. Density-functional exchange-energy approximation with correct asymptotic behavior. *Phys. Rev. A*, 38:3098–3100, 1988.

[31] C. Lee, W. Yang, and R. G. Parr. Development of the Colle-Salvetti correlation-energy formula into a functional of the electron density. *Phys. Rev. B*, 37:785–789, 1988.

[32] J. VandeVondele and J. Hutter. Gaussian basis sets for accurate calculations on molecular systems in gas and condensed phases. *J. Chem. Phys*, 127:114105–9, 2007.

[33] J. Hutter, M. Iannuzzi, F. Schiffmann, and J. VandeVondele. CP2K: Atomistic simulations of condensed matter systems. *Wiley Interdiscip. Rev: Comput. Mol. Sci.*, 4:15–25, 2014.

[34] A. Hassanali, M. K. Prakash, H. Eshet, and M. Parrinello. On the recombination of hydronium and hydroxide ions in water. *Proc. Natl. Acad. Sci. USA*, 108:20410–20415, 2011.

[35] A. Luzar and D. Chandler. Effect of environment on hydrogen bond dynamics in liquid water. *Phys. Rev. Lett.*, 76:928–931, 1996.

[36] J. P. Egan. *Signal detection theory and ROC analysis*. Series in Cognition and Perception. Academic Press, New York, NY, 1975.

[37] S. Hallerberg and A. S. de Wijn. Understanding and controlling regime switching in molecular diffusion. *Phys. Rev. E*, 90:062901–7, 2014.

[38] M. J. Ruiz-Montero, D. Frenkel, and J. J. Brey. Efficient schemes to compute diffusive barrier crossing rates. *Mol. Phys.*, 90:925–941, 1996.

# Chapter 6

# Concerted and Stepwise Autoionization of Water

Mahmoud Moqadam, Anders Lervik, Enrico Riccardi, Titus S. van Erp

Manuscript

**Abstract -** Autoionization of water at room temperature is investigated by combining a recently developed rare event simulation method with ab initio molecular dynamics. This approach allows sampling of rare autoionization events which happen on the timescale of minutes. Our simulations shed light on the autoionization mechanism and we show how local collective variables such as the hydrogen bond wire length connecting the nascent ions and the distortion from tetrahedral arrangement can be used to predict autoionization events. Using these order parameters, we discuss the mechanism and comment on the possibility of enhancing water dissociation.

## 6.1 Introduction

Understanding the behaviour of aqueous solutions is of crucial importance in many areas of chemistry and biology. Water plays an important role as a universal solvent for a wide variety of chemical processes and one of the most important properties of water is its ability to act both as an acid and as a base: In pure water or aqueous solution, water molecules autoprotolyse and form hydroxide ($OH^-$) and hydronium ($H_3O^+$) ions which exist as Eigen or Zundel-like structures [1–4] in solution. Experiments show that the mean lifetime before undergoing autoionization is about 11 hours [5,6] for an individual water molecule and this makes the autoionization event extremely rare compared to the time scale for solvent reorganizations and molecular motions.

The scarcity by which individual water molecules dissociate is also reflected by the low water dissociation equilibrium constant and the high rate of the reverse recombination reaction. In fact, the low conductivity of pure water makes room-temperature water electrolysis challenging and it has to be performed under acidic or alkaline conditions. Electrolysis of water is potentially one of the key steps in the “Hydrogen Economy” where hydrogen is the energy carrier, preferably produced from water using renewable energy sources. Currently, the majority (96% [7]) of hydrogen is produced in coal gasification and natural gas reforming. This is less cost-intensive, but requires a relatively expensive $CO_2$ capture and storage process to be sustainable [8]. Understanding the mechanism for water dissociation is a prerequisite for energy efficient water electrolysis. However, this is one of the most challenging problems in physical chemistry and the autoionization event has not been directly probed by experiments. Typically, the dissociation rate is obtained using the water dissociation equilibrium constant and the rate for the much faster recombination reaction, see e.g. [5,6].

The experimental difficulties make the autoionization event a pertinent target for computer simulations and previous constrained ab initio simulations has indeed shed some light on the mechanism [9–11]. However, the selection of a reaction coordinate that accurately quantifies the progress of the reaction is difficult and the use of constraints leads to a loss of the spontaneous dynamics of the system. These serious limitations can be avoided by making use of path sampling simulation methods such as transition path sampling (TPS) [12] or (replica exchange) transition interface sampling ((RE)TIS) [13, 14]. Both TIS and RETIS are efficient (with RETIS being the most efficient [14]) algorithms based on TPS and these methods have in common that they are designed for sampling rare events without artificially altering the dynamics. Compared to methods based on free energy calculations, the efficiency of path sampling methods are less influenced by the choice of the order parameter [15]. Geissler et al. [16] made use of TPS for ab initio simulations of the autoionization event and demonstrated that the mechanism involves transfer of protons along a hydrogen bond wire with concomitant breaking of the wire. Further, it was found that local order parameters could not be used to describe the event. Due to the computational cost of performing ab initio simulations of the autoionization event and the lack of more efficient methods such as (RE)TIS, only a limited number of reactive trajectories were obtained which preclude a statistical analysis of the event.

The importance of the hydrogen bond wire connecting the ions was also demonstrated by Hassanali et al. [17] who studied the rapid recombination reaction with ab initio simulations. It was demonstrated that the recombination event takes place by a collective compression of the water wire bridging the ions, followed by a triple concerted proton jump. The hydroxide ion which is neutralized is then left in a hyper-coordinated state and Hassanali et al. hypothesized that it could serve, together with the compression of the wire, as a nucleation site for autoionization. The study [17] explained the charge separated state and the recombination process; however, it does not clarify the molecular mechanism of the dissociation process nor quantifies its rate. In particular: what are the conditions for initiation of the autoionization event? In this work we aim to *quantitatively* tackle this question and describe the mechanism and the importance of collective variables such as the hydrogen bond wire length. To this aim, we harvest reactive events using the RETIS algorithm and analyse them using a recently developed rare event analysis method [18]. Our results demonstrate that the local water structure is important for the reactive event and in particular the initiation.

## 6.2 Methodology

### 6.2.1 Simulation methods

The MD simulations required by the RETIS algorithm [14] were performed with the Born Oppenheimer MD capabilities of the CP2K program package [19]. We used a BLYP functional with a DZVP-MOLOPT [20] basis set and a plane-wave cutoff of 280 Ry. The BLYP functional has been shown to give an accurate description of the structure and dynamics of water [21]. Further, the collective compression of the hydrogen bond wire and the motion of the protons in the bulk water is independent of the choice of functional and basis set [17].

The initial system consisted of 32 water molecules placed in a cubic simulation box of $9.85 \times 9.85 \times 9.85$ Å$^3$. All MD simulations were carried out under constant energy (NVE) dynamics, with a time step of 0.5 fs and periodic boundaries.

The transition region was divided into 20 path ensembles by positioning RETIS interfaces at $\lambda = \{1.07, 1.10, 1.13, 1.16, 1.19, 1.22, 1.25, 1.28, 1.31, 1.34, 1.39\ 1.43, 1.48, 1.52, 1.56, 1.80, 2.00, 2.50, 2.90, 3.29\}$ Å. In addition, a final interface was placed at $\lambda = \infty$ such that all trajectories were propagated until they reached the pure water state again. After generating an initial path for each path ensemble (this was done by repeatedly modifying the momenta of the particles and evolving the system forward in time until valid paths were obtained) the RETIS algorithm either attempts to swap paths between different path ensembles or generate new trajectories by the so-called shooting or the time-reversal move. In our simulations the probability of performing a swapping move was set to 50% while the probabilities of the two other moves were both set to 25%. New velocities for the shooting move were drawn from a Maxwell-Boltzmann distribution corresponding to an average temperature of 300 K.

We performed about 24 000 steps with the RETIS algorithm which generated between 8000 and 18 000 distinct trajectories for the different ensembles. The length of the trajectories range from 13.5 fs to 1365 fs and we disregarded the first 400 trajectories in our analysis.

### 6.2.2 Analysis of trajectories

For trajectories harvested with the RETIS algorithm we have calculated additional collective variables: the hydrogen bond wire length ($w_i$), the number of hydrogen bond donors ($n_\mathrm{d}$) and acceptors ($n_\mathrm{a}$) and the orientation order parameter ($q$). Using the first configuration in each trajectory, hydrogen atoms were assigned to the closest oxygen atom and this defined the initial $H_2O$ molecules. Then, the hydrogen bond network was obtained for each configuration in the trajectory. Hydrogen bonds were identified using the criteria of Luzar and Chandler [22] and all (shortest) hydrogen bond connections between all pairs of water molecules were determined using the Floyd-Warshall algorithm [23]. This allowed us to represent the hydrogen bond structure as a graph. Next the oxygen atom ($O^\lambda$) used in the definition of the order parameter was identified. With no $OH^-$ present, this is the oxygen atom for which the covalent O-H distance is largest and when we have $OH^-$ present in the system this is the $OH^-$ oxygen atom. After identifying $O^\lambda$, we obtained the number of hydrogen bonds accepted ($n_\mathrm{a}$) and donated ($n_\mathrm{d}$) by the water specie containing it. The relevant hydrogen bond wire was obtained using the following criteria: (i) The wire should contain the oxygen atom used for the order parameter (identified as explained above) when the order parameter first crossed 1.15 Å, (ii) the wire should contain $i$ water species, (iii) the wire should be the shortest of the wires where two criteria (i) and (ii) are met. The length of the wire was defined as the sum of the O-O distances of consecutive molecules in the wire.

The orientation order parameter measures the distortion from a tetrahedral orientation of four water molecules around a central molecule and is defined by [24]

$$q = 1 - \frac{3}{8}\sum_{j=1}^{3}\sum_{k=j+1}^{4}\left(\cos\psi_{jk} + \frac{1}{3}\right)^2 \tag{6.1}$$

Here, $\psi_{jk}$ is the angle formed by the central oxygen and the oxygens of it's four nearest neighbors. For a perfect tetrahedral orientation $q = 1$ and it is $q \neq 1$ otherwise.

After calculating these additional collective variables, we analysed the trajectories using the methodology of van Erp et al. [18]. For the analysis we used 100 interfaces both for $\lambda^{\mathrm{r}}$ and $\lambda^{\mathrm{c}}$ for the range $0 < \lambda/\text{Å} < 6.4$. The histograms in the collective variable space was constructed using 40 bins for $4.0 \leq w_3/\text{Å} \leq 7.0$, $7.0 \leq w_4/\text{Å} \leq 9.6$, $9.0 \leq w_5/\text{Å} \leq 12$, 25 bins for $0 \leq q \leq 1$, while the bins (mid points) were simply placed at $-0.5, 0.5, 1.5, \ldots, 6.5$ for both $n_{\mathrm{a}}$ and $n_{\mathrm{d}}$.

## 6.3 Results and discussion

The autoionization event was investigated by sampling trajectories generated by the RETIS algorithm [14] in combination with ab initio molecular dynamics (MD) simulations as described in the methods. The RETIS algorithm makes use of an order parameter, $\lambda$, capable of distinguishing the initial and final state. Here, we have used a relatively simple geometric distance order parameter (see illustration in figure 6.1): If the system consist of only $H_2O$ species, $\lambda$ is the largest covalent O–H bond distance, and if the system contains $OH^-$ and $H_3O^+$ species, $\lambda$ is taken as the shortest distance between the oxygen in $OH^-$ and the hydrogen atoms in $H_3O^+$. The type of species are identified by allocating to each hydrogen a single bond connecting it to the closest oxygen. We note that this definition does not require a threshold for defining a chemical bond nor does it constrain the order parameter to specific water molecules for the duration of the simulation, and we will in the following refer to the oxygen atom used for the order parameter as $O^{\lambda}$. Hence, we initially compute the rate for observing a dissociation event of *any* water molecule in the system instead of a single targeted O–H bond or water molecule. This value is easier to compute since it is higher and it can be normalised (by the number of water molecules) to the actual dissociation rate.

The RETIS algorithm proceeds by positioning several interfaces ($\lambda_0 < \lambda_1 < \ldots < \lambda_N$) along the order parameter which defines the so-called path ensembles. The dissociation rate constant, $k_D$, can then be expressed as the product of the flux, $f_A$, through the first interface ($\lambda_0$) and a (conditional) probability, $\mathcal{P}_A(\lambda_N|\lambda_0)$,

$$k_D = f_A \times \mathcal{P}_A(\lambda_N|\lambda_0). \tag{6.2}$$

Here, $\mathcal{P}_A(\lambda_N|\lambda_0)$, is the probability of reaching the final state ($\lambda > \lambda_N$) before (possibly) returning to the initial state given that the initial interface has been crossed. This probability can be estimated by as a product of similarly defined history dependent conditional probabilities for the individual path ensembles, $\mathcal{P}_A(\lambda_i|\lambda_{i-1})$: $\mathcal{P}_A(\lambda_N|\lambda_0) = \prod_{i=1}^{N} \mathcal{P}_A(\lambda_i|\lambda_{i-1})$. The number and location of the interfaces do not alter the results, only the efficiency for obtaining them.

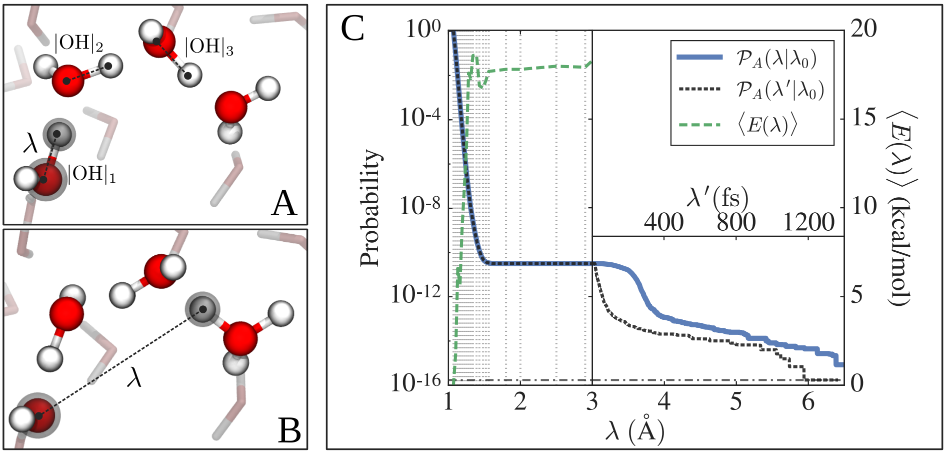

**Figure 6.1:** (Panel A and B) Definition of the order parameter ($\lambda$, dashed line), taken as the largest covalent O–H distance in the system (panel A, when no ionic species are present) or as the shortest distance between the $OH^-$ oxygen atom and the hydrogen atoms in $H_3O^+$ (panel B, when ionic species are present). A hydrogen bond wire with 4 members is shown with red (oxygen) and white (hydrogen) spheres and the distances $|OH|_1$, $|OH|_2$, $|OH|_3$ are also indicated. These distances are used to investigate the possible concerted motion of hydrogen atoms along the wire. (Panel C) The crossing probability ($\mathcal{P}_A$) and average energy of trajectories ($\langle E \rangle$) as a function of the order parameter. The (black) dashed line is calculated using an alternative definition of the order parameter ($\lambda'$) where the trajectory length (in fs) defines the order parameter for $\lambda > 3$ Å. The horizontal dot-dashed line is the crossing probability ($1.7 \times 10^{-16}$) obtained at the plateau for long paths ($\lambda' \geq 1200$ fs). The activation energy is equal to the plateau value of the average energy which approaches 17.8 kcal/mol.

In figure 6.1 we show the crossing probability obtained by the RETIS algorithm as a function of the order parameter. However, as the interionic distance is not necessarily a useful order parameter for distinguishing the neutral and charge-separated states (as largely separated ions might still recombine fast within several fs [16]), we used path reweighting [25] to project the crossing probability on another order parameter which improves the identification of the metastability region of the ionized state. Specifically, we used the trajectory length (in fs) as an alternative order parameter, $\lambda'$, when $\lambda > 3$ Å and detected a semi plateau region for trajectories longer than 1.2 ps which was then used as a stability criterion. We show also the average energy of the different path ensembles which is expected to converge to a plateau value equal to the activation energy [26, 27]. This computed activation energy is derived from the temperature derivative of the rate constant. Hence, it gives in principle a more direct comparison to experiments than standardly computed free energy barriers which depend on the choice of order parameter. From the RETIS simulations we find a crossing probability of $1.7 \times 10^{-16}$ and an initial normalised flux of $2.9 \times 10^{-3}$ fs$^{-1}$ resulting in a rate constant $k_{\mathrm{D}} = f_A \times \mathcal{P}_A = 4.9 \times 10^{-4}$ s$^{-1}$. This compares well with the experimentally determined dissociation constants at 25°C by Eigen and Maeyer ($k_{\mathrm{D}} = 0.25 \times 10^{-4}$ s$^{-1}$) [5] and by Natzle and Moore ($k_{\mathrm{D}} = 0.204 \times 10^{-4}$ s$^{-1}$) [6]. The activation energy obtained from the average energy of the accepted paths is approximately 17.8 kcal/mol. For comparison, an Arrhenius plot of the experimental data of Natzle and Moore [6] results in an activation energy of approximately 17.3 kcal/mol while Eigen and Maeyer [5] reported an activation energy of 15.5–16.5 kcal/mol.

In addition to straightforwardly yielding the rate constant, the RETIS algorithm also generate reactive (and nonreactive) trajectories which can be used to discover possible mechanisms. We have analysed the reactive trajectories both qualitatively and quantitatively using a recently developed rare event analysis method [18]. For this analysis we have considered additional collective variables, $\xi$, relevant for the mechanism. The ability to form hydrogen bonds is one of the characteristic features of water [28] and previous computational studies have demonstrated the relevance of the hydrogen bond wire connecting the ionic species [16, 17]. Therefore, we base our analysis on the hydrogen bond connectivity and hydrogen bond wires. In our case, we aim to *predict* the outcome of initiated trajectories and in particular the initiation conditions for reactive events. Thus, we cannot simply define the hydrogen bond wires as connecting the ionic species since this is one of the outcomes we wish to predict. We rather define the hydrogen bond wire for a single trajectory as the shortest wire containing the O$^{\lambda}$-specie and $i-1$ other water species at the point in time when $\lambda$ is greater than a given threshold value, $\lambda_{\mathrm{t}} = 1.15$ Å. This defines a wire containing $i$ water species and the length of this wire, $w_i$, is obtained as the sum of the O–O distances of consecutive members.

Anticipating the discussion of our results on wires of different length, we find that when the ionic species are separated by at least two water molecules, the ionic state survives for a longer time compared to cases where they are separated by just one water molecule. This implies that (at least) three proton transfer events have occurred. We have monitored the distances of the initially covalent O–H bonds, and show these for the first ($|\mathrm{OH}|_1$), second ($|\mathrm{OH}|_2$) and third ($|\mathrm{OH}|_3$) transferred proton in figure 6.2. As can be expected from Grotthuss mechanism [29,30], the initial autoionization event is followed by several proton transfers in which the ionic species separate along the wire. Figure 6.2 shows

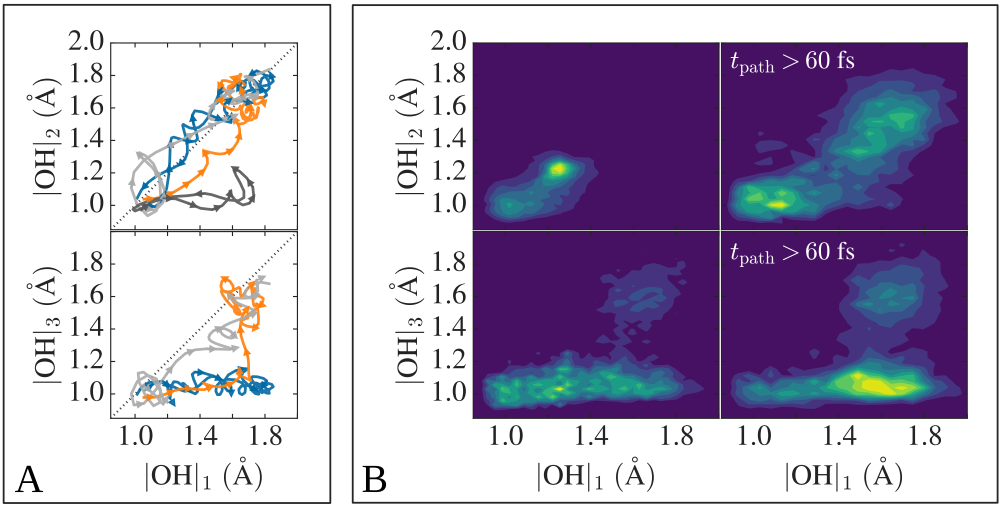

**Figure 6.2:** The concerted behavior of the autoionization event, obtained in the final path ensemble. (Panel A) The distances ($|OH|_i$) of initially covalent O–H bonds for the first ($i = 1$), second ($i = 2$) and third ($i = 3$) proton transfer in four trajectories. The arrows show the time direction and the different trajectories exemplify different types of hydrogen transfer: Failed stepwise (dark gray color, only shown for $|OH|_1$-$|OH|_2$), concerted (light gray color), concerted only for $|OH|_1$-$|OH|_2$ (blue color) and concerted-stepwise (orange color). (Panel B) Using all trajectories in the final path ensemble (having $\lambda > 3.29$ Å by definition), densities for $|OH|_1$-$|OH|_2$ and $|OH|_1$-$|OH|_3$ has been obtained (leftmost column). The right-most column show the densities when considering trajectories with a length $t_{\text{path}} > 60$ fs.

that this can happen both in a concerted and stepwise way: The transfer of the first and second proton occurs almost exclusively in a concerted way, while the transfer of the third proton (if it occurs) can happen in a stepwise or in a concerted way. This is also reflected in the waiting time between these events shown in figure 6.3, where the waiting time distribution between the third and second proton transfer is broader compared to the first and second transfer. To investigate if the wires remain unbroken, we have also calculated the hydrogen bond wire in the time-reverse trajectories. Figure 6.4 shows that trajectories are indeed starting and ending with a contracted wire ($< 7.6$ Å) as reported by Hassanali et al. [17], but at the end these wires do not necessarily contain the same oxygen atoms. This is indicative for the wire being broken and reformed by other water molecules. The majority of the longer trajectories reform via another wire, but there is still a significant number of long trajectories ($> 1.0$ ps) for which the recombination is exactly the same as the dissociation path. This seems to disprove the hypothesis of Geissler et al. [16] that breakage of the wire is a necessary condition to reach a metastable state. We find that, unless the trajectories are short, we most often identify different wires in the time-reversed direction.

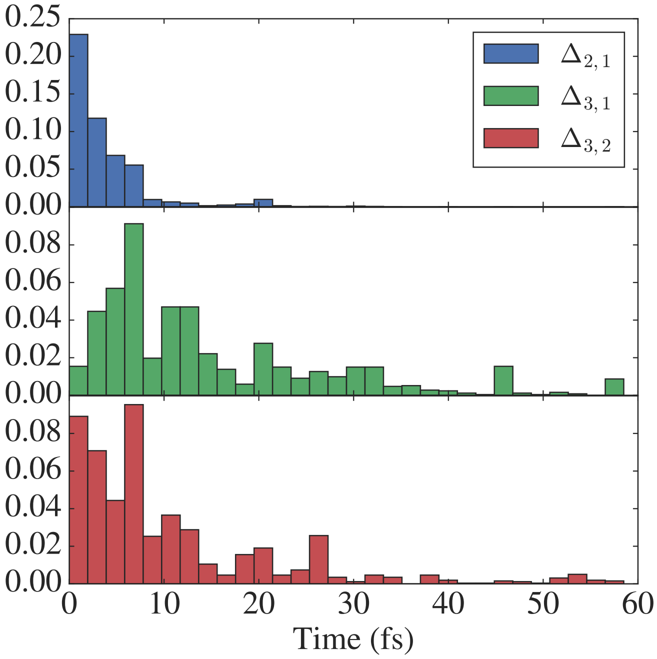

**Figure 6.3:** Distribution of waiting times between initiation of hydrogen transfer events, obtained in the final path ensemble. From top to bottom we show the waiting time between initiation of the first and second hydrogen transfer event ($\Delta_{2,1}$), the first and third ($\Delta_{3,1}$), and the second and third event ($\Delta_{3,2}$).

Next, we address the reaction mechanism and initiation conditions quantitatively. We consider an additional interface for the analysis, $\lambda^{\mathrm{c}} > \lambda_0$, and focus on the first crossing point for the trajectories with this interface. Here, additional collective variables ($\xi$) form a distribution of possible values and we classify the trajectories as reactive or nonreactive depending on them reaching a selected $\lambda^{\mathrm{r}} > \lambda^{\mathrm{c}}$ or not. This gives two distributions: $r^{\lambda^{\mathrm{c}},\lambda^{\mathrm{r}}}(\xi)$; the fraction of reactive trajectories (passing $\lambda^{\mathrm{c}}$ and reaching $\lambda^{\mathrm{r}}$) and $u^{\lambda^{\mathrm{c}},\lambda^{\mathrm{r}}}(\xi)$; the fraction of nonreactive trajectories (passing $\lambda^{\mathrm{c}}$ but fail to reach $\lambda^{\mathrm{r}}$). If, for instance, $u^{\lambda^{\mathrm{c}},\lambda^{\mathrm{r}}}(\xi) = 0$, we know immediately that if we cross $\lambda^{\mathrm{c}}$ at $\xi$, the trajectory will be reactive. Using these distributions, we consider the predictive ability, $\mathcal{T}_A^{\lambda^{\mathrm{c}},\lambda^{\mathrm{r}}}$, defined by [18]

$$\mathcal{T}_A^{\lambda^{\mathrm{c}},\lambda^{\mathrm{r}}} = 1 - \frac{1}{\mathcal{P}_A(\lambda^{\mathrm{r}}|\lambda^{\mathrm{c}})} \int \frac{r^{\lambda^{\mathrm{c}},\lambda^{\mathrm{r}}}(\xi) u^{\lambda^{\mathrm{c}},\lambda^{\mathrm{r}}}(\xi)}{r^{\lambda^{\mathrm{c}},\lambda^{\mathrm{r}}}(\xi) + u^{\lambda^{\mathrm{c}},\lambda^{\mathrm{r}}}(\xi)} \mathrm{d}\xi, \tag{6.3}$$

which satisfy $\mathcal{P}_A(\lambda^{\mathrm{r}}|\lambda^{\mathrm{c}}) \leq \mathcal{T}_A^{\lambda^{\mathrm{c}},\lambda^{\mathrm{r}}} \leq 1$. If the collective variables do not correlate with reactivity the lower limit is attained but if the collective variables are relevant for the

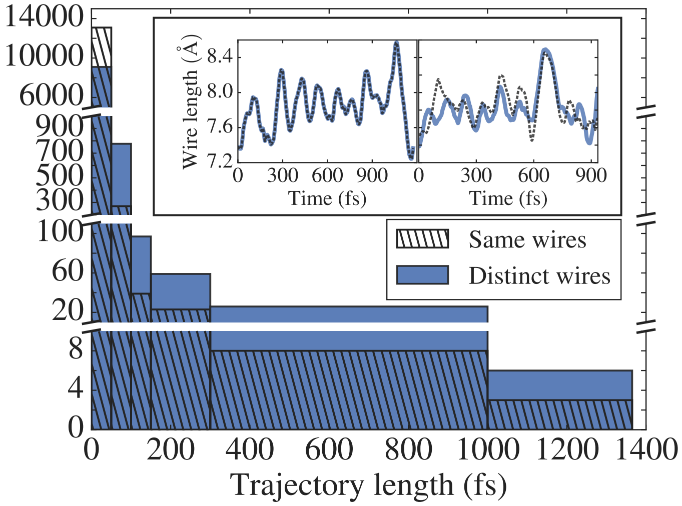

**Figure 6.4:** Distribution of trajectory lengths for the final path ensemble. The trajectories have been classified according to the identified hydrogen bond wire in the forward and time-reversed directions as: (1) The same wire is identified in both directions (white color and striped pattern: "Same wires") or (2) different wires are identified in the two directions (color blue: "Distinct wires"). The inset show two examples for the length of the four-membered wires for the two classes (forward direction in solid blue, time-reversed direction in dashed black lines).

reaction, $\mathcal{T}_A^{\lambda^{\mathrm{c}},\lambda^{\mathrm{r}}} > \mathcal{P}_A(\lambda^{\mathrm{r}}|\lambda^{\mathrm{c}})$. Thus, for a set of collective variables, these distributions give us a measure of how relevant the variables are for the mechanism. Further, we see from the definition in equation (6.3) that if the overlap of the two distributions is small, then the predictive ability will increase.

As stated above, we have investigated the hydrogen bond wires of different length and we now have a quantitative way of distinguishing them. In addition, we have considered three additional collective variables which describe the local structure surrounding the $\mathrm{O}^{\lambda}$-specie: (i) The orientational order parameter, $q$, obtained using the angles defined by $\mathrm{O}^{\lambda}$ and it's four nearest oxygen atoms (by the definition $q = 1$ for a perfect tetrahedral structure and $q \neq 1$ otherwise) and (ii) the number of hydrogen bonds accepted, $n_{\mathrm{a}}$, and (iii) donated, $n_{\mathrm{d}}$, by the water specie containing $\mathrm{O}^{\lambda}$. In figure 6.5-panel A we show $\mathcal{T}_A^{\lambda^{\mathrm{c}},\lambda^{\mathrm{r}}}$ normalized by the probability for these collective variables. Comparing the hydrogen bond wire lengths ($w_3$, $w_4$, $w_5$) we find that $w_4$ and $w_5$ are more correlated with reactivity and that $w_4$ is more relevant than $w_5$ for larger $\lambda^{\mathrm{r}}$. For the other collective variables, the results show that $q$ and $n_{\mathrm{a}}$ are also correlated with reactivity but $n_{\mathrm{d}}$ is less relevant. Using different combinations of the more relevant collective variables (e.g. $\xi = (w_4, q)$) we find that we can improve the predictive capacity by a factor $10^7$ compared to the crossing probability. We note that since the crossing probability is small in this case we have $\mathcal{T}_A^{\lambda^{\mathrm{c}},\lambda^{\mathrm{r}}} \sim 0.1$ and we cannot perfectly predict the outcome. However, our results show that the hydrogen bond wire and the local water structure around the O$^{\lambda}$ specie are important for the mechanism.

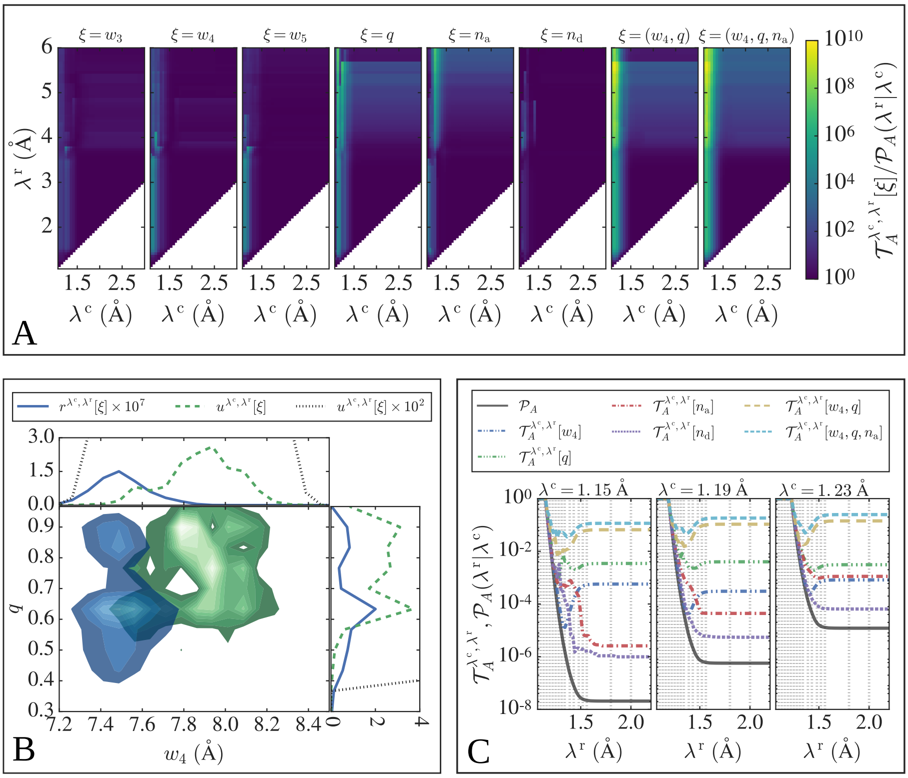

**Figure 6.5:** (Panel A) The predictive power ($\mathcal{T}_A^{\lambda^{\mathrm{c}},\lambda^{\mathrm{r}}}[\xi]$) relative to the crossing probability ($\mathcal{P}_A$) using additional collective variables: Hydrogen bond wires of different length ($\xi = w_3, \xi = w_4, \xi = w_5$), the orientational order parameter ($\xi = q$) and the number of hydrogen bonds accepted ($\xi = n_{\mathrm{a}}$) and donated ($\xi = n_{\mathrm{d}}$) by the O$^{\lambda}$-specie. (Panel B) The distributions $r^{\lambda^{\mathrm{c}},\lambda^{\mathrm{r}}}$ and $u^{\lambda^{\mathrm{c}},\lambda^{\mathrm{r}}}$ using the collective variables $\xi = (w_4, q)$ for $\lambda^{\mathrm{c}} = 1.15$ Å and $\lambda^{\mathrm{r}} = 2.0$ Å. The top and right insets show the one-dimensional distributions for $\xi = w_4$ and $\xi = q$, respectively. (Panel C) The predictive power and the crossing probability as a function of $\lambda^{\mathrm{r}}$ for $\lambda^{\mathrm{c}} = \{1.15, 1.19, 1.23\}$ Å and different combinations of collective variables. Due to the threshold criterion for defining the wires (see the main text), the probability is shifted so that $\mathcal{P}_A = 1$ for $\lambda < 1.15$ Å.

Returning to the question on initiation conditions we investigate these collective variables in more detail. In figure 6.5-panel B we show the $r^{\lambda^{\mathrm{c}},\lambda^{\mathrm{r}}}(\xi)$ and $u^{\lambda^{\mathrm{c}},\lambda^{\mathrm{r}}}(\xi)$ distributions for $\lambda^{\mathrm{c}} = 1.15$ Å, $\lambda^{\mathrm{r}} = 2.0$ Å and $\xi = (w_4, q)$. Hence, we exam all dissociation events, even the ones that recombine quickly. Along the $w_4$ coordinate we see a clear separation of the two distributions and this indicates that trajectories crossing $\lambda^{\mathrm{c}} = 1.15$ Å have a larger probability of being reactive for shorter wires (smaller $w_4$). This supports the hypothesis of a "compressed" wire as an important condition for autoionization, suggested by Hassanali et al. [17]. Along the $q$ coordinate there is a larger overlap of the two distributions. However, we find that $r^{\lambda^{\mathrm{c}},\lambda^{\mathrm{r}}}$ is shifted towards lower $q$ values compared to $u^{\lambda^{\mathrm{c}},\lambda^{\mathrm{r}}}$. This indicates that a distortion from a tetrahedral arrangement around the dissociating water specie may also initiate the event. Finally, in figure 6.5-panel C we show $\mathcal{T}_A^{\lambda^{\mathrm{c}},\lambda^{\mathrm{r}}}$ as functions of $\lambda^{\mathrm{r}} \leq 2$ Å for $\lambda^{\mathrm{c}} = \{1.11, 1.15, 1.2\}$ Å compared to the crossing probability using several combinations of the collective variables $\xi = \{w_4, q, n_{\mathrm{a}}, n_{\mathrm{d}}, (w_4, q), (w_4, q, n_{\mathrm{a}})\}$. Inspecting these results, we find again that the two collective variables $w_4$ and $q$ are more relevant for reactivity than the other variables. We also find again that $\mathcal{T}_A^{\lambda^{\mathrm{c}},\lambda^{\mathrm{r}}} \sim 0.1 < 1$ which indicates that there are other collective variables important for description. These might be local ones we did not consider yet, or, possibly, non-local variables are needed as suggested by Geissler et al. [16].

Overall the results shown in figure 6.5 show that a compression of the water wire (as measured by $w_4$) and hyper-coordination (measured by $n_{\mathrm{a}}$) or distortion (measured by $q$) are necessary initiation conditions for autoionization. These are not sufficient conditions as shown by the values of $\mathcal{T}_A^{\lambda^{\mathrm{c}},\lambda^{\mathrm{r}}}$ in figure 6.5-panel C. Still, our findings suggest that water splitting could be tremendously enhanced if we would be able to manipulate the water structure towards the topological relevant initiation region for autoionization, for instance, by bringing into contact with well-designed nanostructured materials possibly in combination with applying electric fields or inclusions of ions.

## 6.4 Conclusions

We have investigated the autoionization of water at room temperature using an unconstrained ab initio rare event simulation method. Our simulations sample reactive events that happen on the time scale of *minutes* and we have demonstrated that autoionization can be initiated by a compression of a hydrogen bond wire and distortion from a tetrahedral arrangement. Our findings are valuable for the future development of more efficient and sustainable approaches for hydrogen production since it provides clues on how the water structure needs to be manipulated in order to increase the rate of dissociation.

### Acknowledgements

The authors thank the Research Council of Norway project no. 237423 and the Faculty of Natural Sciences and Technology (NTNU) for support. This research was supported in part with computational resources at NTNU provided by NOTUR, http://www.sigma2.no

## Author contributions

MM and AL performed the simulations and the analysis. ER, MM and TSvE wrote the computer code for the ab initio RETIS algorithm. TSvE guided the overall supervision of the project. All authors contributed to the writing of the manuscript.

# Bibliography

[1] M. E. Tuckerman, K. Laasonen, M. Sprik, and M. Parrinello. Ab initio molecular dynamics simulation of the solvation and transport of $H_3O^+$ and $OH^-$ ions in water. *J. Phys. Chem.*, 99:5749–5752, 1995.

[2] D. Marx, M. E. Tuckerman, J. Hutter, and M. Parrinello. The nature of the hydrated excess proton in water. *Nature*, 397:601–604, 1999.

[3] M. E. Tuckerman, D. Marx, and M. Parrinello. The nature and transport mechanism of hydrated hydroxide ions in aqueous solution. *Nature*, 417:925–929, 2002.

[4] E. F. Aziz, N. Ottosson, M. Faubel, I. V. Hertel, and B. Winter. Interaction between liquid water and hydroxide revealed by core-hole de-excitation. *Nature*, 455:89–91, 2008.

[5] M. Eigen and L. de Maeyer. Self-dissociation and protonic charge transport in water and ice. *Proc. R. Soc. Lond. A Math. Phys. Sci.*, 247:505–533, 1958.

[6] W. C. Natzle and C. B. Moore. Recombination of $H^+$ and $OH^-$ in pure liquid water. *J. Phys. Chem.*, 89:2605–2612, 1985.

[7] International Energy Agency (IEA). Technology roadmap: Hydrogen and fuel cells, 2015.

[8] M. Voldsund, K. Jordal, and R. Anantharaman. Hydrogen production with $CO_2$ capture. *Int. J. Hydrogen Energy*, 41:4969–4992, 2016.

[9] B. L. Trout and M. Parrinello. The dissociation mechanism of $H_2O$ in water studied by first-principles molecular dynamics. *Chem. Phys. Lett.*, 288:343–347, 1998.

[10] B. L. Trout and M. Parrinello. Analysis of the dissociation of $H_2O$ in water using first-principles molecular dynamics. *J. Phys. Chem. B*, 103:7340–7345, 1999.

[11] M. Sprik. Computation of the p*K* of liquid water using coordination constraints. *Chem. Phys.*, 258:139–150, 2000.

[12] C. Dellago, P. G. Bolhuis, and D. Chandler. Efficient transition path sampling: Application to lennard-jones cluster rearrangements. *J. Chem. Phys.*, 108:9236–9245, 1998.

[13] T. S. van Erp, D. Moroni, and P. G. Bolhuis. A novel path sampling method for the sampling of rate constants. *J. Chem. Phys.*, 118:7762–7774, 2003.

[14] T. S. van Erp. Reaction rate calculation by parallel path swapping. *Phys. Rev. Lett.*, 98:268301, 2007.

[15] T. S. van Erp. Efficiency analysis of reaction rate calculation methods using analytical models I: The two-dimensional sharp barrier. *J. Chem. Phys.*, 125:174106–20, 2006.

[16] P. L. Geissler, C. Dellago, D. Chandler, J. Hutter, and M. Parrinello. Autoionization in liquid water. *Science*, 291:2121–2124, 2001.

[17] A. Hassanali, M. K. Prakash, H. Eshet, and M. Parrinello. On the recombination of hydronium and hydroxide ions in water. *Proc. Natl. Acad. Sci. USA*, 108:20410–20415, 2011.

[18] T. S. van Erp, M. Moqadam, E. Riccardi, and A. Lervik. Analyzing complex reaction mechanisms using path sampling. *J. Chem. Theory Comput.*, 2016. In press, DOI: 10.1021/acs.jctc.6b00642.

[19] J. Hutter, M. Iannuzzi, F. Schiffmann, and J. VandeVondele. cp2k: atomistic simulations of condensed matter systems. *WIREs Comput. Mol. Sci*, 4:15–25, 2014.

[20] J. VandeVondele and J. Hutter. Gaussian basis sets for accurate calculations on molecular systems in gas and condensed phases. *J. Chem. Phys*, 127:114105–9, 2007.

[21] M. Sprik, J. Hutter, and M. Parrinello. Ab initio molecular dynamics simulation of liquid water: Comparison of three gradient-corrected density functionals. *J. Chem. Phys.*, 105:1142–1152, 1996.

[22] A. Luzar and D. Chandler. Effect of environment on hydrogen bond dynamics in liquid water. *Phys. Rev. Lett.*, 76:928–931, 1996.

[23] T. H. Cormen, C. E. Leiserson, R. L. Rivest, and C. Stein. *Introduction to Algorithms, Third Edition*. The MIT Press, 3rd edition, 2009.

[24] J. R. Errington and P. G. Debenedetti. Relationship between structural order and the anomalies of liquid water. *Nature*, 409:318–321, 2001.

[25] J. Rogal, W. Lechner, J. Juraszek, B. Ensing, and P. G. Bolhuis. The reweighted path ensemble. *J. Chem. Phys.*, 133:174109–12, 2010.

[26] C. Dellago and P. G. Bolhuis. activation energies from transition path sampling simulations. *Mol. Simul.*, 30:795–799, 2004.

[27] T. S. van Erp and P. G. Bolhuis. Elaborating transition interface sampling methods. *J. Comput. Phys.*, 205:157–181, 2005.

[28] A. Nilsson and L. G. M. Pettersson. The structural origin of anomalous properties of liquid water. *Nature Communications*, 6:8998–11, 2015.

[29] N. Agmon. The grotthuss mechanism. *Chem. Phys. Lett.*, 244:456–462, 1995.

[30] D. Marx. Proton transfer 200 years after von Grotthuss: Insights from ab initio simulations. *ChemPhysChem*, 7:1848–1870, 2006.

# Chapter 7

# Autoionization of Water in Presence of Chloride and Sodium Ions [1]

---

[1] This chapter is based on work in progress and ongoing simulations.

## 7.1 Introduction

Understanding the behavior of aqueous solutions is of crucial importance in many areas of chemistry and biology. Water plays an important role as a universal solvent for a wide variety of chemical processes. The structure of liquid water is controlled by hydrogen bond interactions between water molecules. This normally influences the dynamics of water in many ways. Adding ions into pure liquid water leads to a disturbance in the natural hydrogen bond network. The water molecules must break the hydrogen bonds and reposition in order to accommodate the additive ions. Although this process is energetically unfavourable, the hydrogen bonds between ions and water molecules can recoup the loss of inter-water hydrogen bonds and result in a negative total free energy of solvation. The contribution of this ion-water interaction is determined by the strength and the number of the hydrogen bonds that surround the ion and these parameters depend on the charge and the size of the ion. An ion with smaller charge produces a weaker hydrogen bond, while an ion with high charge makes a strong hydrogen bond. Moreover, the sign of the charge is of importance for the determination of the solvation free energy. The solvation of an anion is favorable compared to the solvation of a cation because the layout of the first solvation shell of anion is more compatible with natural water-water interactions in liquid water [1]. The effect of the size of the ion in liquid water is a bit more tricky to understand. A large ion disturbs the natural water network more than small ion, in addition its charge is more delocalized, both these effects are unfavourable, but a larger ion can also create a larger solvation shell and therefore forms hydrogen bonds with more water molecules, which is again favourable. Therefore, the net effect deeply depends on the specific ion and the geometry and size of its solvation shell [2].

The solvation of ions has been studied, both experimentally [3–6] and computationally [2, 7–9]. Most of previous studies investigated the structural and dynamical properties of the solvation shell of water molecules. One of the most important chemical properties of water is its ability to act as either a Brønsted acid or a Brønsted base [10]. In pure water or aqueous solution, one water molecule can deprotonate to become a hydroxide ion, $OH^-$, and the hydrogen nucleus, $H^+$, protonates another water molecule to create hydronium, $H_3O^+$. This process is called the autoionization of water and is greatly involved with the acid-base chemical equilibria and is an important factor for determining the pH of water [11]. These charged species show up in pairs as the result of the dissociation of a water molecule, and they vanish through the recombination process. The mechanism of water dissociation and recombination has previously been studied [11–16], however, the influence of the presence of ions pair and their interactions has not been fully described yet. The interaction of the ions in solution has an important role for determining the pH of solution but due to the rarity of the autoionization process, the understanding of molecular mechanism of this process is still one the most challenging problems in the physical chemistry.

In this work, we applied the Replica exchange interface sampling (RETIS) method in combination with Born-Oppenheimer molecular dynamics (BOMD) on autodissociation of water molecules in presence of chloride and sodium ions. This study complements and expands our previous work on pure water by addressing how the presence of ions can accelerate the ionization process of water.

## 7.2 Methodology and Computation Details

Path sampling [17] has become a very efficient approach to calculate quantitative properties like reaction rates and to provide qualitative analysis on reaction mechanisms. In this work, we use RETIS [18] as an advanced sampling method to explore the true dynamical pathways and to measure the rate constant of transition between two stable states. The ensemble of trajectories, that is obtained from RETIS simulation, provides a wealth of information about the reaction process. From this simulation we obtain large sets of paths connecting reactant and product state or paths that make progress along the reaction coordinate but then fail to reach the product state. Using this data, we can use path analysis in order to extract the qualitative and the quantitative path features from these sets.

In this work, we studied the effect of additives on the autoionization process of water. For this purpose, we employed the RETIS simulation combined with CP2K BOMD [19]. We investigated the application of this method for studying molecular mechanism and rate constant of the autodissociation of water into the charged separated state of $H_3O^+$ and $OH^-$ ions in pure water and in the presence of sodium and chloride ions.

In this work, water was modeled using the Goedecker-Teter-Hutter (GTH) pseudopotentials [20, 21], the BLYP functional [22, 23] and a DZVP-MOLOPT basis set [24]. In addition to the Gaussian basis set, a plane-wave basis set was used with a plane-wave cutoff 400 Ry. The BLYP functional has proven to give an accurate description of the structure and dynamics of water. The simulations were performed using a cubic simulation box of $13 \times 13 \times 13$ Å$^3$ containing 64 water molecules and a $Cl^-$ or a $Na^+$ ions. The simulation were carried out using the CP2K program package with 0.5 fs timestep and NVE dynamics. Shooting moves were performed by randomly reselecting the velocities at the shooting point from a Maxwellian distribution corresponding to a temperature of 300 K.

The reaction coordinate was defined using the distances between oxygen and hydrogen atoms. The reaction coordinate initially is $\mathrm{MAX}[|OH|]$ which implies that the value of the reaction coordinate corresponds to the largest OH distance in the system that is still considered to be a bond. Once a OH bond breaks and the proton transfers to another water molecule, the reaction coordinate switches to the shortest distance from the oxygen in $OH^-$ to a hydrogen in $H_3O^+$. This approach guarantees that the reaction can and will occur at any OH bond of any molecule.

## 7.3 Preliminary Analysis and Discussion

Water molecules sometimes spontaneously ionize into hydroxide and hydronium. This spontaneous dissociation of water molecule leads to a proton transfer through the solution along a hydrogen bond wire. Once the hydronium and hydroxide are separated from each other, they may remain in ionized state for a while or may recombine quickly. The presence of additive ions and other impurities in the solution affects solvation shell of water around the hydroxide and hydronium ions and obviously influences the ionization process in the solution.

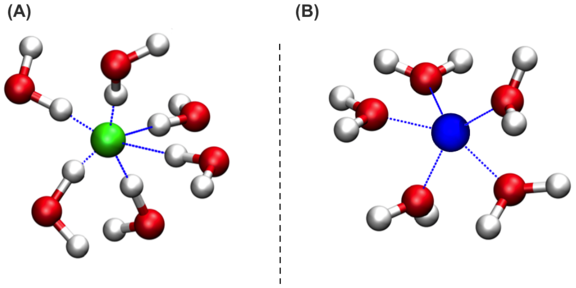

**Figure 7.1:** Representative snapshot of water molecules surrounding (A) negative and (B) positive ions.

Figure. 7.1 shows chloride and sodium ions surrounded by a layer of sticky water molecules. Water molecule has a permanent dipole, it means that one end (H) is always slightly positively charged and the other end (O) is always slightly negatively charged. Therefore, the charged ends of the water molecules are strongly attracted to the sodium and chloride ions. The alignment of the hydrogen bonded network and the presence of strong electrostatic forces are suspected to facilitate the ionization process.

We detected different types of ionization processes in the presence of the chloride ion. Figure. 7.2A shows the mechanism in which the chloride ion is not directly involved in the ionization process. Although this mechanism looks very similar to the autoionization process in pure water, influence of the presence of chloride is completely recognizable. We observed that the ionization reaction always commences inside the first solvation shell around the chloride ion. Figure. 7.3A shows the radial distribution function for chloride-oxygen pair. The hydronium is mostly formed around the distance 2.75 Å which we identified as the minimum $H_3O^+-Cl^-$ contact-ion pair distance. The hydronium ion can present either as a direct $H_3O^+-Cl^-$ contact-ion pair or transfer along the hydrogen wire and present as a solvent-separated ion pair. The hydroxide is always located in the second solvation shell around the chloride as a solvent-separated ion pair.

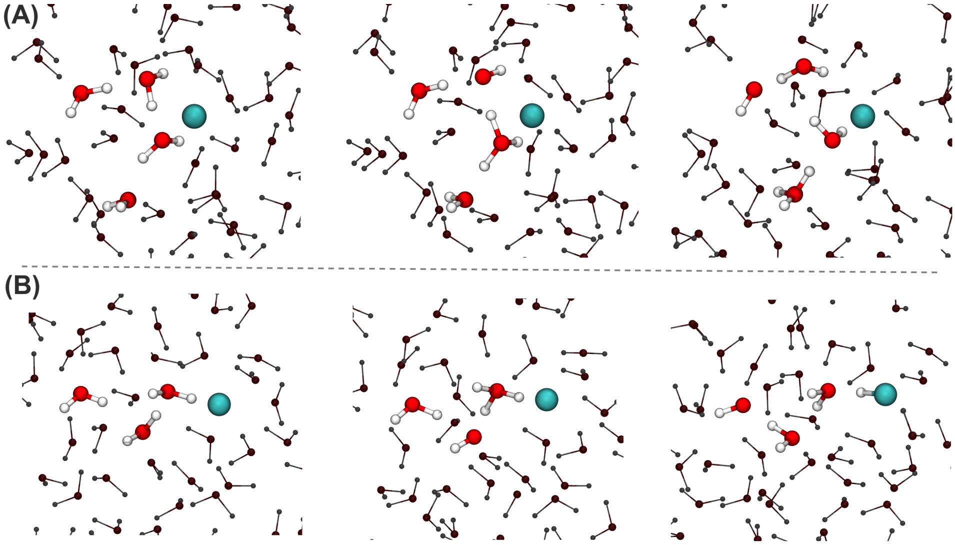

**Figure 7.2:** Representative snapshot of water ionization in presence of chloride ion. Water molecule involved in ionization wire are shown bold and the chloride ion is in cyan. (A) the autoionization process, (B) the autoionization process producing hydrochloric acid and hydroxide.

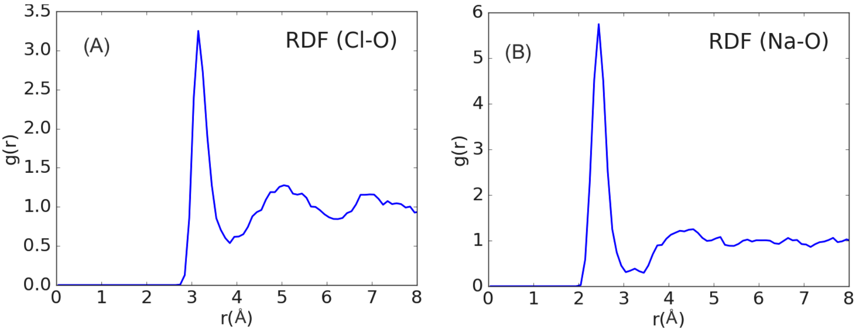

**Figure 7.3:** Radial distribution function for (A) chloride-oxygen Cl−O, (B) sodium-oxygen Na−O pair at T = 300 K.

Figure. 7.2B shows the mechanism in which the chloride ion directly participates in the ionization process. Chloride ion is very electronegative and once a water molecule approaches the chloride ion less than contact-ion pair distance, the chloride ion pulls off a hydrogen from that water, and concertedly a proton transfers from another water molecule to that water and forms the hydroxide and hydronium ions. Upon decreasing of the central $H_3O^+{-}Cl^-$ distance, the proton can barrierlessly shuttle between the oxygen and chloride. When the proton transfers to the chloride ion and the resulting water molecule builds hydrogen bonds with the hydroxide ion and other water molecules, the

$H_2O{-}HCl$ distance increases and the transfer is complete. The hydroxide ion sometimes accepts a proton from another water molecule in the wire and moves further into the second solvation shell of water around the chloride.

Figure. 7.4 shows the autoionization reaction in the presence of sodium ion. We observed that the autoionization reaction always occurs in the second solvent shell around the sodium ion. Figure. 7.3B shows the radial distribution function for sodium-oxygen pair. The positively charged sodium ion and the negatively charged hydroxide ion interaction is very small but nonnegligible. This interaction explains why the hydroxide-sodium distance is always less than the hydronium-sodium distance in our reactive trajectories. However, the $HO^{-}{-}Na^{+}$ pair always remains present as a solvent-separated ion pair.

Our analysis in this chapter was based on our ongoing simulations. Because our research efforts are in progress, we focused on a brief qualitative analysis for the autoionization process in presence of the ions rather than presenting quantitative results. Despite the preliminary character of our simulations, the results clearly suggest that the presence of ions enhance the rate of the autoionization process ($R_{nH_2O+Cl} > R_{nH_2O+Na} > R_{nH_2O}$). However, once the ionization has occurred the presence of contaminants, such as chloride and sodium ions, can cause a decline in excess proton diffusivity, i. e. the frequency of proton jumps between water molecules is reduced [9]. For example, in the case of chloride ion the relatively small diffusion constant, combined with the strong hydrogen bonding between the ion and water molecules, results in slow dynamics of the solvation shell around the hydronium ion. Therefore, this twisted and slowed down solvation shell around the hydronium ion decreases the rate of recombination severely which leads to longer reactive trajectories in our simulation.

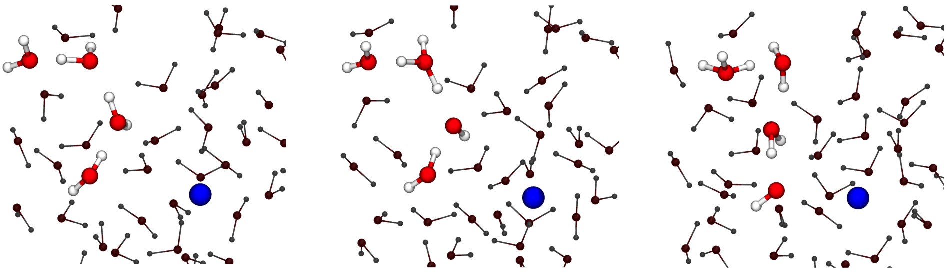

**Figure 7.4:** Representative snapshot of water autoionization in presence of sodium ion. Water molecule involved in autoionization wire are shown bold and the sodium ion is in blue colour.

# Bibliography

[1] A. Grossfield. Dependence of ion hydration on the sign of the ion's charge. *J. Chem. Phys.*, 122:024506–024506, 2005.

[2] J. M. Heuft and E. J. Meijer. Density functional theory based molecular-dynamics study of aqueous chloride solvation. *J. Chem. Phys.*, 119:11788–11791, 2003.

[3] G. W. Neilson and J. E. Enderby. The coordination of metal aqua ions. *Adv. Inorg. Chem.*, 34:195–218, 1989.

[4] D. H. Powell, G. W. Neilson, and J. E. Enderby. The structure of $Cl^-$ in aqueous solution: an experimental determination of $g_{ClH}$(r) and $g_{ClO}$(r). *J. Phys. Condens. Matter*, 5:5723–5730, 1993.

[5] M. F. Kropman and H. J. Bakker. Dynamics of water molecules in aqueous solvation shells. *Science*, 291:2118–2120, 2001.

[6] W. E. Price, R. Mills, and L. A. Woolf. Use of experimental diffusion coefficients to probe solute-solute and solute-solvent interactions in electrolyte solutions. *J. Phys. Chem.*, 100:1406–1410, 1996.

[7] J. M. Heuft and E. J. Meijer. Density functional theory based molecular-dynamics study of aqueous fluoride solvation. *J. Phys. Chem.*, 122:094501–7, 2005.

[8] J. M. Heuft and E. J. Meijer. Density functional theory based molecular-dynamics study of aqueous iodide solvation. *J. Phys. Chem.*, 123:094506–5, 2005.

[9] J. M. Heuft and E. J. Meijer. A density functional theory based study of the microscopic structure and dynamics of aqueous HCl solutions. *Phys. Chem. Chem. Phys.*, 8:3116–3123, 2006.

[10] R. L. Myers. *The Basics of Chemistry*. Greenwood Publishing Group, Westport, London, 2003.

[11] P. L. Geissler, C. Dellago, D. Chandler, J. Hutter, and M. Parrinello. Autoionization in liquid water. *Science*, 291:2121–2124, 2001.

[12] O. Coskuner, E. A. A. Jarvis, and T. C. Allison. Water dissociation in the presence of metal ions. *Angew. Chem., Int.Ed.*, 46:7853–7855, 2007.

[13] O. Coskuner and T. C. Allison. Dynamic and structural properties of aqueous arsenic solutions. *ChemPhysChem*, 10:1187–1189, 2009.

[14] A. Hassanali, M. K. Prakash, H. Eshet, and M. Parrinello. On the recombination of hydronium and hydroxide ions in water. *PNAS*, 108:20410–20415, 2011.

[15] A. Hassanali, F. Giberti, J. Cuny, T. D. Kühne, and M. Parrinello. Proton transfer through the water gossamer. *PNAS*, 110:13723–13728, 2013.

[16] N. Agmon, H. J. Bakker, R. K. Campen, R. H. Henchman, P. Pohl, S. Roke, M. Thämer, and A. Hassanali. Protons and hydroxide ions in aqueous systems. *Chem Rev.*, 116:7642–7672, 2016.

[17] C. Dellago, P. G. Bolhuis, F. S. Csajka, and D. Chandler. Transition path sampling and the calculation of rate constants. *J. Chem. Phys.*, 108:1964–1977, 1998.

[18] T. S. van Erp. Reaction rate calculation by parallel path swapping. *Phys. Rev. Lett.*, 98:268301–4, 2007.

[19] CP2K: High Performance Computing, http://www.nanosim.mat.ethz.ch/ research/cp2k.

[20] S. Goedecker, M. Teter, and J. Hutter. Separable dual-space Gaussian pseudopotentials. *Phys. Rev. B*, 54:1703–1710, 1996.

[21] C. Hartwigsen, S. Goedecker, and J. Hutter. Relativistic separable dual-space Gaussian pseudopotentials from H to Rn. *Phys. Rev. B*, 58:3641–3662, 1998.

[22] A. D. Becke. Density-functional exchange-energy approximation with correct asymptotic behavior. *Phys. Rev. A*, 38:3098–3100, 1988.

[23] C. Lee, W. Yang, and R. G. Parr. Development of the Colle-Salvetti correlation-energy formula into a functional of the electron density. *Phys. Rev. B*, 37:785–789, 1988.

[24] J. VandeVondele and J. Hutter. Gaussian basis sets for accurate calculations on molecular systems in gas and condensed phases. *J. Chem. Phys.*, 127:114105–114105, 2007.

# Chapter 8

# Summary, Conclusions, and Prospectives

The aim of this thesis is to theoretically study and advance the application of the RETIS path sampling method for realistic modeling of chemical systems. These applications are the study on autoionization of water, which is a fundamental application, and silicate oligomerization in gas phase and aqueous solution, a reaction that is relevant for e.g. zeolite synthesis. Applications that have been undertaken served as proof for the ability of this method to deal with realistic and complex environments.

In chapter 3, the main focus has been put on presenting a comparison between DFT and ReaxFF calculations (using two already published parameter sets) for the initial step of the silicate dimerization reaction. Notable discrepancies between the two methods have been found, with ReaxFF showing a few unphysical results. Our results suggest that the standard procedures for parameter fitting need to be improved by a mutual comparative method. Furthermore, the reactions were deeply investigated using DFT and constrained molecular dynamics. This provided reaction barriers but did not allow the study of the unbiased reaction dynamics.

In order to study the actual reaction dynamics, RETIS has been employed in chapter 4 to gather a collection of true dynamical unbiased trajectories connecting stable states. From these trajectories exact rate constants are computed and true reaction mechanisms are identified. Quantitative and qualitative analysis on different reaction mechanisms for the dissociation process and the water removal step are presented.

An approach to analyze collective variables for chemical reactions is introduced in chapter 5. The analysis method introduces a new theoretical concept which corresponds to a measure of predictive power for a reaction. This predictive power can be optimized by a search in collective variable space. The method is based on already available path sampling data from a TIS, RETIS or FFS simulation. The method was tested on one-dimensional double well potential, a theoretical model for an ion-transfer reaction, and an Ab initio molecular dynamics study of water autoionization at low density. The approach allows testing hypotheses on the reaction mechanisms and can be used to construct the phase space committor surfaces without the need of additional trajectory sampling. Quantitative interpretation of path sampling data is enhanced with this analysis technique providing practical hints on how reactions can be steered in desired directions.

In chapter 6, RETIS simulations of water autodissociation in pure water are performed. The reaction coordinate is defined using distances between oxygen and hydrogen atoms. The rate of proton transfer between water molecules is computed without specifying which water molecule or which OH bond should break. This rate well agrees with the experiments at 25°C. Also, the obtained activation energy is close to the experimental value. The reactive trajectories generated by the RETIS algorithm provide insight to discuss possible ways to enhance water splitting.

We can conclude that RETIS simulations are an effective method to compute rate constants and to unravel reaction mechanisms. RETIS has the advantage over other methods to provide the real dynamics. In the dimerization reaction this aspect provided new insights which were not achievable using biasing techniques. After this study, it would be interesting to apply RETIS to other silicate reactions like the formation of longer linear and three-ring silicate oligomers.

In our simulations, molecular dynamics treats the atomic nuclei as classical particles whose trajectories are computed by integrating Newton's equations of motion. However, because of light mass, hydrogen nuclei are subjected to nuclear quantum effects. These effects might have an impact on H-bond fluctuations in water, and presumably also in other hydrogen-bonded systems. There are approaches like finite path integrals molecular dynamics that can treat the nuclei as the quantum mechanical objects but they are very expensive and are not suited for studying of dynamics. These effects can also be seen in the autoionization of water-heavy water mixture. Since the nuclear quantum effects are more important for hydrogen than deuterium, comparing water ($H_2O$) and heavy water ($D_2O$) systems both theoretically and experimentally might shine a light on the effect of the quantum nature of hydrogen. Therefore, an interesting and informative extension of the autoionization process can be the autoionization in water-heavy water mixtures in which several species may be observed: $H_2O$, HDO, $D_2O$, $H_3O^+$, $D_3O^+$, $H_2DO^+$, $HD_2O^+$, $HO^-$ and $DO^-$. The heavy water, under standard conditions, is less dissociated than ordinary water. This is a reflection of the somewhat shorter and stronger bond between D and O, which means it will take a greater amount of energy to separate D from O. Moreover, based on classical transition state theory, the rate is proportional to the inverse of the square root of mass. Deuterium is 2 times heavier than hydrogen, therefore, we can expect that the rate of $D-O$ dissociation would be about 1.4 times smaller than that of $H-O$.

In Ab initio molecular dynamics simulations, the gradient-corrected BLYP functionals have been the most popular for the study of aqueous solutions. However, it has been noted that BLYP produces slightly over-structured water with a somewhat larger number of H-bonds than experimental evidences suggest. This leads to longer H-bond lifetimes and sluggish water dynamics, particularly a slower self-diffusion coefficient for water molecules. The major causes of this inaccuracy are a poor description of weak dispersion interactions, the self-interaction error and omission of nuclear quantum effects. Some of the dispersion correction schemes proposed for water give less over-structured water, with RDFs and angle distribution functions in better agreement with experiments. However, sensitivity of results with respect to choice of basis set, density functional might still be a concern in Ab initio simulations. Our collective analysis shows that the over-structure in water can lead to two mechanisms, one increases and one decreases the autoionization reaction and it is not clear which one is more important. More structure means more H-bonds and more electrostatic effects. Therefore, molecules get more polarized and this will increase the rate of autodissociation. On the other hand, a defect from tetrahedral structure can help the autodissociation to occur as we showed in Chapter 6.

Another issue in Ab initio molecular dynamics simulation is the effect of the periodic boundary conditions due to its necessarily small box size. These edge effects can result in an increase in the rate of autodissociation of water because molecules may interact with the periodic images in a neighbouring box. We are, therefore, planning to repeat these type of simulations using a larger simulation box with twice the number of water molecules.

Despite these limitations, our approach provides realistic qualitative analysis, as well as semi-quantitative analysis on unbiased reaction dynamics. Therefore, we believe that the technique presented in this thesis may open up many possible avenues for investigating chemical reactions. Besides the fundamental new insight, these type of simulations will eventually help to obtain a better control of chemical reactions and provide new inspiration for alternative synthesis methods.